UNIVERSITY OF OKLAHOMA

GRADUATE COLLEGE

MOLECULAR BEAM EPITAXY OF NARROW GAP QUANTUM WELLS: INSB, INGAAS AND ELEMENTAL SB

A DISSERTATION

SUBMITTED TO THE GRADUATE FACULTY

in partial fulfillment of the requirements for the

Degree of

DOCTOR OF PHILOSOPHY

By

CHOMANI K. GASPE MUDIYANSELAGE
Norman, Oklahoma
2013

MOLECULAR BEAM EPITAXY OF NARROW GAP QUANTUM WELLS:
INSB, INGAAS AND ELEMENTAL SB

A DISSERTATION APPROVED FOR THE
HOMER L. DODGE DEPARTMENT OF PHYSICS AND ASTRONOMY

BY

_____
Dr. Michael B. Santos, Chair

_____
Dr. Sheena Q. Murphy

_____
Dr. Kieran Mullen

_____
Dr. Patrick Skubic

_____
Dr. Patrick J. McCann

To my parents, two sisters, brother and relatives

Acknowledgements

First, I would like to express my heartfelt deepest gratitude to my thesis advisor Prof. Michael Santos for his enormous support, advise, encouragement and guidance throughout my Ph.D. He is one of the kindest and most helpful persons I ever met and I am extremely grateful to him for his patience, understanding and being there for me at all times.

I would also like to thank my dissertation committee: Prof. Sheena Murphy, Prof. Kieran Mullen, Prof. Patrick Skubic, and Prof. Patrick McCann for their input and advise during my graduate studies. Very special thanks to Prof. Sheena Murphy for suggestions, discussions and ideas with regard to the Sb research project. I would also take this opportunity to thank Prof. Matthew Johnson for his technical support and advise in many occasions during my lab work at OU.

I thank Dr. Tetsuya Mishima for his invaluable support, advise, discussions on growth and technical issues and also for providing me TEM images. I thank Dr. Joel Keay for his enormous support on technical issues, input in my research, for SEM images in addition to his invaluable time in training me in most of the lab equipment's at OU. I have learnt a lot from their vast knowledge.

I thank Dr. Mukul Debnath, Dr. Lu Li, fellow graduate students, Sangeetha, Kaushini, Holly, Lin and Shayne for their assistance in lab work, various measurements and on top of all to their friendship. I would like to thank former members of MBE group,

Madhavie and Dr. Hong Wen for their initial help in my lab work and training me in MBE, Dr. Niti Goel at Intel for the direction and guidance for the Intel project.

I am very much fortunate to have a great group of friends in and out of OU. I cannot thank them enough for their friendship, support and for being there for me at all times.

Thanks for the staff at NHMFL Lab in Tallahassee FL for the support during magneto-optical measurements. I greatly acknowledge the funding from NSF and Intel Grants and Scholarships for my research and graduate studies at OU.

I would like to thank faculty and the staff of the Physics Department at OU for their excellent support during my graduate studies. I also greatly acknowledge faculty of the Physics department at University of Peradeniya (Sri Lanka) for the guidance throughout my undergraduate studies and arousing my interest for graduate studies in Physics.

Very special thanks to Dr. Furneaux and Sandy for having me and my family at her place for thanksgiving and Jack 'O' Lantern celebrations and introducing me the traditional and cultural festivals.

Last but not least I would like to express my deepest thanks to my wonderful parents, two sisters, brother and my relatives for their endless love and giving me courage and moral support to achieve my educational goals. I am very much grateful to my husband Sumudu and my daughter Navindri for their love and patience which gave me the strength to hang on to my work.

Table of Contents

List of Tables

List of Figures

Abstract

In this work the electronic properties of *n*-type and *p*-type quantum wells (QWs) made of narrow gap InSb and InGaAs materials have been studied experimentally. The narrower band gap in these materials leads to smaller effective masses for electrons and holes, therefore higher mobilities are expected. High intrinsic electron mobility due to the small effective mass for electrons in these materials makes them attractive as the channel material in *n*-type transistors. The layer structure, doping and growth parameters were further optimized to enhance the mobility for electrons in InSb and InGaAs QWs. A room-temperature electron mobility of 11,600cm^2/Vs and 44,700cm^2/Vs were achieved in our QWs made of $In_{0.64}Ga_{0.36}As$ and InSb, respectively.

The hole effective mass in InSb QWs with different strain and confinement was studied. To achieve high hole mobilities, strain and confinement must be maximized. Both parameters increase the energy splitting between heavy and light hole bands and lower the effective mass for in-plane motion. The smallest hole effective mass of $0.017m_e$ was observed in an InSb QW with 1.05% strain and 7nm well width. Hole mobility in strained InSb QWs grown on GaAs(001) substrates can be significantly improved by better buffer layer design. The effect of the thickness and the Al composition in the $Al_xln_{1-x}Sb$ initial buffer layer on hole mobility of *p*-type InSb QWs was also studied. A room-temperature hole mobility of 1,050cm^2/Vs has been achieved in our improved *p*-type InSb QW with 1.32% strain, 7nm well width and a 0.8μm thick $Al_{0.15}In_{0.85}Sb$ initial buffer layer. The compressive strain was introduced into $In_yGa_{1-y}As$ QWs by increasing the Indium composition (y) in the well slightly above the value needed for

lattice matching (y=0.53) with InP (001) substrates. A room temperature hole mobility of 230cm^2/Vs was obtained in our $In_{0.75}Ga_{0.25}As$ QW with remotely, Be δ-doped $In_{0.45}Al_{0.55}As$ barrier layers.

An experimental study of growth, structural and electronic properties of elemental Sb QWs with GaSb barriers was performed to explore their potential as topological insulators. Molecular beam epitaxy growth procedures on GaAs(111)A and GaSb(111)A were developed to realize ultra-thin layers of Sb with a thickness ≤ 4nm. Transmission electron microscopy and scanning electron microscopy indicated good crystalline quality in these ultra-thin layers of Sb. Resistivity measurements indicated that Sb QWs with a thickness above ~2nm were metallic, whereas thinner wells showed insulating behavior.

Dissertation Outline

In order to obtain high-performance, complementary metal oxide semiconductor (CMOS) circuits require both *n*-type and *p*-type transistors with high mobility carriers. Because of the comparable electron and hole mobilities for Si and the well-established fabrication techniques, Si based transistors have been the workhorse for the CMOS circuits until now. Narrow gap III-V channel based *n*-type field effect transistors (FETs), however, have demonstrated better performance due to their high intrinsic electron mobility and saturation velocity compared to Si. Therefore they have the potential to enable future high speed electronic devices that operate under lower power. Their narrower band gap is beneficial because it leads to smaller effective masses for electrons and holes which will lead to higher mobility. Quantum wells (QWs) made out of III-V narrow gap materials such as InSb and InGaAs with high electron mobility, unfortunately, exhibit low hole mobility. Additionally, the lack of a good native oxide as a gate dielectric is also an issue facing narrow gap channel FETs for use in future logic applications. This dissertation is concerned with electron and hole mobility in InSb and InGaAs QWs as well as the integration of high-κ dielectrics with these materials.

Sb based materials exhibit inherently large spin orbit coupling which makes InSb also suitable for spintronic device applications, and elemental Sb has potential for a new class of materials called topological insulators (TIs). In TIs the bulk is insulating due to an energy gap while the surface is conducting due to un-gapped protected surface states. Quantum confinement is predicted to open up a gap for the bulk states in semimetallic

Sb, revealing the new TI properties of the surface states. Still thinner films should ultimately display trivial insulator properties. This dissertation also discusses the realization of ultra-thin films of Sb and a semimetal-to-insulator transition in these films.

The dissertation chapters are organized in the following way:

Chapter 1: All narrow-gap InSb, InGaAs and Sb QWs reported in this dissertation are grown by molecular beam epitaxy. This chapter reviews the experimental procedures used in molecular beam epitaxy growth.

Chapter 2: Material characterization by use of high resolution x-ray diffraction (HRXRD) and Hall effect measurements are important in optimizing the growth, structural and electronic properties of the MBE grown heterostructures. This chapter reviews the fundamentals and experimental methods for determining the structural and electronic parameters of these materials using HRXRD and Hall effect measurements.

Chapter 3: A study of the dependence of the electrical properties of two-dimensional electron systems in InSb and InGaAs QWs on structural and growth parameters is described in this chapter. Further optimization of these parameters led to further increases in electron mobility in these materials. A collaborative study of high-κ gate dielectrics on $In_yGa_{1-y}As$ channel material is also briefly discussed in this chapter.

Chapter 4: Strain and confinement effects alter the valence band structure in a way that lowers the effective mass of the holes thereby increasing the hole mobility. Our research efforts to improve the hole mobility in two-dimensional hole systems in InSb and

InGaAs QWs by use of biaxial strain, confinement and optimization of the buffer layer structure are discussed in this chapter.

Chapter 5: A successful growth procedure to realize ultra-thin Sb QWs with the thickness ranging from ~1 to 4nm with GaSb barrier layers is described in this chapter. Dominant quantum confinement effects resulted in a metal-to-insulator transition in our ultra-thin Sb wells with a thickness below ~2nm.

Chapter 6: This chapter summarizes the results obtained in this dissertation work and makes suggestions for future work.

Chapter 1

Molecular Beam Epitaxy

1.0 Introduction

Molecular beam epitaxy (MBE) is an experimental technique for growing thin films of a wide variety of materials, ranging from oxides to semiconductors to metals. In this technique, a beam of atoms or molecules travels through an ultra-high vacuum (UHV~1×10^{-8} Torr) to a heated crystalline substrate to form a crystalline layer in registry with the substrate. MBE has the ability to precisely control the thickness (to an atomic level), composition, and doping of these layers by changing the beam fluxes and substrate temperature. The UHV environment preserves the purity of the growing film and the surface of the growing film can be monitored using a technique called Reflection High Energy Electron Diffraction, RHEED. Because of this control, MBE grown structures such as superlattices, quantum wells and quantum dots can be developed not only for fundamental research but also for creating novel electronic and optical devices.

This chapter describes the main components of an MBE system and the experimental procedures used in MBE growth.

1.1 MBE system in the Department of Physics and Astronomy at OU

An Intevac Modular Gen II MBE system with two-growth chambers and a shared central analysis chamber are installed at the Department of Physics and Astronomy, University of Oklahoma. The analysis chamber is equipped with XPS (X-ray photoelectron spectroscopy) and AES (Auger electron spectroscopy) instruments and isolates the III-V and IV-VI MBE systems from each other. The schematic of typical MBE growth chamber and a picture of the III-V side of the MBE system at OU are shown in Figure 1.1.

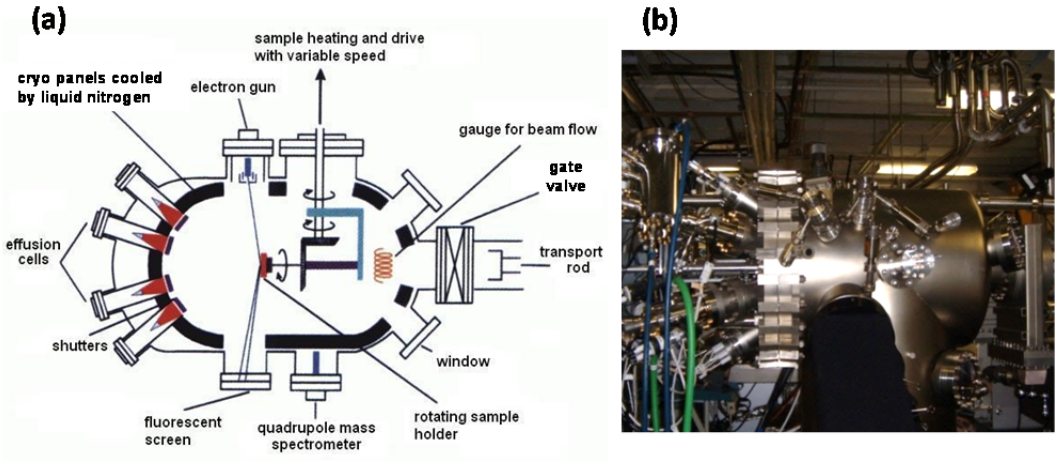

Figure 1.1: (a) Schematic of MBE system [1] and (b) a picture of III-V MBE system in the physics department at OU.

1.2 Experimental methods

The III-V part of the MBE system primarily consists of three vacuum chambers: a growth chamber, a buffer chamber and a load lock or entry-exit chamber, each with a

suitable pumping system. All three chambers are isolated from each other by gate valves.

1.2.1 Entry-Exit Chamber

In the entry-exit chamber, new substrates, individually mounted in a uni-block (Indium-free mounting), are installed on a trolley which can transport them from chamber to chamber. After being opened to atmosphere, the chamber can be pumped down to <10mTorr by a rough pumping system with a scroll pump and a molecular drag pump. This reduces the gas load introduced into the main vacuum when opening the valve to the rest of the system. The UHV ($<10^{-8}$ Torr) in the entry-exit chamber is then achieved by using a small cryopump. When the pressure is low enough ($<5\times10^{-7}$ Torr) the chamber is heated at 200°C in order to outgas the substrates and their holders for a minimum of 2 hours. The trolley is transferred to the buffer chamber when the entry-exit chamber is cooled back down to the room temperature.

1.2.2 Buffer Chamber

The buffer chamber is used as a transition tube between the entry-exit chamber and the growth chamber and the shared analysis chamber. The new substrates are transferred to another trolley stored in the buffer chamber, so that the grown wafer can be unloaded without exposing the un-grown substrates to the air. The substrates are further degassed at a heated station in the buffer chamber (GaAs at 300°C for 12 hours

and InP at 200°C for 2-3 hours) before transfer into the growth chamber. The magnetically coupled transfer rods are used to move uni-blocks between the trolley, the substrate holder in the growth chamber and the heated station in the buffer chamber. This can be done since the uni-blocks are made out of nonmagnetic materials and since the bearings provide a smooth transport of the trolley in the vacuum. The proper alignment of pin positions in the transfer rods with those of the uni-blocks on the trolley is also necessary for a smooth and secure transfer of the substrate. The UHV in the buffer chamber is achieved by using an ion pump and a Ti sublimation pump (which is used primarily after venting the chamber). The idle pressure in the buffer chamber is $\sim 5\times10^{-10}$ Torr and it increases up to 1×10^{-7} Torr at the beginning (and to $\sim 2\text{-}5\times10^{-9}$ Torr at the end) of the substrate degasing procedure.

1.2.3 Growth Chamber

The critical part of the process occurs in the growth chamber. It contains the following essential components for MBE growth as shown in Fig.1 (a).

a. Cryopanels
b. Beam sources
c. Substrate manipulator and heater
d. Beam flux gauge and mass spectrometer
e. RHEED

The most important requirement in MBE is that the vacuum surrounding the growing epilayer must be kept as low as possible to avoid contamination from the

background gases. To maintain the UHV, the components of the MBE system are made out of materials that outgas negligibly at higher temperatures such as molybdenum and tantalum [2]. Liquid nitrogen cooled cryopanels are used in the growth chamber in addition to a cryopump (pumping speed of air, ~1500 l/s) and the ion pump (pumping speed of air, 400 l/s) to keep the partial pressure of unwanted gases such as H_2O and CO_2 below 10^{-11} Torr. The flux of residual gases is much less than that of the beam sources at UHV conditions. Therefore a slow growth rate of < 1ML/s can still keep the impurity level of the growing layer at one part per million or less [2]. The whole chamber must be baked at 200°C for about a week to re-obtain the UHV conditions, after venting to refill the source materials or for maintenance. A mass spectrometer is used for residual gas analysis (RGA) and for leak detection. Typically, the III-V growth chamber is operated for more than 10 months without exposure to atmosphere with careful use and proper maintenance of the system. In this case the predominant background gases in the system are the high vapor pressure group V (As and Sb) elements.

The III-V MBE system has 8 source ports, 7 are being used for the effusion cells and the remaining port is used for a viewing window. The group III elements (Gallium, Indium and Aluminum) and the dopant elements (Silicon for *n*-type and Beryllium for *p*-type) are loaded in 50 cc and 5cc conical shaped crucibles, respectively, (with an insert for Al) which are made out of pyrolytic boron nitride (PBN). All the cells are surrounded by a chilled alcohol (-37°C) shroud which keeps them thermally isolated from each other. Antimony (Sb) is stored in the bulk (evaporator) part of the dual zone effusion cell with a thermal cracker which breaks the Sb_4 into Sb_2. Arsenic (As) is

stored in a valved cracker effusion cell with a large crucible. The automated valve positioner operates the valve inside the cell to control the As flux (As_2). Since the As and Sb cells extend outside the cooling panel, cooling water runs around the cells for dissipating heat. The In, Ga, and Al charges are melted slowly by controlling the power to the cells. In particular, melting or solidifying Al needs to be done carefully. If the temperature fluctuates around the melting point (~660°C) due to rapid melting or cooling, the crucible can be cracked by contraction since Al adheres to the crucible walls.

A battery backup is used to maintain the temperature of the Al and Ga cells in the event of a power failure. Sudden freezing of the Ga charge during a power failure (while alcohol and liquid nitrogen cooling are running) can also crack the crucible since Ga solidifies at room temperature. After heating each source independently until a molecular beam flux is generated, the intensity of the beam is controlled by changing the cell temperature with proportional, integral and derivative (PID) controllers. In UHV, the atoms or molecules in these beams have a long mean free path so that they travel straight to the substrate without collisions. Mechanically controlled shutters in front of the cells switch the beams on and off. The molecular beams of the source materials come onto the substrate from different directions and thus the beam flux is not uniform over the large substrate; therefore the substrate is continuously rotated (~25 rpm) during growth to avoid having concentration or thickness gradients in the grown layer. This substrate rotation manipulator is called Continual Azimuthal Rotation (CAR).

Good control of the MBE growth requires precise control over the substrate temperature and the III/V beam flux ratio. The substrate temperature is therefore measured by a thermocouple attached to the back side of the holder and by a pyrometer which analyzes the radiation coming off of the hot substrate. The RHEED system with a phosphor-coated window mounted in another port serves as an *in situ* growth monitoring tool. The details of the RHEED system are described in section 1.2.4. The ion gauge mounted on the opposite side of the substrate holder can be used to measure and monitor the beam flux or the beam equivalent pressure (BEP). A constant III/V flux ratio is maintained during the growth. BEP measurements can be used as a growth rate parameter after the calibration is determined by RHEED oscillations. The growth rate calibration changes rapidly when the source materials become increasingly depleted; therefore a good record of BEP saves significant time and materials by avoiding frequent calibrations.

1.2.4 Reflection High Energy Electron Diffraction

Reflection high energy electron diffraction (RHEED) is one of the most important real time surface analytical tools in an MBE system [2]. The RHEED system consists of an electron gun and a phosphorus screen. High energy electrons (9.5keV) are directed at the substrate at a low angle of 1-3° which minimizes the penetration of the electrons deep into the substrate. The resulting diffraction pattern on the phosphor screen is recorded and analyzed with a charge-coupled device (CCD) camera and KSA 4000 software.

The atoms in the two–dimensional (2D) surface lattice produce a lattice of infinite rods in the reciprocal space. The diffraction pattern is produced when these lattice rods in reciprocal space intersect with the Ewald sphere of the incident electron beam.

1.2.4.1 Surface Reconstruction

The surface of a semiconductor can be reconstructed or relaxed to minimize the surface energy. When a surface is created by cleavage or by growth, at least one bond per atom is unsatisfied, leaving unstable dangling bonds with unpaired electrons [3]. The atoms with these dangling bonds can seek new positions and change the periodicity or the translational symmetry. Surface relaxation describes the case when the surface atoms are displaced from their bulk positions. This reconstruction appears in the RHEED pattern as "fractional order features" positioned between the "integral" (bulk) order diffraction streaks.

The RHEED pattern is also used to determine whether the native oxide layer on the surface of the substrate is desorbed before growth. Since the oxide is amorphous, a diffuse diffraction pattern is observed before it is removed from the surface. The oxide desorption temperature for GaAs(001) is 600°C - 640°C and shows a 2× pattern along the [11 0] azimuth and facets along the [$\bar{1}$10] azimuth with an Sb background pressure. RHEED can also be used to determine the substrate temperature or the flux ratio (stoichiometry) by observing the transition from one surface reconstruction to another (phase transition). InSb (at ~340°C) or $Al_{0.1}In_{0.9}Sb$ (at ~300°C) undergoes a phase

transition from pseudo (1×3) to c(4×4) as the substrate temperature is decreased with the V/III flux ratio of 1.1-1.2. It is believed that the pseudo (1×3) pattern results from a mixture of different (2×4) phases of the surface [4]. Fig. 2 shows a pseudo (1×3) surface reconstruction of InSb and a c(4×4) reconstruction of a $Al_{0.1}In_{0.9}Sb$ layer under a static condition (with an Sb overpressure).

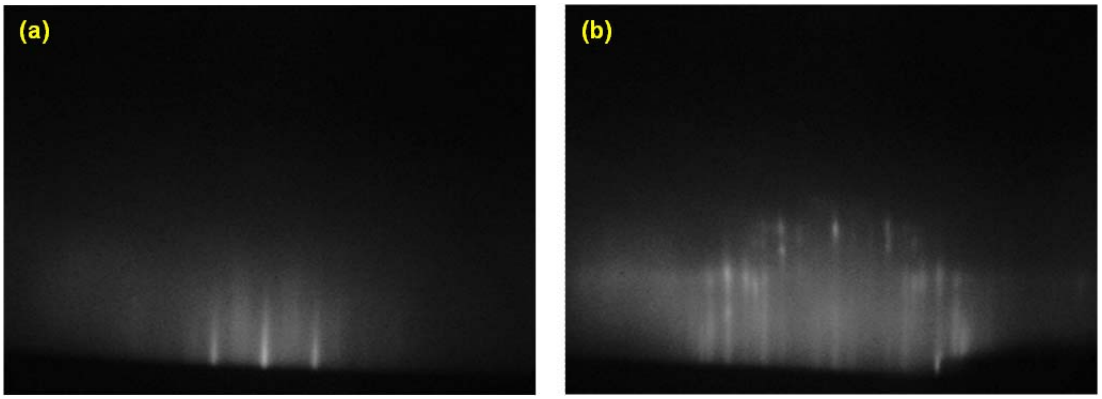

Figure 1.2: RHEED image of (a) pseudo 3× periodicity in a (1×3) surface reconstruction during InSb growth and (b) 4× periodicity in a c(4×4) surface reconstruction of $Al_{0.1}In_{0.9}Sb$ under a static condition in the $[1\ \bar{1}0]$ azimuth.

1.2.4.2 Growth rate calibration using RHEED intensity oscillations

The specular beam intensity oscillations of RHEED are used to calculate the growth rates of the materials. From the intensity of the diffraction features one can tell whether the surface is rough or smooth at the monolayer scale. The maximum intensity is obtained when the arriving atoms complete a monolayer. As more atoms are

deposited, 2D islands are formed and the surface becomes relatively rough; at this point the minimum intensity is obtained. As the growth proceeds, these islands coalesce with adjacent islands to form a complete layer. The diffraction spot oscillates in brightness due to the periodic roughening and smoothing of the surface as the growth proceeds. The time for one period of oscillation is equals to the time for one monolayer growth. Figure 1.3 shows a surface coverage of 2D islands and the corresponding RHEED intensity oscillations.

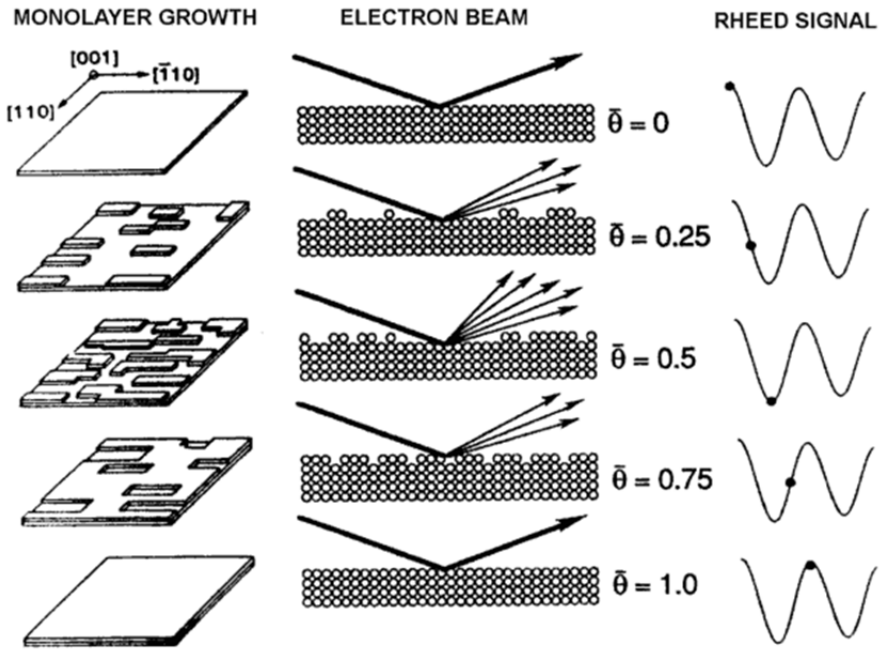

Figure 1.3: Schematic diagram of surface coverage of 2D islands and corresponding RHEED intensity oscillations [5].

In and Sb growth rates are calibrated during the growth of an InSb epilayer (~1μm thick) on a GaAs (001) substrate. The In and Sb growth rate calibration is difficult since this can be done only in a narrow range of flux ratios and growth temperatures. The group V/III flux ratio during the growth of the epilayer and during the calibration needs to be maintained at 1.0-1.1 to obtain good oscillations. After growing the epilayer at a substrate temperature of 380°C, the temperature is decreased to 25°C below the transition from pseudo (1×3) to c(4×4). The In shutter is opened for 8-10 sec while the Sb shutter is open, and a few monolayers of InSb are grown to calculate the In growth rate. For Sb calibration, the In shutter is first opened for 8-10 sec while the Sb shutter is closed. Then the In shutter is closed and the Sb shutter is opened to grow InSb and calculated the Sb growth rate. The RHEED intensity oscillations obtained for In and Sb are shown in Fig. 1.4.

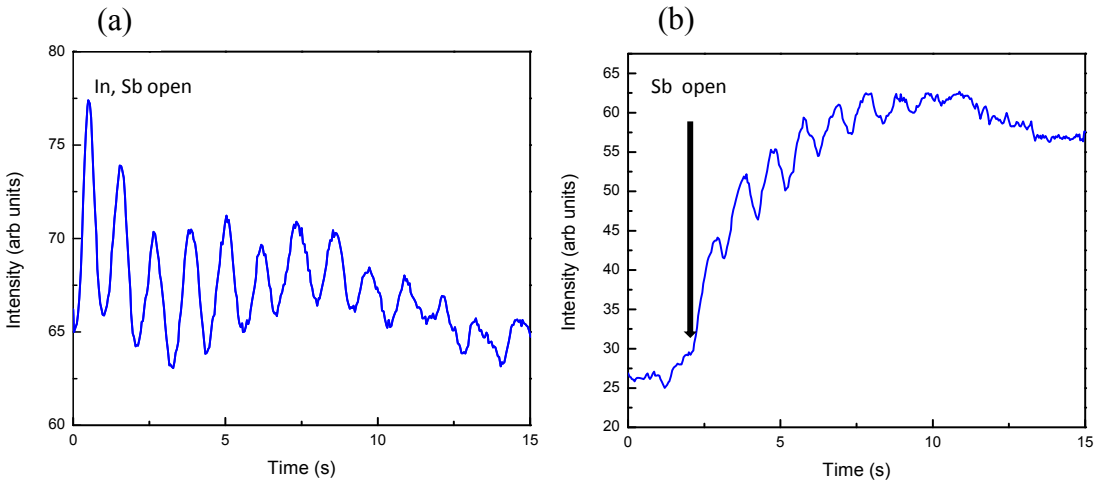

Figure 1.4: Intensity oscillations of the specular beam for (a) In limited growth on InSb and for (b) Sb limited growth of InSb.

Ga and Al are calibrated on a GaAs epilayer grown on a GaAs (001) substrate. The GaAs epilayer (~0.5μm) is grown at the oxide desorption temperature (or 20°C higher than that) with an As:Ga ratio of 15:1. The Al growth rate can be determined using the same As flux since it is not critical for this calibration. The Ga (Al) shutter is opened for 8-10sec while As is open to calculate the Ga (Al) growth rate. After doing the Al calibration, a few monolayers of GaAs are grown to cover the AlAs layer to preserve the smoothness and the purity of the surface for further calibration. RHEED intensity oscillations for As can be only seen for the lower growth rates if the valve is kept only slightly opened to reduce the flux. The As growth rate is rarely calibrated using intensity oscillations since As related growths are done using much higher As fluxes than used for As calibration. Instead, BEP measurements are used in As related growths and a V/III ratio of 15-20 is maintained during the growth.

Chapter 2

Structural and Electrical Characterization of MBE Grown Heterostructures

2.0 Introduction

Characterization techniques play an important role in the development of MBE grown structures. High resolution X-ray diffraction (HRXRD) and Hall effect measurements were widely used to characterize the structural and electrical properties of the MBE grown structures described in this dissertation. Therefore, basic definitions and experimental procedures for HRXRD (section 2.1) and Hall effect measurements (section 2.2) are described in this chapter. Structural properties such as strain, defects and potential barrier height depend on the alloy compositions of the QW and the barrier/buffer layers. In order to determine the structural properties and to optimize the growth conditions, alloy compositions were experimentally determined by HRXRD measurements. Density and mobility for electrons and holes in InSb and InGaAs QWs and resistivity in Sb QWs are the major concerns of this thesis work. Experimental determinations of these properties were carried out by means of the Hall effect using Van der Pauw methods.

2.1 High Resolution X-ray Diffraction

High resolution x-ray diffraction is a well-established technique for the structural characterization of single crystal semiconductor thin films and

heterostructures. This technique can be rapidly performed without destroying the sample. The lattice parameters, alloy composition, layer thickness, strain and the interface roughness of epilayers can be determined accurately using the X-ray diffraction (XRD) patterns.

HRXRD measurements were carried out using a Philips Materials Research Diffractometer with an incident beam from a four-reflection Ge (220) monochromater and an initial power of 1200W. The incident x-ray source is $CuK\alpha_1$ and producea a monochromatic x-ray beam with a wavelength (λ) of 1.5406Å. The goniometer, sample alignment, XRD scans and simulations were performed using Philips X'Pert software.

2.1.1 Experimental setup and basic scattering geometries

Figure 2.1 shows the experimental arrangement in real space for an XRD measurement. The angle ω is the incident angle of the x-ray beam with respect to the sample surface. The angle 2θ is the angular position of the detector (to detect the diffracted beam) with respect to the incident beam. It is 0° when the detector is directly facing the incident beam. The goniometer with the sample can be rotated about the sample normal, the y-axis (ϕ angle) and about the x-axis (ψ -tilt angle) to align the sample and to allow for reflections from different crystalline planes.

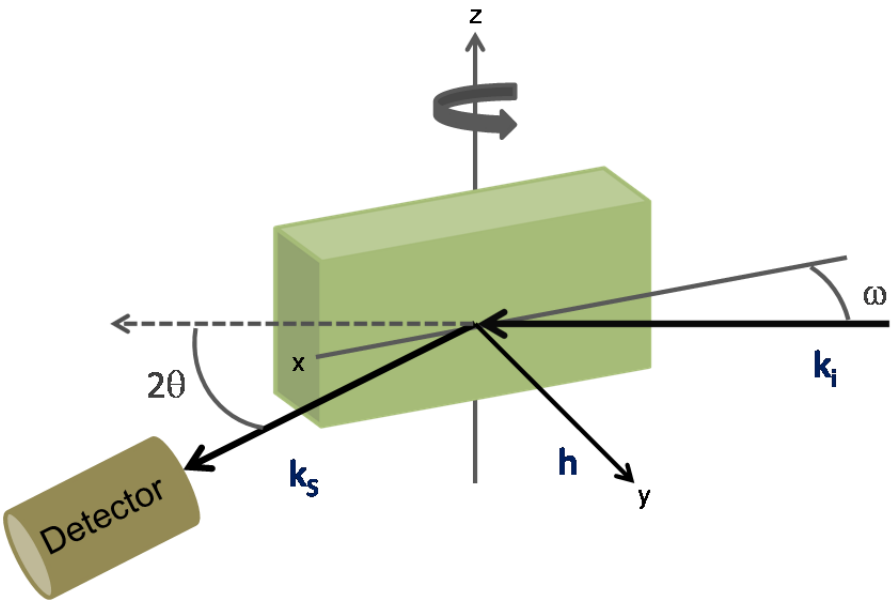

Figure 2.1: Schematic of an experimental set up of x-ray diffraction measurement.

In an x-ray diffraction experiment, a set of lattice planes (*hkl*) is selected according to the incident conditions of the beam and the lattice spacing d_{hkl} is determined by Bragg's law [1]. The diffraction from planes parallel to the sample surface is defined as symmetric scans [Fig. 2.2(a)] and the diffraction from the planes inclined by an angle φ (tilt angle) with respect to the sample surface are defined as asymmetric scans [Fig. 2.2 (b) and (c)]. Symmetric scans provide information about the sample parameters along the growth direction perpendicular to the surface such as perpendicular lattice constant c, the strain component $\varepsilon^{\perp}$ and the layer thickness. Using asymmetric scans, lattice constants both perpendicular and parallel to the surface, and in-plane strain can be calculated.

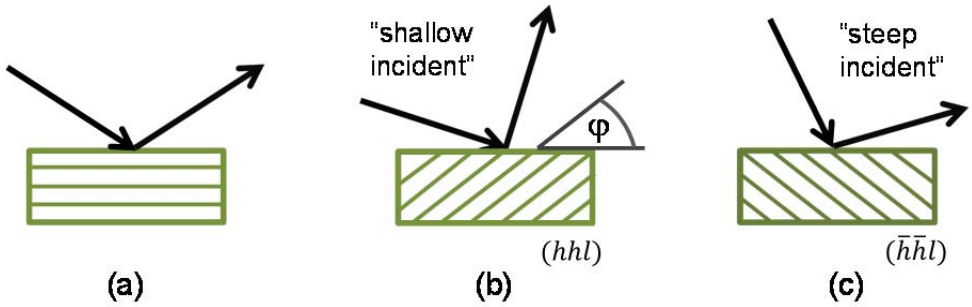

Figure 2.2 Schematic of (a) symmetric diffraction, and two incident conditions (b) shallow and (c) steep for asymmetric diffraction geometries. φ is the layer tilt from the surface for the asymmetric geometry.

2.1.2 Scan modes

Two main scan modes, ω scan and ω-2θ (or 2θ-ω) scan are available to probe the reciprocal lattice points which satisfy the diffraction conditions. The intensity is recorded as a function of ω (θ for 2θ-ω scans). An ω scan is performed with the detector fixed at the $2\theta_B$ position, where θ_B is the Bragg angle, and ω is swept through a few degrees by rotating the sample stage about the diffractometer (z-axis). In ω-2θ scans, the detector is also rotated, but twice as fast as the sample. Generally ω scans are performed to align the sample. In the alignment procedure, the ψ and ϕ angular positions are moved to bring the **h**-vector (normal to the sample surface) and **s**- vector (any other vector on the sample perpendicular to ω and 2θ axes) into the diffracting plane. These angles are optimized by performing ω scans to get the maximum intensities for the substrate peak. For the symmetric scans ψ optimization is sufficient

but for the asymmetric scans both ψ and ϕ optimizations are necessary. Once the alignment procedure is completed, an ω-2θ scan is performed for the desired (*hkl*) reflection.

2.1.3 Layer mismatch, strain and alloy composition

2.1.3.1 Basic definitions

The basic definitions of the physical quantities used to describe a strained heterostructures are given here. The mismatch (*m*) of heteroepitaxial layer is defined as [1]:

$$m = \frac{a_L - a_S}{a_S} \qquad 2.1$$

where a_L and a_S are the unstrained (cubic form) lattice parameters of the epilayer and the substrate, respectively. The two unit cells are assumed to be in the same orientation. The strain induced in the film changes the lattice from cubic to tetragonal or to a lower symmetry lattice. In this case the parallel and perpendicular lattice mismatches with reference to the interface between film and substrate can be written as:

$$\frac{\Delta a^{\parallel}}{a_S} = \frac{a_L^{\parallel} - a_S}{a_S} = \frac{a - a_S}{a_S}, \quad \frac{\Delta a^{\perp}}{a_S} = \frac{a_L^{\perp} - a_S}{a_S} = \frac{c - a_S}{a_S} \qquad 2.2$$

Where $a_L^{\parallel}$=a, and $a_L^{\perp} = c$ are the strained lattice parameters of the layer. Lattice mismatch is the difference between the actual relaxed lattice parameters of the layers forming a heterostructure.

The strain is defined as the relative deformation of the lattice with respect to its bulk parameters induced by a stress. For a cubic lattice the parallel and perpendicular strain are defined as [1]:

$$\varepsilon^{\parallel} = \frac{a_L^{\parallel} - a_L}{a_L}, \quad \varepsilon^{\perp} = \frac{a_L^{\perp} - a_L}{a_L} \tag{2.3}$$

For a cubic lattice, the epitaxial layers grown along <001> direction (coincident with the z-axis) the strain is biaxial and the epilayer lattice parameters are deformed along the interface (x and y directions). Therefore the components of the strain are given by:

$$\varepsilon^{\perp} = -2\frac{c_{12}}{c_{11}}\varepsilon^{\parallel} \tag{2.4}$$

Where, c_{12} and c_{11} are the elastic constants. The Poisson ratio (ν) is defined in terms of elastic constants. For a cubic crystal and for high symmetry directions such as <001>, <011> and <111>, the Poisson ratio is given by:

$$\nu = \frac{c_{12}}{c_{11} + c_{12}} \tag{2.5}$$

Then the misfit can be written in terms of the Poisson ratio and the parallel and perpendicular lattice mismatches.

$$m = \frac{a_L - a_S}{a_S} = \frac{\Delta a^{\perp}}{a_S}\frac{1-\nu}{1+\nu} + \frac{\Delta a^{\parallel}}{a_S}\frac{2\nu}{1+\nu} \tag{2.6}$$

The average bulk lattice parameter for the layer can be calculated from Equation 2.6.

$$a_L = \Delta a^{\perp}\frac{1-\nu}{1+\nu} + \Delta a^{\parallel}\frac{2\nu}{1+\nu} + a_S \tag{2.7}$$

Equation 2.7 can be used to calculate the strain and alloy compositions of heterostructures of the cubic form.

In the case of a pseudomorphic growth, the parallel lattice parameter is matched to that of the substrate, but the perpendicular lattice parameter is deformed along the growth direction due to the effect of biaxial strain. Both in-plane and perpendicular strain components are at their maximum values. In this case the epilayer is said to be completely strained. Then the average lattice constant is given by:

$$a_L = \Delta a^{\perp} \frac{1-\nu}{1+\nu} + a_S \,, \; a_L = (c - a_S) \frac{1-\nu}{1+\nu} + a_S \qquad 2.8$$

where c is the perpendicular lattice parameter of the strained layer.

For lattice mismatched growths beyond a particular critical thickness, the layer changes from pseudomorphic to metamorphic. Then the epilayer is said to be partially relaxed. In a partially relaxed layer both perpendicular and parallel lattice parameters are different from the unstrained values and also from the substrate lattice parameters. The average lattice constant of a partially relaxed layer is calculated by using Equation 2.7 and is given as:

$$a_L = \frac{1-\nu}{1+\nu} c + \frac{2\nu}{1+\nu} a \qquad 2.9$$

where c and a are the perpendicular (out-of-plane) and parallel (in-plane) lattice parameters of the epilayer, respectively.

2.1.3.2 Determination of the lattice parameters, alloy composition and relaxation.

When an alloy composition is derived from symmetric reflections, the layer is assumed to be fully relaxed. If grow thick enough on a mismatched substrate, strain relaxation is accompanied by the onset of misfit dislocations and results in misorientation of the lattice cells (tilt) at the layer-substrate interface [1]. Therefore in general it is more accurate when the alloy composition is derived from asymmetric reflections and the assumption is that the layer is partially relaxed. For the MBE grown structures in this dissertation, the In compositions in InGaAs/InAlAs or Al composition in AlInSb epilayers are determined using asymmetric reflections.

The choice of the asymmetric reflection is limited by the sample orientation, and by the need for a high asymmetry angle to enhance the parallel component of the d_{hkl} spacing [1]. For (001) oriented cubic structures, (335), (224) or (115) asymmetric reflections can be used. In order to determine the In composition in InGaAs, (115) or (335) asymmetric reflections with "shallow" incident (ω^-) [Fig. 2.2(b)] and "steep" incident (ω^+) [Fig. 2.2(c)] geometries were used. The tilt angle φ of the layer from (001) surface can be directly determined using a pair of asymmetric reflections, *hhl* and *-h-hl* [2]. On the other hand, the misorientation of the layer planes ($\alpha=\Delta\varphi$) with respect to the substrate lattice planes can be eliminated by choosing azimuthal angle ϕ differing by π. For this case, measurements need to be taken at $\phi=0°$ (ω^-) and $\phi=180°$ (ω^+) for a selected asymmetric reflection (*hhl*). For each reflection, ω-2θ scans were performed and the peak positions were recorded. Figure 2.3 shows the intensity profile recorded by

ω-2θ scan for (004) and (115) reflections. The tilt angle φ and lattice parameters *a* and *c* are calculated using the peak separations.

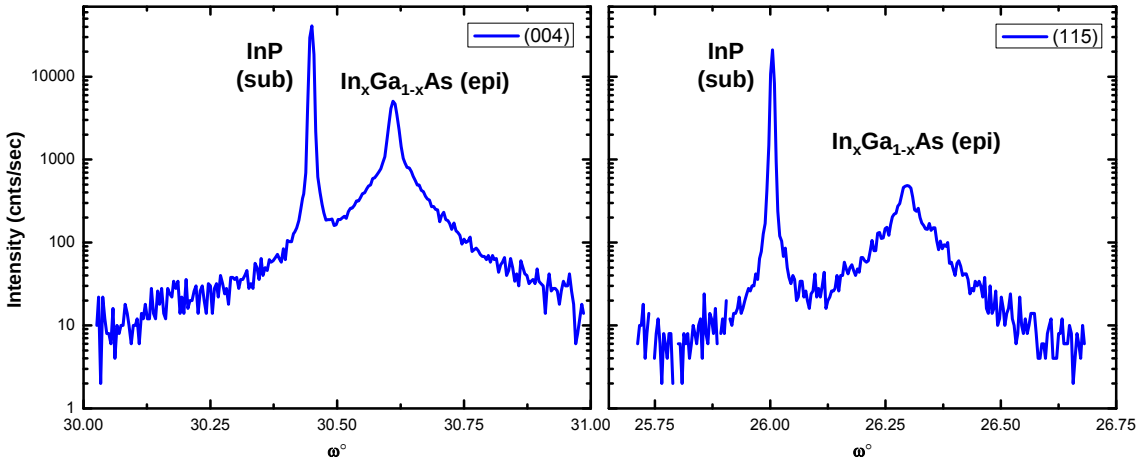

Figure 2.3: HRXRD Intensity profiles for symmetric and asymmetric reflections. The sample number is P019. The Bragg angle difference between the substrate and the layer is determined by the peak separations. The peak parameters are listed in Table 2.1 and Table 2.2 for symmetric and asymmetric reflections, respectively.

The lattice plane spacing d_{hhl}, the Bragg angle θ_B and the plane tilt angle φ for *hhl* reflection are related by the following equations [3].

$$\frac{1}{d_{hhl}} = \frac{2\sin\theta}{\lambda} = \sqrt{\frac{2h^2}{a^2} + \frac{l^2}{c^2}} \qquad 2.10$$

$$\cos\varphi = \frac{l/c}{\sqrt{\frac{2h^2}{a^2} + \frac{l^2}{c^2}}} \qquad 2.11$$

From Equations 2.10 and 2.11, *c* and *a* can be obtained:

$$c = \frac{\lambda l}{2 \sin\theta \cos\varphi} \qquad \text{and} \qquad a = \frac{ch}{l}\sqrt{2}\cot\varphi \tag{2.12}$$

The Bragg angle difference between the layer and the substrate $\Delta\theta$ is given by the average of the peak separations $\Delta\omega_1$, and $\Delta\omega_2$ for the (ω^-) and (ω^+) incident geometries, respectively.

$$\Delta\theta = \frac{\Delta\omega_1 + \Delta\omega_2}{2} \tag{2.13}$$

The tilt between the layer and the substrate $\Delta\varphi$ is half the difference of the two peak separations for the (ω^-) and (ω^+) reflections and it is given by:

$$\Delta\varphi = \frac{\Delta\omega_1 - \Delta\omega_2}{2}, \tag{2.14}$$

The tilt of the layer φ from (001) surface is directly calculated from half the difference of the two peak positions ω^- (*hhl*) and ω^+ (*-h-hl*) [2].

$$\varphi = \frac{\omega_2 - \omega_1}{2} \tag{2.15}$$

Calculations:

The out-of-plane lattice constant c is calculated from (004) reflections, using equation 2.12. In this case, ω^- and ω^+ correspond to ϕ=0° and ϕ=180° incidences and φ=$\Delta\varphi$. The corrected Bragg angle for the layer is given by:

$$\theta = \theta_S - \Delta\theta \tag{2.16}$$

where θ_S (=31.669°) is the substrate (InP) Bragg angle for the (004) reflection and can

be calculated by setting h=0, λ=1.5406Å and c=a=5.8687Å in above the formula. From θ_B=31.8263° and $\Delta\varphi$=0.004°, c is calculated. The values are given in Table 2.1.

	Substrate (InP)			Epilayer ($In_xGa_{1-x}As$)					
h k l	θ_S (theor.)	ω^- (ϕ=0°)	ω^+ (ϕ=180°)	ω^- (ϕ=0°)	ω^+ (ϕ=180°)	$\Delta\theta$	$\Delta\varphi$	θ_B	c (Å)
0 0 4	31.669	30.4499	33.1519	30.6112	33.3052	-0.1573	0.004	31.8263	5.8427
$\Delta\omega$				-0.1613	-0.1533				

Table 2.1: X-ray diffraction data obtained from (004) reflections and calculated lattice parameters for $In_xGa_{1-x}As$ grown on an InP (001) substrate.

The in-plane lattice constant a is calculated from asymmetric reflections (115) and (-1-15) by using the formula, $a = \frac{ch}{l}\sqrt{2}\cot\varphi$ and calculated c value from (004) reflection. The parameters are given in Table 2.2.

The bulk lattice constant a_L is calculated using Equation 2.9 with ν=0.33 and is found to be; a_L =5.8582Å.

	Epilayer ($In_xGa_{1-x}As$)					
h k l	ϕ	ω^-	ω^+	φ	φ_{ave}	a (Å)
1 1 5	0	26.2959	57.7202	15.7121	15.7104	5.8751
	180	28.9935	60.4111	15.7088		

Table 2.2: X-ray diffraction data obtained from (115) and (-1-15) reflections and calculated in-plane lattice parameter for $In_xGa_{1-x}As$ grown on a InP (001) substrate.

The Indium composition *x* in $In_xGa_{1-x}As$ is calculated using Vegard's law. In an alloy A_xB_{1-x}, the lattice parameter $a_L(x)$ is proportional to the stoichiometric coefficient x:

$$a_L(x) = xa_A + (1-x)a_B \ , \ x = \frac{a_L - a_B}{a_A - a_B} \qquad 2.17$$

$$x_{InGaAs} = \frac{a_L - a_{GaAs}}{a_{InAs} - a_{GaAs}}, \qquad x = \frac{5.8582 - 5.6533}{6.0583 - 5.6533} = 0.506$$

The calculated In composition of $In_xGa_{1-x}As$ is 50.6%.

The percentage relaxation is given by:

$$R\% = \frac{a - a_S}{a_L - a_S} 100\% \qquad 2.18$$

$$R = \frac{5.8751 - 5.8687}{5.8582 - 5.8687} 100\% = -60.9\%$$

The calculated percentage relaxation is -60.9%. The layer is said to be 100% (0%) relaxed (completely strained) when *a* equals to the lattice constant of bulk alloy, a_L (substrate, a_S).

2.1.4 XRD Simulation

For pseudomorphic growths or for very thin layers, the peak separation depends at the same time on the composition, strain and the thickness of the epilayer. In this case, simulations are performed and the composition is determined by the simulation profile that best fits the experimental diffraction profile. Figure 2.4 shows an ω-2θ scan and the best fit simulation curve of the (004) reflection for a MBE grown InP(001)/100nm $In_{0.52}Al_{0.48}As$/300nm $In_{0.53}Ga_{0.47}As$ structure. The X'pert Epitaxy

software uses the Takagi-Taupin theory to calculate the intensity diffracted by strained heteroepitaxial structures of the cubic form [4]. A background intensity of 5cnts/sec, noise of 0.1cnts/sec, and diffuse scattering of 130cnts/sec were added to the simulation curve to match with the experimental XRD intensity profile. The thickness of 96nm (298nm) and the In composition of 50.6% (51.9%) for InAlAs (InGaAs) layer were deduced from the simulation curve.

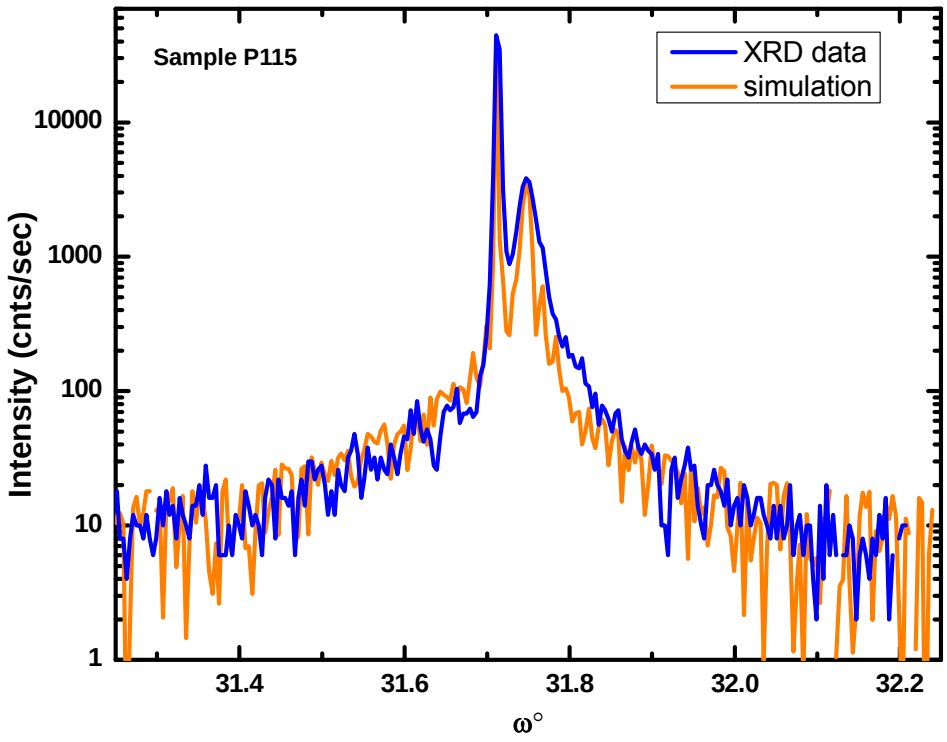

Figure 2.4: (004) HRXRD ω-2θ scan and the simulation curve for MBE grown InP(001)/100nm $In_{0.52}Al_{0.48}As$/300nm $In_{0.53}Ga_{0.47}As$ structure. The compositions and the layer thicknesses deduced from the best fit simulation are given by InP(001)/96nm $In_{0.506}Al_{0.494}As$/ 298nm $In_{0.519}Ga_{0.481}As$.

2.1.5 Determination of the layer thickness

For the diffraction from a thin nearly-perfect heteroepitaxial layer, thickness fringes arise. The layer thickness (t) is related to the spacing of the thickness fringes (δω) by the formula given bellow [4].

$$\delta\omega = \frac{\lambda \sin e}{t \sin 2\theta_{av}} \qquad 2.19$$

where *e* is the angle between the diffracted beam and the sample surface, which is given by ($2\theta_{av}$ - ω) and $2\theta_{av}$ is the average value of 2θ for the two fringes. δω is the peak separation for the two thickness fringes and is measured in radians.

When thickness fringes are not seen for diffraction from a single layer, the layer thickness (t) is related to the full width at half maximum, β (FWHM) of the diffraction peak by the formula (Scherrer equation) [5]:

$$\beta = \frac{0.89\lambda}{t \cos \theta_l} \qquad 2.20$$

where 0.89 is the Scherrer constant and θ_l is the peak position of the (*00l*) reflection for the layer. For an example, the thicknesses of the Sb films grown on GaSb (111)A substrates determined using this formula are given in Chapter 5.

2.2 Hall Effect measurement

The classical Hall Effect measurement is one of the most common and most useful electrical characterization techniques for semiconductors. Electrical transport

properties such as resistivity, carrier density, carrier type and the mobility of a QW or an epilayer can be determined using this technique. In the Classical limit, the transport fundamentals are derived according to the simple Drude model approximation.

2.2.1 Drude Model

In the Drude model, valence electrons in a solid or a metal are considered as a free electron gas and are free to move, whereas ions or heavy positive charges are considered to be immobile [6]. Moreover it assumes that electrons change their velocity by bouncing off ion cores and therefore electron-electron collisions are ignored. The mean time between collisions τ, or the relaxation time, is independent of the velocity and the position of the electron. Under an electric field, electrons drift with an average velocity, v_d.

2.2.2 Electrical conductivity

According to the Drude model under an electric field the current density in a conducting wire is given by Ohm's law:

$$\boldsymbol{E} = \rho \boldsymbol{j} \qquad 2.21$$

Where, $\boldsymbol{E}$ is the electric field, $\boldsymbol{j}$ is the current density and ρ is the resistivity (proportionality constant between $\boldsymbol{E}$ and $\boldsymbol{j}$) of the wire and depends only on the material properties. The resistivity is related to the resistance by $R=\rho L/A$, where L is the length

and A is the cross-sectional area of the wire. If the wire has *n* electrons per volume moving with velocity v_d, the current density can be expressed as:

$$\boldsymbol{j} = -ne\boldsymbol{v_d} \text{ , and } \boldsymbol{v_d} = \frac{e\boldsymbol{E}\tau}{m} \quad 2.22$$

where *e* is the electron charge and *m* is the electron mass. From 2.22, current density can be written as:

$$\boldsymbol{j} = \sigma_0 \boldsymbol{E} \text{ ,} \quad 2.23$$

where σ_0 is the electrical conductivity and is given by:

$$\sigma_0 = \frac{ne^2\tau}{m} = \frac{1}{\rho} \quad 2.24$$

and mobility, μ is defined as:

$$\mu = \frac{e\tau}{m} \quad 2.25$$

2.2.3 Hall Effect

When a current passes across a conducting sheet placed under an external weak magnetic field (**B)** perpendicular to the surface, an electric field develops in the opposite edges on the surface perpendicular to the current and the magnetic field directions. Electrons deflect to an opposite edge until steady state is reached. This is known as the Hall Effect [6]. The voltage drop is perpendicular to the current direction is called the Hall voltage. Once the steady-state conditions are reached, the Lorentz force is balanced

by the Hall voltage and current continues to flow across the sample independent of the B field. The equation of motion for the electrons at the steady state is given by:

$$-e(\boldsymbol{E} + \boldsymbol{v_d} \times \boldsymbol{B}) = \frac{m\boldsymbol{v_d}}{\tau} \quad 2.26$$

This can be written in the tensor form:

$$\begin{bmatrix} E_x \\ E_y \end{bmatrix} = \begin{bmatrix} \frac{m}{e\tau} & -B \\ B & \frac{m}{e\tau} \end{bmatrix} \begin{bmatrix} v_x \\ v_y \end{bmatrix}, \quad 2.27$$

By using $\boldsymbol{j}$=-ne$\boldsymbol{v_d}$ and μ=eτ/m, equation 2.27 can be rewritten in the form:

$$\begin{bmatrix} E_x \\ E_y \end{bmatrix} = \sigma^{-1} \begin{bmatrix} 1 & -\mu B \\ \mu B & 1 \end{bmatrix} \begin{bmatrix} j_x \\ j_y \end{bmatrix}, \quad 2.28$$

where, σ=enμ is the zero B field conductivity.

The resistivity tensor can be written in the same form:

$$\begin{bmatrix} E_x \\ E_y \end{bmatrix} = \begin{bmatrix} \rho_{xx} & \rho_{xy} \\ \rho_{yx} & \rho_{yy} \end{bmatrix} \begin{bmatrix} j_x \\ j_y \end{bmatrix} \quad 2.29$$

where, $\rho_{xx} = \frac{1}{\sigma} = \frac{1}{en\mu}$ 2.30

and $\rho_{xy} = -\rho_{yx} = \frac{1}{en} B$ and 2.31

ρ_{xx} is called the longitudinal resistivity and ρ_{xy} is called the transverse resistivity or Hall resistivity and linearly increases with B in the low field limit. R_H= -1/en is known as the Hall coefficient. The sign is opposite for holes.

2.2.4 Hall Effect measurement and the van der Pauw geometry

The sheet carrier density, the resistivity and the mobility of the conducting sample is experimentally determined by the Hall measurement in the van der Pauw geometry. While the Hall effect measurement can be performed in a lithographically defined Hall bar, we prefer to use a square specimen directly cleaved from a MBE grown wafer. For the samples described in this dissertation, the Hall measurement was performed on a square specimen [Fig. 2.5]. Pure In or an In-Zn alloy (for *p*-type InSb QWs) was applied at the corners of the sample for ohmic contacts. Temperature-dependent Hall measurements were done in a closed-cycle He refrigerator from 300K to 20K. Poor ohmic contacts can freeze out at low temperature; therefore, contacts were annealed at 230°C for ~7min (for InSb QWs) or ~400°C for ~10min (for InGaAs QWs) in a H_2 (~20%) and N_2 (~80%) environment. Detailed discussion of mobility and density and limiting factors are given in Chapter 3.

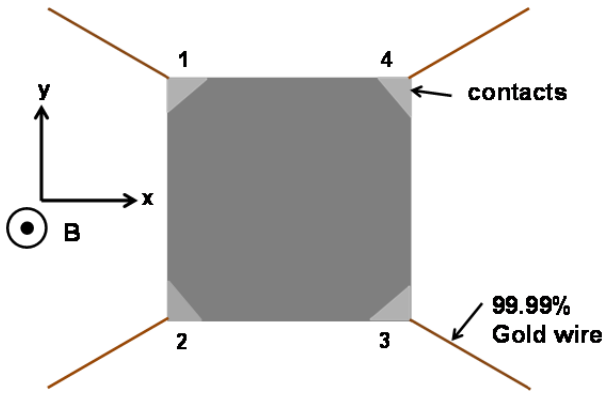

Figure 2.5: Square geometry of samples used for the Hall measurements. Magnetic field B is applied along the z-direction perpendicular to the sample surface.

At steady state, transverse current is zero (j_y=0), therefore , from equation 2.29,

$$E_x = \rho_{xx} j_x \; ; \quad E_y = \rho_{yx} j_x \tag{2.32}$$

From equation 2.32 and 2.31, transverse resistivity is given by:

$$\rho_{xy} = \frac{V_H}{I} = -\frac{1}{en_s} B \tag{2.33}$$

where V_H is the transverse voltage drop and is measured between contacts 2 and 4 (V_{24}) while a constant current, I is passed between 3 and 1 (I_{31}) with a perpendicular magnetic field. Here n_s is the sheet carrier density and is related to the bulk concentration, $n=n_s/t$, where t is the thickness of the conducting layer. The sheet carrier density is determined from the Hall coefficient (R_H), the slope of transverse resistivity versus B field. Typically the B field is swept between 0 and 0.12T for the low field limit. A linear Hall relationship is observed for a single carrier type, (electrons or holes) and the carrier type is determined by the sign of V_H. V_H is positive (negative) if the carriers are electrons (holes).

$$n_s = -\frac{1}{e} \frac{1}{\left(\frac{d\rho_{xy}}{dB}\right)} \tag{2.34}$$

Mobility is calculated using the longitudinal resistivity at B=0 (equation 2.30) and the calculated carrier density as given in equation, 2.34.

$$\mu = \frac{1}{en_s \rho_{xx}} \tag{2.35}$$

From equation 2.32 longitudinal resistivity, in this case the sheet resistivity, at B=0 is given by:

$$\rho_{xx} = \frac{V_x}{I}$$

The longitudinal resistivity or the sheet resistivity of the sample is measured according to the van der Pauw geometry [7] with **B**=0. Van der Pauw described a method to determine the sample resistivity independent of its shape and the size. In this technique, the sample is assumed to be homogenous in thickness and carrier density, and very large in comparison to the point-like contacts which are placed at the boundaries. Then the longitudinal resistivity is given by the formula:

$$\rho_{xx} = \frac{\pi}{ln2}\left[\frac{R_{12,43}+R_{43,12}+R_{23,14}+R_{14,23}}{4}\right] f\left[\frac{R_{12,43}+R_{43,12}}{R_{23,14}+R_{14,23}}\right] \qquad 2.36$$

where, $R_{12,43}$ is the four point resistance and given by;

$R_{12,43} = \frac{V_{12}}{I_{43}}$,

V_{12} is the dc voltage drop between contacts 1 and 2 when the current I is passed from contact 4 to 3.

$R_{43,12}$, $R_{23,14}$, $R_{14,23}$ are defined similarly. f is the correction term for the arbitrary shape of sample. For a square sample with small contacts, f is 1. Then the longitudinal resistance can be written as;

$$\rho_{xx} = \frac{\pi}{ln2} R_{av} \text{ , where, } R_{av} = \left[\frac{R_{12,43}+R_{43,12}+R_{23,14}+R_{14,23}}{4}\right] \qquad 2.37$$

The previous calculation has assumed that only one type of carrier with a single mobility is present in the system. This is true at all temperatures for most of the 2D

systems doped with electrons, but for some *p*-type doped InSb QWs at room temperature, non-linear Hall curves were observed due to the presence of intrinsic electrons. For the case where both electrons and holes are present, the Hall coefficient is given by [8]:

$$R_H = \frac{p\mu_h^2 - n\mu_e^2}{e(p\mu_h + n\mu_e)^2} \qquad 2.38$$

where, p and n are 2D electron and hole densities, respectively. μ_h and μ_e are hole and electron mobilities, respectively.

Chapter 3

2D Electron Systems in InSb and $In_yGa_{1-y}As$ Quantum Well Structures

3.0 Introduction

Among III-V materials InSb and InGaAs are promising candidates for future high speed, ultra-low-power digital logic applications, because of higher electron mobility and saturation velocity. A comparison of III-V *n*-type quantum-well field effect transistors (QWFETs) with standard silicon metal oxide semiconductor FETs (MOSFETs) shows that the energy-delay product, an important figure of merit, is more favorable (lower the better) for the FETs made of InSb and InGaAs quantum wells [1]. However, a major challenge is to find a suitable gate dielectric stack compatible with III-V channel FETs in order for these devices to be used in digital logic applications.

This chapter is organized as follows. The first section discusses the growth of *n*-type InSb QWs and the dependence of the electrical properties on structural parameters with a goal of high mobility electrons. The second section discusses the growth of remotely doped *n*-type $In_yGa_{1-y}As$ QWs with $In_xAl_{1-x}As$ barriers and their electrical properties. Growth of undoped $In_yGa_{1-y}As$ QWs with $In_xAl_{1-x}As$ barriers for MOSFET applications and epilayers for development of high-κ dielectric integration is discussed in the third section. This project was a collaboration with Intel Corp. and others for which we provided $In_yGa_{1-y}As/In_xAl_{1-x}As$ layer structures for the high-κ dielectric experiments.

3. 1.0 High electron mobility InSb quantum well structures

InSb has the narrowest band gap (0.18eV at room temperature) and the smallest effective mass for the electrons ($0.014m_e$) of all the III-V's which leads to the highest intrinsic mobility for electrons. InSb also exhibits the highest saturation velocity for electrons (5×10^7 cm s^{-1}) [2]. These characteristics make InSb a promising candidate for ultra-high speed low power electronic devices [3] and ballistic transport devices [4, 5]. QWFETs fabricated from an InSb QW with a remotely doped $Al_xIn_{1-x}Sb$ barrier have already demonstrated the highest switching speed and lowest power dissipation in a comparative study with other III-V QWFETs and Si MOSFETs [6]. Because of the large spin-orbit effects for electrons InSb is also an attractive material for spintronic devices [7].

The quantum confinement and the mobility of the InSb QWs can be increased by further optimization of the layer structure, doping and growth parameters. Increased carrier mobility and density in these structures will lead to improved device performance. Therefore the growth and the study of the dependence of the electrical properties on structural parameters are motivated by the potential for producing high mobility electrons for device applications and for the basic research on quantum transport.

3.1.1 Simplified method of calculating the electron density in an *n*-type QW with a single δ-doping layer placed a distance *d* from the well

In a finite potential well, electrons are free to move in the x-y plane and are confined in the z-direction (growth direction). The quantum confinement leads to the quantization of the electronic states (subbands). A simple method of calculating the electron density for a QW δ-doped on one side and with one occupied subband is given here. Figure 3.1 shows a schematic energy diagram.

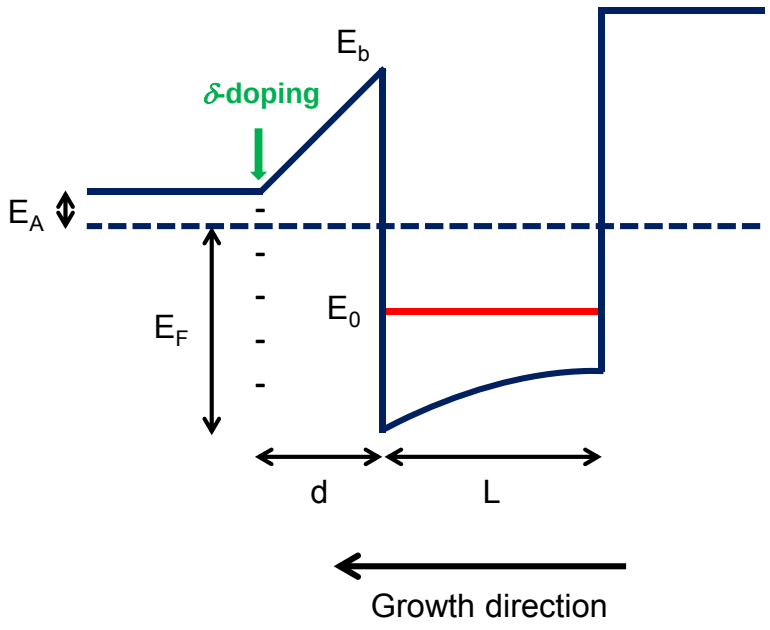

Figure 3.1: Schematic energy diagram of a QW with single δ-doping layer.

At low temperature, the electron density in the well with a single occupied subband (ground state) is calculated by integrating the two-dimensional density of states, $D(E) = m^*/\pi\hbar^2$ and given by Equation 3.1 [8]:

$$n = \frac{m^*}{\pi\hbar^2}(E_F - E_0) \quad (3.1)$$

where m^* is the in-plane effective mass, E_F is the Fermi level energy, and E_0 is the ground state energy. From this equation E_F can be written as:

$$E_F = \frac{\pi\hbar^2 n}{m^*} + E_0 \quad (3.2)$$

Assuming that the Fermi level is pinned to the conduction band edge at the δ-doped layer, the electric field in the spacer layer can be written as:

$$\frac{qn}{\varepsilon} = \frac{E_b - E_F - E_A}{qd} \quad (3.3)$$

where E_b is the barrier height. The left hand side of the Equation 3.3 is obtained from Poisson's Equation, where q is the charge of the electron and ε is the permittivity of the well material ($\varepsilon = 18\varepsilon_0$ for InSb). In the right hand side, E_A ($=13.6m^*/\varepsilon^2$ eV) is the activation energy of the ionized dopants and d is the spacer layer thickness. Substituting E_F in Equation 3.3 and rearranging gives:

$$n = \frac{E_b - E_0 - E_A}{\frac{\pi\hbar^2}{m^*} + \frac{q^2 d}{\varepsilon}} \quad (3.4)$$

In general, $E_b > (E_A + E_0)$ is necessary to populate the QW. E_A is ignored since E_A is much smaller than E_b and E_0. The electron density dependence on the spacer layer thickness d can be expressed as:

$$n \approx \frac{E_b - E_0}{\frac{\pi\hbar^2}{m^*} + \frac{q^2 d}{\varepsilon}} \quad (3.5)$$

The barrier height of $Al_xIn_{1-x}Sb$ can be calculated by assuming that the 62% of the band offset appears in the conduction band for InSb [9]. E_0 can be calculated using the energies predicted by the infinite potential well approximation.

$$E_0 = \frac{\pi^2 \hbar^2}{2m^* L^2} \quad 3.6$$

Where, L is the thickness of the QW. The electron density in the well depends on the spacer layer thickness when the donor density N_d is larger than the electron density predicted by the Equation 3.5. For smaller N_d, the electron density is simply equal to N_d.

3.1.2 Design parameters and the factors limiting electron density and mobility in InSb QWs

Fabrication of a high quality two-dimensional electron gas (2DEG) is challenging due to the lack of suitable substrate and barrier materials for InSb QWs. For this reason GaAs substrate and $Al_xIn_{1-x}Sb$ buffer/barrier layers are often used. The design parameters for InSb QWs with $Al_xIn_{1-x}Sb$ barrier layers are QW width (L), doping density (N_d), spacer layer thickness (d), and the barrier height (E_b), besides the buffer layer structures. In order to obtain high carrier density, according to equations 3.5 and 3.6, a wider well and a higher barrier height are required. A thicker well, below the critical thickness, can be grown on an $Al_xIn_{1-x}Sb$ buffer layer with low x (Al composition). But for high barrier heights, $Al_xIn_{1-x}Sb$ buffer layers with high x are required. A strain balanced InSb QW structure design would allow one to grow a thicker well on a low x $Al_xIn_{1-x}Sb$ buffer layer while having high x barrier layers [10].

In this design, InSb QW and high x $Al_xIn_{1-x}Sb$ barrier layers are compressively and tensilely strained to the low x thick relaxed $Al_xIn_{1-x}Sb$ buffer layer, respectively. The well width and the barrier thickness are calculated such that the compressive strain in the InSb well is balanced by the tensile strain in the high x $Al_xIn_{1-x}Sb$ barrier layers.

On the other hand, higher mobility (>100,000cm^2/Vs at low temperature) with lower density (~$2.5\times10^{11}cm^{-2}$) is required in order to obtain a gate-controled 2DEG in gated InSb QWs using a top gating approach [11]. Mobility at low temperature is limited by the defects from lattice mismatched growth and ionized dopant scattering arising from the Si δ-doping layer that provides the electrons to the well. The two δ-doping layers with optimal doping densities are necessary to avoid parallel conduction through the δ-doping layers. The δ-doping layer near the surface needs to be placed away from the well in order to minimize the ionized dopant scattering. This distance is limited by the requirement of a shallow well (a short distance to the surface from the well) for the fabrication of a top gate with gate dielectric depositions and gate controllability of carrier density in InSb QWs [11]. The shallow QWs are also beneficial for other device processing techniques such as optical and electron beam (E-beam) lithography.

3.1.3 Layer structure of remotely doped InSb QWs.

All the InSb/$Al_xIn_{1-x}Sb$ heterostructures were grown on semi-insulating, off axis (2° off [001] toward [110]) GaAs(001) substrates by MBE. A typical layer structure for an asymmetrically doped InSb QW with an interlayer buffer is shown in Figure 3.2.

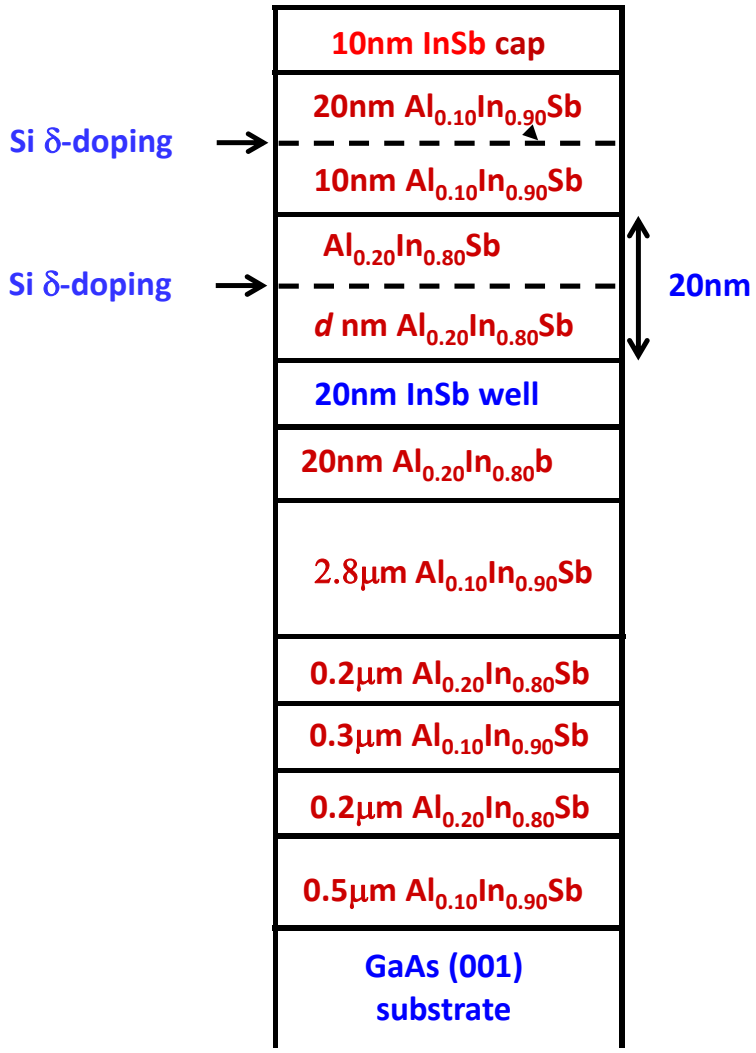

Figure 3.2: The layer structure of asymmetrically doped InSb QW with $Al_{0.20}In_{0.80}Sb$ barrier layers.

Due to the large lattice mismatch (~14.5%) between GaAs and InSb, structural defects such as microtwins (MT) and threading dislocations (TD) are created during the growth of the buffer layers [12]. These defects at the QW layer limit the electron mobility in the well and depend strongly on the Al composition of the buffer layers located between the substrate and the lower barrier layer [13]. A 2° off axis GaAs substrate is chosen to reduce the MTs density at the QWs [14]. The buffer layers as

shown in Fig 3.2, in growth order, consist of an initial 0.5μm thick $Al_{0.10}In_{0.90}Sb$ layer followed by two $Al_{0.20}In_{0.80}Sb$ interlayers separated by a 0.3μm $Al_{0.10}In_{0.90}Sb$ matrix layer and a 2.8μm thick relaxed $Al_{0.10}In_{0.90}Sb$ buffer layer. Two $Al_{0.20}In_{0.80}Sb$ interlayers were introduced in the buffer to reduce the density of TDs that propagate to the QW [13, 15]. The matrix layers, interlayers and the thick buffer layer were grown at a substrate temperature of 380°C with a V/III flux ratio of 1.2-1.3 after the initial oxide desorption at ~640°C -650°C under an Sb_2 flux.

The strain-balanced 20nm thick InSb QW is sandwiched between $Al_{0.20}In_{0.80}Sb$ barrier layers on the $Al_{0.10}In_{0.90}Sb$ relaxed buffer layer. Since the compressive strain of the InSb is balanced by the tensile strain of the $Al_{0.20}In_{0.80}Sb$ barrier layers, a thicker QW (than would be possible on a relaxed $Al_{0.20}In_{0.80}Sb$) can be grown on the relaxed $Al_{0.10}In_{0.90}Sb$ layer [9]. To supply electrons to the well, a single Si δ-doped layer is placed in the upper barrier a distance 10 nm ≤ d ≤ 18nm above the InSb QW in order to minimize the ionized dopant scattering. A second Si δ-doped layer (donor density of ~3.0-3.6×10^{11} cm^{-2}) placed in the $Al_{0.10}In_{0.90}Sb$ cap layer near the surface, provides electrons to surface states. The InSb cap layer minimizes the oxidization of the $Al_{0.10}In_{0.90}Sb$ layers underneath. The InSb QW, two Si- delta doping layers and the cap layers were grown at 35°C below the transition temperature where the pseudo (1×3) reconstruction of the $Al_{0.10}In_{0.90}Sb$ surface changes to c(4×4) to obtain maximum doping efficiency [16]. The growth rate of the QW layer is ~0.52 ML/s and the V/III ratio is kept at ~1.3.

3.1.4 Electron mobility and density in remotely doped InSb QWs

All the InSb QWs were characterized by the Hall and van der Pauw methods [Sec. 2.2] on ~8×8 mm^2 samples in magnetic fields up to 0.13 T over the temperature range from 300K to 20K in a closed cycle He refrigerator. Four electrical contacts were made at each corner of a sample by annealing In at 230°C in a H_2(~20%) and N_2(~80%) environment (in order to minimize the surface oxidization) for ~7min. Ohmic contact was checked through observation of linear current voltage characteristics at 300K, 150K, 77K and 25K. A linear Hall voltage with applied magnetic field was observed for all the samples at all temperatures. Fig 3.3 shows the typical temperature dependence of the mobility and density for an *n*-type InSb QW. The electron density (mobility) decreases (increases) as the temperature decreases and saturates at low temperature. A high mobility of 229,500cm^2/Vs with a density of $2.9\times10^{11}cm^{-2}$ was achieved. The Hall data for a series of asymmetrically doped InSb QWs is given in Appendix A Table A.1.

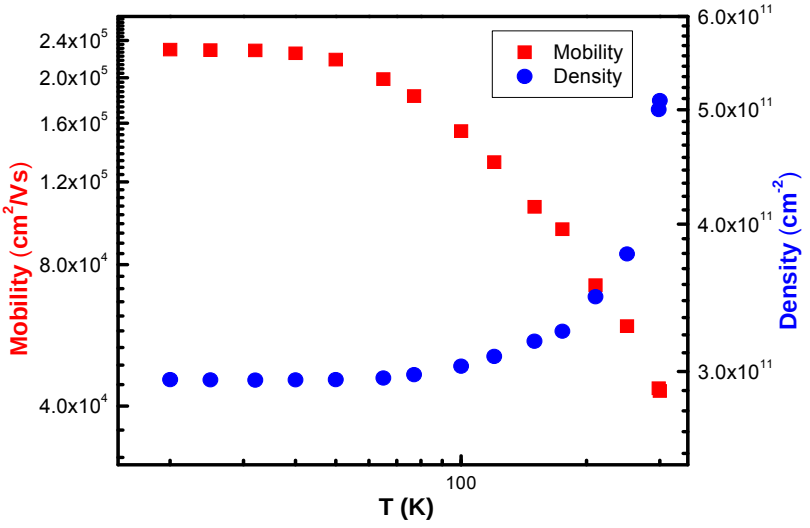

Figure 3.3: Density and mobility of InSb QW structure (t341) as a function of temperature.

Three structures which had identical layer structures as shown in Fig 3.2 except without the InSb cap layer, and the same donor density (N_D~ 3.6×10^{11} cm^{-2}) in both Si δ-doped layers were grown with different spacer layer thickness *d*. Mobility and density as a function of temperature for these structures are shown in Fig. 3.4. The mobility in all the samples at 300K is lower than at low temperature. The mobility at higher temperatures is limited by polar optical phonons [17]. The effect of scattering by defects of the mobility is important at all temperatures. The mobility at any temperature is higher for the structure with *d*=15nm compared to the structure with *d*=10nm. A decrease in the carrier density (by factor of 1.5) which is expected according to the equation 3.5 is observed for this structure.

The mobility at low temperature is limited by the scattering from ionized dopants, unintentional ionized background impurities in the $Al_xIn_{1-x}Sb$ layers, and a rough interface between well and barrier. A low-temperature mobility limited by interface roughness scattering has been observed in InSb QWs for a well thickness of ≤ 20nm [18]. A strong dependence of low temperature mobility on the spacer layer thickness implies that the effect of ionized dopant scattering would be more significant than the interface roughness scattering in our InSb QW structures.

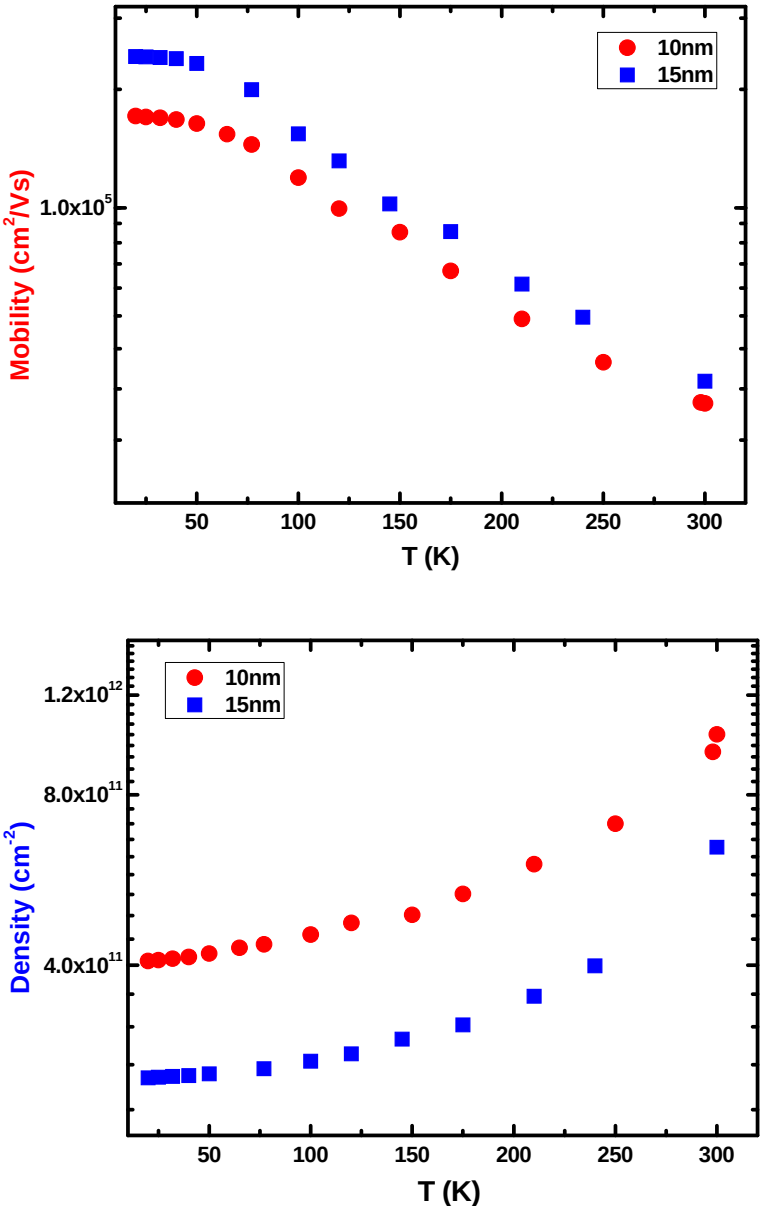

Figure 3.4: Temperature dependence of electron (a) mobility and (b) density of InSb QWs with different spacer layer thickness.

The dependence of mobility and density of the well on the spacer layer thickness at low temperature are shown in Fig. 3.5 with two additional samples. As shown in Figure 3.5, both the highest mobility and the highest density are observed in structure with *d*=15nm and an InSb cap layer. The reduced ionized dopant scattering in structure t335 resulted in a highest mobility of 251,000 cm^2/Vs and density of 3.1×10^{11} cm^{-2} at 25K. An improvement in the room temperature mobility of 44,700 cm^2/Vs and density of 5.4×10^{11} cm^{-2} were also observed in this structure. The δ-doped layer near the well was placed in the lower barrier below the QW with the same doping density and *d*=15nm for the structure t350. The mobility at 25K in this structure is however a factor of ~2.3 lower than that of the other two structures with *d*=15nm. An increase in the carrier density ($5.4\times10^{11}cm^{-2}$) by a factor of ~2 was also observed in this structure compared to the other two structures with *d*=15nm at 25K. The high carrier density in this structure could be due to the migration of dopants in to the well, which would also increase the ionized dopant scattering in this structure. However further studies are needed in order to make a strong conclusion.

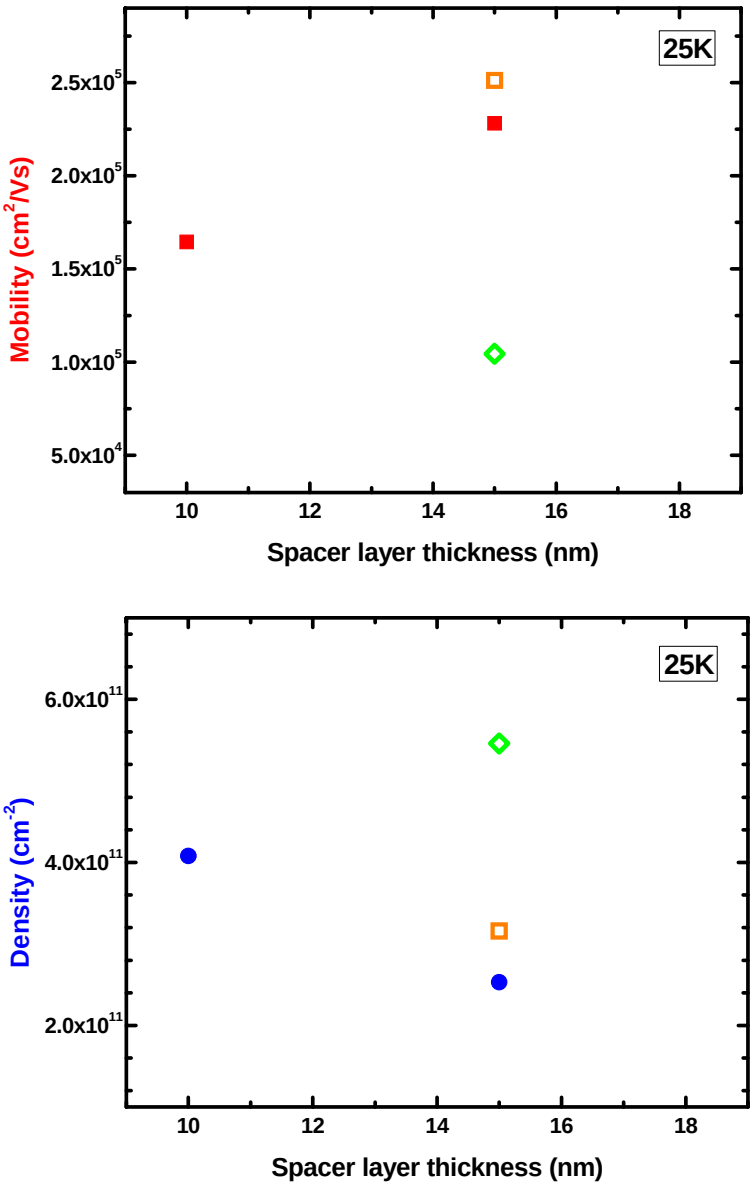

Figure. 3.5: The dependence of (a) mobility and (b) density with spacer layer thickness at 25K. Open square and diamond symbols represent the structure t335 with an InSb cap layer, and the structure t350 with the δ-doped layer in the lower barrier below the QW, respectively.

The effect of the doping concentration on the mobility and density was also studied. In order to achieve lower density, doping near the well needs to be lowered. QW structures, as shown in Fig. 3.2 with d=15nm, were grown with different donor concentrations in the δ-doped layers. Table 3.1 summarizes the δ-doping densities in these structures along with the carrier mobility and density. The carrier mobility and density as a function of temperature for these structures are compared in Fig. 3.6.

Sample	δ-doping ($\times 10^{11}$ cm^{-2})		Average density (cm^{-2})		Average mobility (cm^2/Vs)	
	surface	well	20K	300K	20K	300K
t335	3.6	3.6	3.1	5.4	251,000	44,700
t339	3.6	1.8	2.0	3.6	171,500	39,800
t397	3.0	0.9	1.6	3.7	139,200	37,600
t402	3.0	0.7	1.0	2.6	84,500	35,300

Table 3.1: A comparison of mobility and density in InSb QWs with different Si δ-doping concentrations.

Both density and mobility decreased as the doping density near the well is decreased. Screening of scattering potentials from the electrons in the δ-doping plane at high doping density is also important in enhancing the mobility [19]. As the doping density increases, the increased occupation in the doping plane results in increased a screening and reduces the ionized dopant scattering. Since parallel conduction was not evident (t339), the observed low mobility at low doping structures could be due to the unscreened ionized dopant scattering. It has been observed that the screening of remote

ionized dopant scattering by electrons in the δ-doped plane has less effect on mobility for low doped InSb QWs [19].

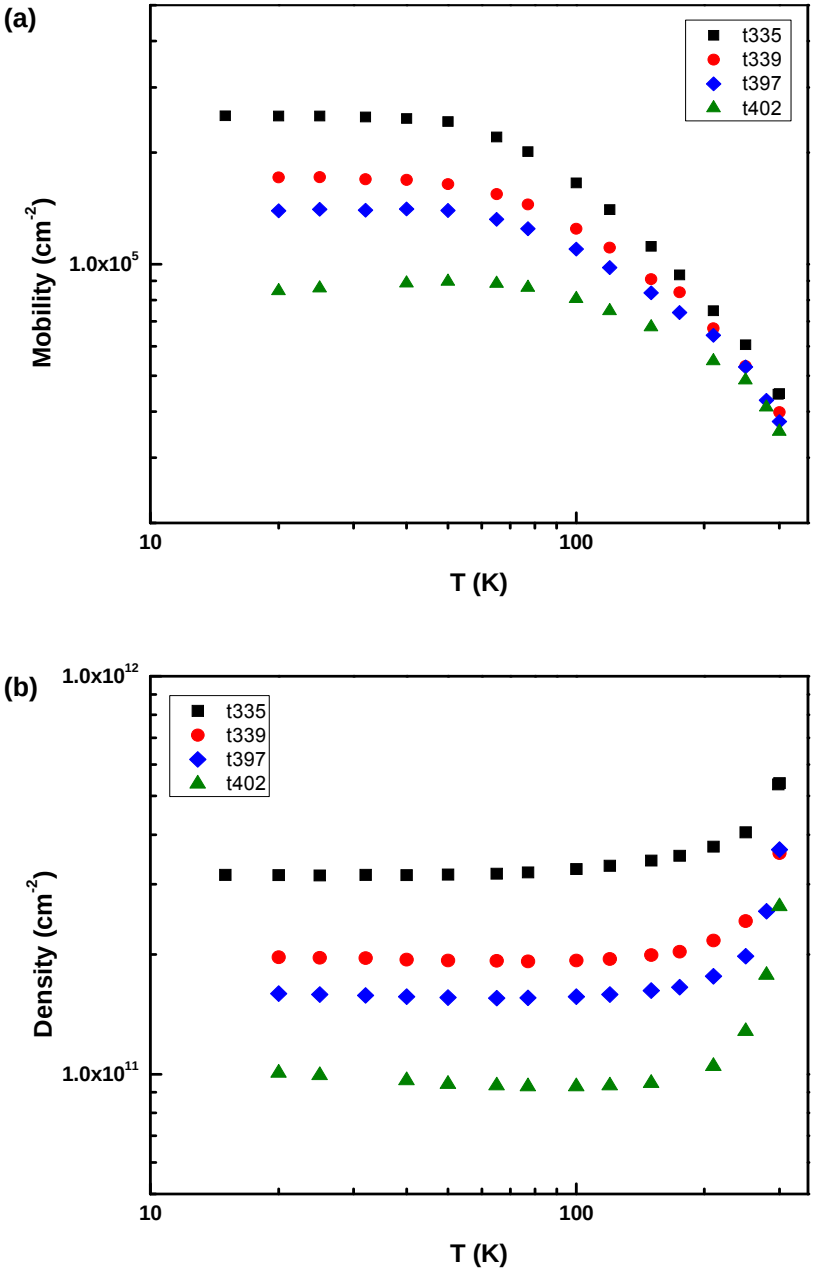

Fig 3.6: The temperature dependence of (a) mobility and (b) density for different doping concentrations in δ-doped layers. δ-doping near the surface was 3.6×10^{11} cm^{-2}(3.0×10^{11} cm^{-2}) for the structures t335 and t337 (for t397 and t402).

3.1.5 Electron mobility and density in symmetrically doped InSb QWs

In symmetrically doped InSb QWs, δ-doped layers with equal doping densities are placed on both sides of the well with an equal spacer layer thickness of *d* from the well. Therefore electrons in the well feel a zero net electric field and the field in one side of the spacer is now half as much as given by equation 3.3. The density is now accordingly higher than given by equation 3.5. A QW structure designed in the previous section with well thickness of 20nm, *d*=15nm, and x=0.2 in $Al_xIn_{1-x}Sb$ barriers was chosen since this shows better performance. Because of the short distance from surface to well (60nm), these structures can be used for device processing by optical and E-beam lithography. Therefore, symmetrically doped InSb QW structures were used by Dr. Murphy's group at OU to fabricate nano-wires by E-beam lithography to study the spin relaxation via anti-weak localization [20]. QWs with low temperature densities of $3\text{-}5\times10^{11}cm^{-2}$ with no parallel conduction and low mobility (~50,000cm^2/Vs) were required for this study in order for the spin relaxation theory to be applied.

Since high mobility is not required a series of symmetrically doped InSb QWs with $Al_{0.20}In_{0.80}Sb$ barrier layers were grown with a buffer layer of constant composition instead of several interlayers. The typical layer structure is shown in Fig. 3.7. A single relaxed 1.8μm thick $Al_{0.20}In_{0.80}Sb$ buffer layer was grown on semi-insulating GaAs(001) (2° off [001] toward [110]) substrate. A 0.25μm thick $Al_{0.10}In_{0.90}Sb$ layer was grown prior to the QW growth to observe the transition from pseudo (1×3) to c(4×4). A Si δ-doped layer near the well (the surface) provide the carriers to the well

(surface states). A summary of a series of symmetrically doped InSb QWs along with the doping density is given in Appendix A Table A.2.

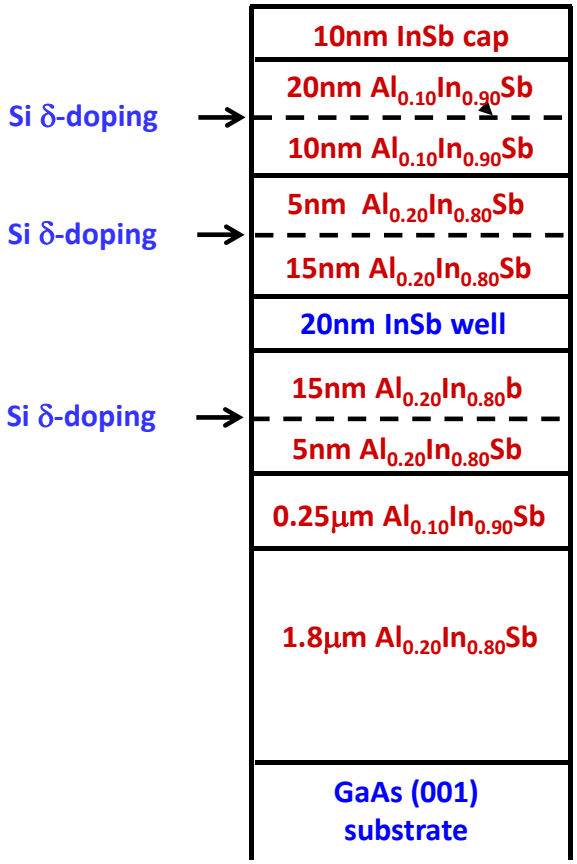

Figure 3.7: The layer structure of a symmetrically-doped InSb QW with $Al_{0.20}In_{0.80}Sb$ barriers. Two δ-doped layers are placed 15nm from the well.

The effect of the δ-doping concentration on carrier mobility and density in symmetrically doped QWs was studied. The mobility and density obtained for a few symmetrically doped QWs along with the doping densities are listed in Table 3.2. Since

the electrons in the well experience a zero net electric field, the peak of the electron probability density will remain in the middle of the well. Therefore both ionized dopant scattering and interface roughness scattering have less effect on mobility in symmetrically doped QWs compared to the asymmetrically doped QWs. Mobility both at 300K and 20K in these QWs was lower than that of in asymmetrically doped QWs because of the relatively thin non-interlayer buffer (~2μm). The mobility at low temperature in these QWs is limited mainly by the defects due to the lattice mismatch between the buffer layer and the substrate. However the electron densities in symmetrically doped QWs are slightly higher than in asymmetrically doped QWs which is expected for the similar net doping densities.

An observed electron density of 3.8×10^{11} cm^{-2} for the structure t340 with two delta doped layers of net $N_d \sim 3.6\times10^{11}$ $cm^{-2}$is slightly higher than that of 3.1×10^{11} cm^{-2} for the structure t335 with a single delta doped layer with the same doping density. A decrease in the carrier density with decreasing δ-doping density near the well was observed for these structures. The structure with the lowest doping density near the well (N_D~1.1×10^{11} cm^{-2} in each side) showed the highest mobility: μ = 78,300 cm^2/Vs with n = 3.0×10^{11} cm^{-2} at 20K and μ = 36,700 cm^2/Vs with n = 3.7×10^{11} cm^{-2} at room temperature.

Sample	δ-doping ($\times 10^{11}$ cm^{-2})		Average density (cm^{-2})		Average mobility (cm^2/Vs)	
	surface	well	20K	300K	20K	300K
t337	3.6	1.8	3.8	5.4	51,780	27,260
t340	3.6	1.3	3.6	4.9	56,360	29,000
t348	3.0	1.1	3.0	3.7	78,280	36,700

Table 3.2: The Hall mobility and density observed for a few symmetrically doped InSb QWs with 15nm spacer layer and 20nm $Al_{0.20}In_{0.80}Sb$ barrier layers are listed.

3.2 High mobility $In_yGa_{1-y}As/In_xAl_{1-x}As$ QW structures

InGaAs/InAlAs high electron mobility transistors (HEMTs) have long been studied for potential in millimeter wave applications and optical communications because of their excellent high frequency and low noise performances [21, 22]. $In_yGa_{1-y}As$/ $In_xAl_{1-x}As$ QWs are grown metamorphically ($0.3 \leq y \leq 0.7$) on GaAs substrates with graded buffer layers (mHEMTs) or pseudomophically ($0.53 \leq y \leq 0.7$) on InP substrates with lattice matched $In_{0.52}Al_{0.48}As$ barriers (pHEMTs). $In_yGa_{1-y}As$ QWs ($0.15 \leq y \leq 0.3$) are also grown pseudomorphically with wide band gap AlGaAs barriers on GaAs substrates, which make pHEMT suitable for high power applications [23]. It was found recently that $In_yGa_{1-y}As$ based QWFETs are suitable for logic applications with better performance than Si transistors as they can be operated at low supply voltage down to 0.5V [24]. High In content $In_{0.7}Ga_{0.3}As$ channel QWFETs have already been

demonstrated with excellent performance with gate lengths down to 50nm and operating at a supply voltage of 0.5V [25, 26].

The smaller effective mass for electrons ($0.045m_e$) in $In_{0.53}Ga_{0.48}As$ which leads to higher mobility and high saturation velocity, arises from the large energy difference between Γ and L valley (~0.55eV [27]), and makes this material attractive as the channel material. Since $In_{0.53}Ga_{0.47}As$ and $In_{0.52}Al_{0.48}As$ are lattice matched to InP substrates, a high quality 2DEG can easily be fabricated with the electron mobility in $In_{0.53}Ga_{0.47}As$ closer to the intrinsic values which is half way between GaAs and InAs. Electron mobility in $In_yGa_{1-y}As/In_xAl_{1-x}As$ QWs can be further increased with even higher densities by introducing strain into the well by slightly increasing the indium content (y>0.53) in the channel. Strain can be introduced into the barriers by slightly increasing the Al composition beyond the value needed for lattice matching (x<0.52) in $In_xAl_{1-x}As$ barrier layers. Larger barrier height due to the strain and the increased band gap in $In_xA_{1-x}lAs$ barriers enables higher densities without populating the 2nd sub band.

Therefore growth of high mobility $In_yGa_{1-y}As/In_xAl_{1-x}As$ QWs was motivated by their potential for electronic device applications. Growth of strained-well (y=0.64, x=0.52) and strained-well-and-barrier (y=0.64, x=0.45) remotely doped pseudomorphic $In_yGa_{1-y}As/In_xAl_{1-x}As$ QWs along with their mobility and density is described in this section. Since the compressive strain in the $In_{0.64}Ga_{0.36}As$ well is balanced by the tensile strain in the $In_{0.45}Al_{0.55}As$ barriers, the whole structure is dislocation free and therefore referred as a strain balanced structure. These QW structures in general exhibit higher densities. An attempt was also made to grow lattice matched InGaAs/InAlAs QW

structures with modulation doping by increasing the spacer layer thickness in order to obtain lower density (2-3×$10^{11}$$cm^{-2}$).

3.2.1 The layer structures of remotely doped $In_yGa_{1-y}As/In_xAl_{1-x}As$ QWs.

Remotely doped $In_yGa_{1-y}As/In_xAl_{1-x}As$ structures were grown on semi-insulating, on-axis, quarter of a 2□ InP (001) substrates at or slightly above the oxide desorption temperature for InP. The growth rate of strained (y=0.64) and lattice matched (y=0.53) $In_yGa_{1-y}As$ channels was kept at ~0.53ML/s and ~0.63ML/s, respectively. The growth rate of the strained (x=0.45) and lattice matched (x=0.52) $In_xAl_{1-x}As$ barrier layer was kept at ~0.73ML/s and ~0.64ML/s respectively in these structures. A 15-20 times higher As_2 flux than the group III fluxes was used during the growth of all the structures.

The typical layer structure for strained and strain balanced, modulation doped, pseudomorphic $In_{0.64}Ga_{0.36}As/In_xAl_{1-x}As$ QWs is shown in Fig. 3.8(a). Since the InP substrates are nearly lattice matched to the $In_yGa_{1-y}As/In_xAl_{1-x}As$ QW structure, a 100nm thick $In_{0.52}Al_{0.48}As$ buffer layer which is lattice matched to InP was grown prior to the QW as shown in Fig. 3.8(a). A 10nm thick $In_{0.64}Ga_{0.36}As$ QW layer was sandwiched between $In_xAl_{1-x}As$ (x=0.52, 0.45) barrier layers to obtain quantum confinement. A higher In percentage in the strained well with the strained $In_{0.45}Al_{0.55}As$ barriers is expected to increase the mobility and the carrier confinement in this structure, respectively. A single Si δ-doped layer was placed in the upper $In_xAl_{1-x}As$ barrier a distance d (10nm, 18nm) above the well to provide the electrons to the well. A

second Si δ-doped layer placed in the $In_{0.52}Al_{0.48}As$ layer near the surface provides the electrons to the surface states. A 10nm $In_{0.53}Ga_{0.47}As$ cap layer was grown on the top to prevent the oxidation of the $In_{0.52}Al_{0.48}As$ layer.

In lattice matched $In_{0.53}Ga_{0.47}As/In_{0.52}Al_{0.48}As$ QWs, a 300nm $In_{0.52}Al_{0.48}As$ buffer layer was grown prior to the 20nm $In_{0.53}Ga_{0.47}As$ QW as shown in Fig. 3.8(b). A lower carrier density can be achieved by lowering the doping concentrations or by increasing the spacer layer thickness. Therefore a Si δ-doped layer, which provides the electrons to the well was placed a spacer thickness of 50nm above the QW. The second Si δ-doped layer which provides the electrons to the surface states was placed a distance 140nm away from the first δ-doped layer. A 20nm thick $In_{0.53}Ga_{0.47}As$ cap layer was grown on the top.

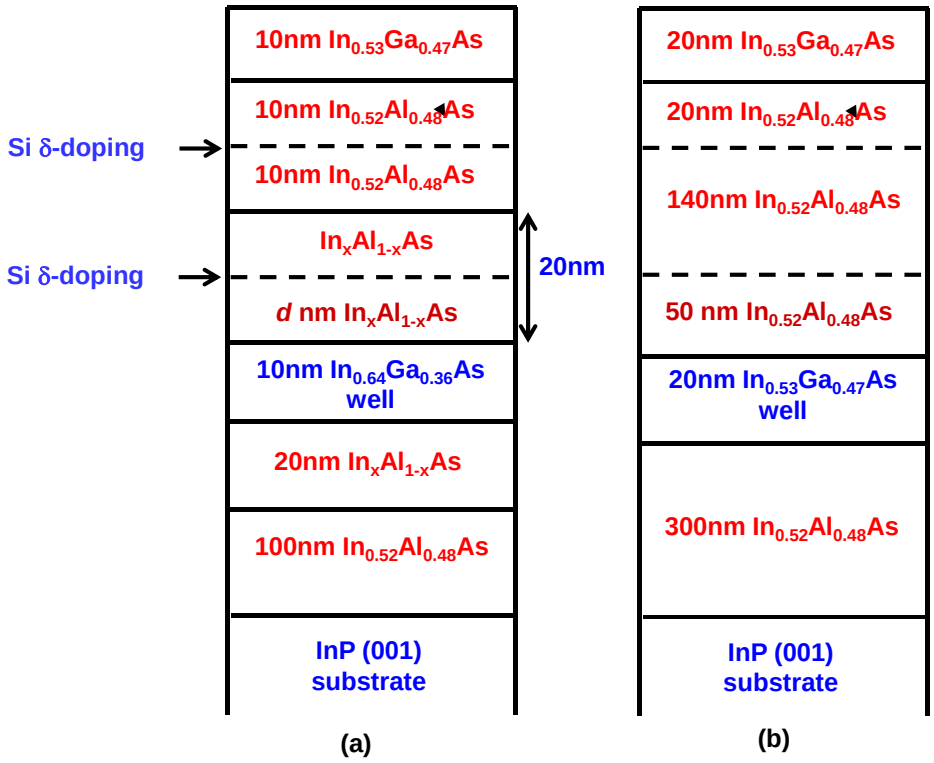

Figure 3.8: The layer structure of (a) strained /strain balanced $In_{0.64}Ga_{0.36}As$ QW and (b) lattice matched $In_{0.53}Ga_{0.47}As/In_{0.52}Al_{0.48}As$ QWs. The strain balanced (strained) QWs are realized with $In_{0.45}Al_{0.55}As$ ($In_{0.52}Al_{0.48}As$) barriers in structure (a).

3.2.2 Mobility and density results and discussion.

The dependence of the 2D electron properties on growth temperature and spacer layer thickness in high In content $In_{0.64}Ga_{0.36}$ QWs is discussed. The Hall measurement was performed on ~8mm square pieces in magnetic fields up to 0.12T over the temperature range from 300K to 25K in a closed cycle He refrigerator (Sec. 2.2). Electrical contacts are made by annealing In at 380°C-400°C in a H_2 (20%) and N_2 (80%) environment for 7-10min. Table 3.3 shows the mobility and density data obtained for the

$In_{0.64}Ga_{0.36}As/In_xAl_{1-x}As$ QWs along with the channel growth temperature and the spacer layer thickness.

sample	x	d (nm)	mobility (cm^2/Vs)		density ($\times 10^{12} cm^{-2}$)		T_{sub} (°C)
			300K	25K	300K	25K	
P103	0.45	10	6,500	11,380	1.22	1.05	420
P110-c	0.52	10	1,300	730 (32K)	0.57	0.47 (32K)	460
P122	0.45	18	11,680	53,790	1.10	1.05	505
P123	0.45	10	10,800	40,830	1.25	1.20	505

Table 3.3: The average mobility and density for strained (x=0.52) and strain balanced (x=0.45) $In_{0.64}Ga_{0.36}As/In_xAl_{1-x}As$ QWs along with the growth temperature.

Both strained and strained balanced $In_{0.64}Ga_{0.36}As$ QW structures grown at low temperature (<480°C) showed poor electrical properties. Low temperature growth can result in the incorporation of background impurities into the growing film and degrade their electrical properties. Strained balanced $In_{0.64}Ga_{0.36}As/In_{0.45}Al_{0.55}As$ QW structures grown at higher temperatures on the other hand have shown better transport properties at all temperatures.

The highest mobility and density were observed for the structures grown at higher substrate temperature (505°C) with an 18nm spacer layer in comparison to the structure with a 10nm spacer. A room temperature (low temperature) mobility of

11,680cm^2/Vs (53,790cm^2/Vs) and density of 1.1×10^{12}cm^{-2} (1.0×10^{12}cm^{-2}) was observed for the structure with an 18nm spacer, due to the reduced ionized dopant scattering.

All lattice matched $In_{0.53}Ga_{0.47}As/In_{0.52}Al_{0.48}As$ QWs had a 50nm spacer layer thickness and were grown at a fixed substrate temperature of 500°C with different doping densities. The electron mobility and density obtained for a few low-doping lattice matched InGaAs/InAlAs QWs are listed in Table 3.4.

sample	δ-doping ($\times10^{11}$ cm^{-2})		mobility (cm^2/Vs)			density ($\times10^{11}$cm^{-2})		
	well	surface	300K	77K	20K	300K	77K	20K
P219	5.7	20.5	7,400	13,200	12,900	12.1	8.5	8.0
P231	4.1	13.8	9,370	27,800	17,500	3.3	3.8	2.0
P234	4.6	13.8	9,200	29,600 (65K)	26,900	3.8	2.8 (65K)	2.8

Table 3.4: The average mobility and density for lattice matched $In_{0.53}Ga_{0.47}As/In_{0.52}Al_{0.48}As$ QWs along with the doping density for the well and surface are listed.

Mobilities of lattice matched structures were lower than those of the strain balanced InGaAs QW structures at all temperatures. The highest mobility of 9,400 cm^2/Vs was observed in structure P231 with the density of 3.3×10^{11}cm^{-2} at 300K. The highest low temperature mobility of 29,600 cm^2/Vs was observed in structure P234

with a density of $2.8\times10^{11}cm^{-2}$ at 77K. The temperature dependent mobility and density are shown in Fig. 3.9. Degradation in the mobility has been observed in these QW structures for temperatures below ~77K. Achieving higher mobility with lower carrier density ($2\text{-}3\times10^{11}cm^{-2}$) was challenging due to the large spacer layer thickness and/or due to the lower doping density.

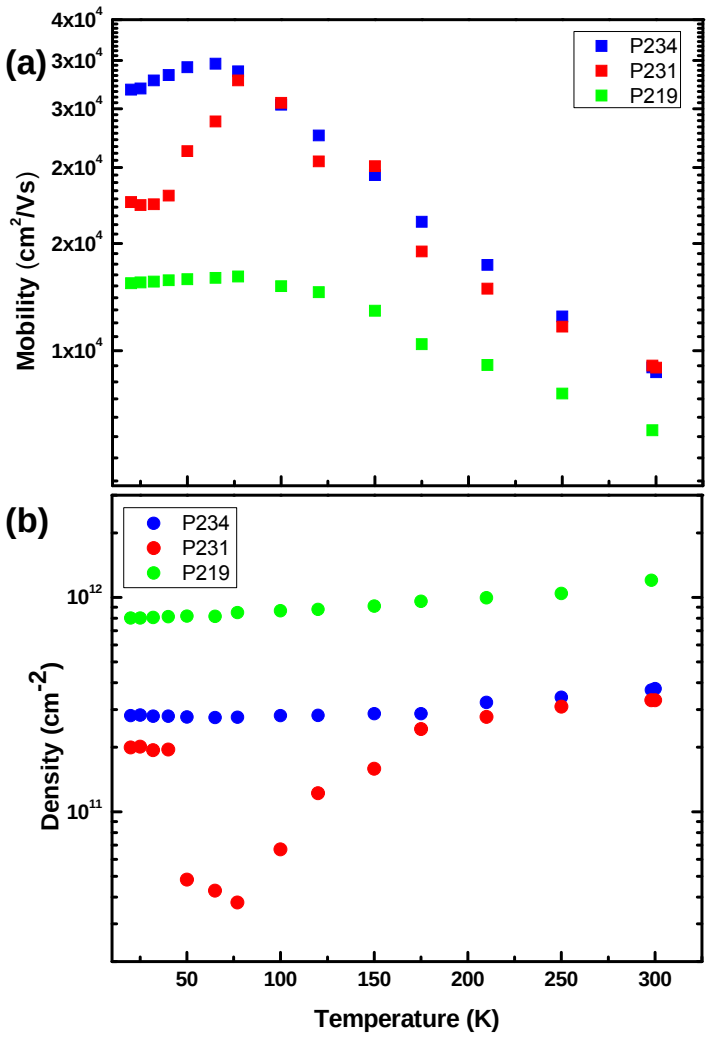

Figure 3.9: (a) Electron mobility and (b) density of a few low-doping lattice matched $In_{0.53}Ga_{0.47}As/In_{0.52}Al_{0.48}As$ QWs grown on InP(001) substrates.

3.3 High mobility $In_yGa_{1-y}As$ QWs for high-κ dielectric based MOSFETs

The advantage of having high mobility $In_{0.53}Ga_{0.47}As$ as a channel material over GaAs and Si in MOSFET technology has long been recognized [28, 29]. As Si-MOSFET scaling has reached the fundamental limit, attention has focused on alternative high mobility, smaller band gap III-V channel materials such as InSb and $In_yGa_{1-y}As$ and alternative high dielectric constant (high-κ) materials such as HfO_2 instead of SiO_2 for Si-MOSFETs. A high density of interfacial states due to the absence of an ideal native oxide, unlike SiO_2, for Si has been the key issue in III-Vs being used as the channel in MOSFETs. High quality and good thermal stability of the gate dielectric are necessary to passivate the interface states and prevent Fermi level pinning at the III-V/gate dielectric interface [30]. Much research has been devoted towards realizing a high quality thermodynamically stable insulator/III-V channel interface. Ga_2O_3 [31] and Al_2O_3 [32] dielectrics and passivation techniques using Si [33] or Ge [34] interface passivation layers (IPLs) on GaAs or low In content $In_{0.2}GA_{0.8}As$ have been studied. However, only a few studies have been done on small band gap channel materials such as InSb, InAs and high In content $In_yGa_{1-y}As$ with high-κ dielectrics such as HfO_2 for MOSFET applications.

In order to address this issue $In_yGa_{1-y}As$ channel MOSFETs were investigated using high-κ dielectrics and different passivation techniques by Intel Corp. First standard $In_{0.53}Ga_{0.47}As/In_{0.52}Al_{0.48}As$ structures on InP substrates were grown, in order to estimate the mobility and concentration baselines for comparison with the improved structures. These transistor layer structures were provided to Intel and their

collaborators to deposit dielectric layers and fabricate MOSFETs. Feedback from the results of the device performance was used to develop improved structures with high In content. Increasing *x* beyond 0.53 is expected to enhance electron-transport properties, which translate to higher cutoff frequency and higher gain. A brief summary of the layer structures grown for MOSFETs, evolution of dielectric integration and the results of the HfO_2 based $In_{0.53}Ga_{0.47}Aa$ channel MOSFETs are given in this section.

3.3.1 Layer structure growth and characterization

Undoped, *n*-doped, and *p*-doped $In_{0.53}Ga_{0.47}As$ and $In_{0.52}Al_{0.48}As$ layers were grown by MBE on 2″ on-axis semi-insulating (SI) and doped (*n*, *p* - type) InP(001) substrates respectively. Undoped $In_{0.53}Ga_{0.47}As$/ $In_{0.52}Al_{0.48}As$ epilayers grown on SI InP substrates were used for MOS capacitor fabrication whereas doped $In_{0.53}Ga_{0.47}As$ channels and $In_{0.52}Al_{0.48}As$ buffer layers grown on doped InP substrates were used for MOSFET fabrication. Figure 3.10 shows different layer structures grown for MOS capacitors and MOSFET fabrications. Si (Be) was used as the *n*-type (*p*-type) dopant. $In_{0.53}Ga_{0.47}As$ and $In_{0.52}Al_{0.48}As$ layers were grown at a rate of ~0.63ML/s and a V/III ratio of 15:1 was maintained. Growth temperatures of 480°C and 500°C were used for the growth on doped SI substrates.

An amorphous arsenic (As) cap layer was grown on some of the InGaAs structures shown in Fig. 3.10(a) that were used to study *ex-situ* dielectric depositions such as $LaAlO_3$ [35] and Al_2O_3. An As cap layer prevents the formation of a native oxide and contamination during air transfer and minimizes interfacial defect density

[36]. The substrate heater was turned off after growth of the layer structure and the wafer was cooled down overnight inside the growth chamber prior to the As deposition. An arsenic cap layer was deposited by exposing the wafer to an As_2 flux of 1×10^{-5} Torr for 3 (~300nm) to 1 (100nm) hours while being rotated very slowly for uniform deposition. The substrate temperature was increased to ~10°C during the As deposition by heating from the hot arsenic cell. Calibrations of doping and In compositions were performed on 300nm-500nm thick uniformly doped $In_{0.53}Ga_{0.47}As$ epilayers grown on SI InP(001) substrates by using Hall effect and HRXRD measurements (Chap. 2), respectively.

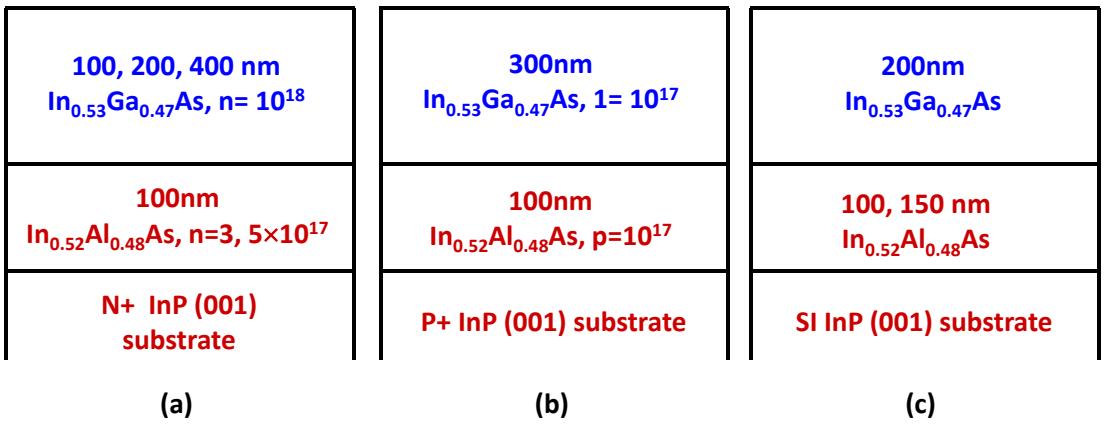

Figure 3.10: Schematic of doped $In_{0.53}Ga_{0.47}As/In_{0.52}Al_{0.48}As$ layer structures for (a) *n*-channel and (b) *p*-channel MOS capacitors and (c) un-doped $In_{0.53}InGa_{0.47}As/In_{0.52}Al_{0.48}As$ layers for MOSFET fabrication.

3.3.2 Results and discussion (from papers)

MOS capacitors (MOSCAPs) were fabricated with HfO_2 dielectric layers deposited by physical vapor deposition (PVD) on the 100nm thick doped (n=1×10^{18}cm^{-3}) $In_{0.53}Ga_{0.47}As$ channel structures shown in Fig. 3.10(a). These have been used to study the effect of post-deposition anneal (PDA) time on material and electrical characteristics of MOSCAPs with high-κ HfO_2 [37]. It was found that compared to GaAs, high-κ dielectrics on high In content $In_{0.53}Ga_{0.48}As$ channel MOSCAPs exhibit much higher quality interfaces with reduced Ga-O and As-O bonds after PDA and excellent capacitance voltage (C-V) characteristics with a thin equivalent oxide thickness (EOT) of ~1.1nm [37].

The frequency dispersion of parasitic capacitance has been another issue for high-κ dielectrics on III-V channels since it is correlates with the interface density [38]. MOSCAPs fabricated on the structures shown in Fig. 3.10(a) with HfO_2 and a Si interface passivation layer (IPL) deposited by PVD showed very low frequency dispersions (<1%), indicating a better interface quality with low interface trap density in comparison to those without a Si IPL at different PDA conditions [38, 39]. *n*-MOSFETs fabricated on the 200nm $In_{0.53}Ga_{0.47}As$ structures shown in Fig. 3.10(c) using the ring-FET transistor pattern and the same gate stack (HfO_2 and Si IPL) deposited by PVD [38] and dc sputtering [40] also showed improved device performances. Studies on effects of PDA temperatures and Si IPL thickness on *n*-$In_{0.53}Ga_{0.47}As$ channel MOSFETs showed that the annealing temperatures are critical for determining the transistor performance [39].

MOSFETs and MOSCAPs were fabricated on 200nm and 400nm $In_{0.53}Ga_{0.47}As$ structures with HfO_2 and thin Ge IPLs [41]. Among these, MOSCAPs have demonstrated low frequency dispersions and low leakage current with Ge IPL. The *n*- and *p*-type MOSCAPs fabricated with HfO_2 and a Ge IPL on the structures shown in Fig. 3.10(a) and (b) were studied with different PDA conditions and compared with *n*- and *p*-type InAs, GaAs and InSb MOSCAPs [42]. All *n*-type MOSCAPs with HfO_2 and a Ge IPL showed good C-V characteristics with low frequency dispersion (<10%) compared to those without a Ge IPL. However, MOSCAPs on *p*-type GaAs and $In_{0.53}Ga_{0.47}As$ exhibited poor C-V characteristics while *p*-type InAs and InSb exhibited good C-V characteristics. It was found that the poor C-V characteristics of *p*-MOSCAPs based on HfO_2 and Ge IPL were due to strong Fermi level pinning and it became worse with Ge passivation.

Chapter 4

2D Hole Systems in InSb and $In_yGa_{1-y}As$ Quantum Well Structures

4.0 Introduction

Complementary Metal Oxide Semiconductor (CMOS) technology is the most desirable technology for modern digital logic applications because of the lower static power consumption and high performances [1]. CMOS circuits require *p*-channel transistors with high hole mobility, in addition to *n*-channel transistors with high electron mobility. The Si/SiO_2 material system has long dominated the CMOS technology due to the advantages of nearly matching electron and hole mobilities and well established fabrication procedures. The performance of III-V based field effect transistors (FETs) for the CMOS configuration are lagging behind, mainly due to low hole mobilities and a lack of suitable gate insulators.

Because the narrower band gap leads to a smaller effective mass for the electrons and holes in III-V materials, higher mobilities are expected in these materials if the mean scattering time is similar. III-V quantum well (QW) materials with high electron mobilities, including InSb and $In_yGa_{1-y}As$, however, exhibit relatively low hole mobilities, presumably due to a larger effective mass for holes. Heavy-hole (HH) and light-hole (LH) valence bands are degenerate at the Γ point in a bulk III-V semiconductor. In a QW, the degeneracy can be lifted by the strain and the confinement in a way that increases the hole mobility. Biaxial compressive strain is introduced into

an InSb QW with an intentional lattice mismatch between the InSb well and $Al_xIn_{1-x}Sb$ buffer/barrier layer in a controlled way by choosing the appropriate Al composition (x). Biaxial compressive strain is introduced into an $In_yGa_{1-y}As$ QWs by slightly varying the indium composition (y>0.53) in the channel. A study of the dependence of hole mobility on structural parameters is described in this chapter, with the goal of achieving high hole mobility in InSb and $In_yGa_{1-y}As$ QWs.

The chapter is organized as follows. First, an experimental study of the effective mass of holes in InSb QWs with different strain, confinement and carrier densities is reported. The smallest hole effective mass of $0.017m_e$ is observed in our InSb QW with a 1.05% compressive strain [2]. The hole mobility in the strain engineered QW can be further increased through improvement in crystal quality with minimal defects and other irregularities, via better buffer layer design. Next, the effect of the buffer layer structure on hole mobility in *p*-InSb QWs will be discussed. 2D hole systems in $In_yGa_{1-y}As$ QWs were realized by remotely doping the $In_xAl_{1-x}As$ barriers with Be. The mobilities and densities are reported at the end of the chapter.

4.1 Effect of strain and confinement on the valence band of III-V QWs

The valence band structure in a bulk III-V semiconductor consists of a highly non-parabolic heavy-hole (HH) band, a light-hole (LH) band and a split-off band which is shifted far away in energy [3]. The HH band and the LH hole band are degenerate at the center of the Brillouin zone, and both bands are occupied resulting a lower hole mobility. The strain and confinement in a QW lifts the degeneracy in an interesting

way. In the (001) growth direction, the HH (LH) band has a heavier (lighter) effective mass. In other words, the "heavy" and "light" names correspond to the mass in the growth direction.

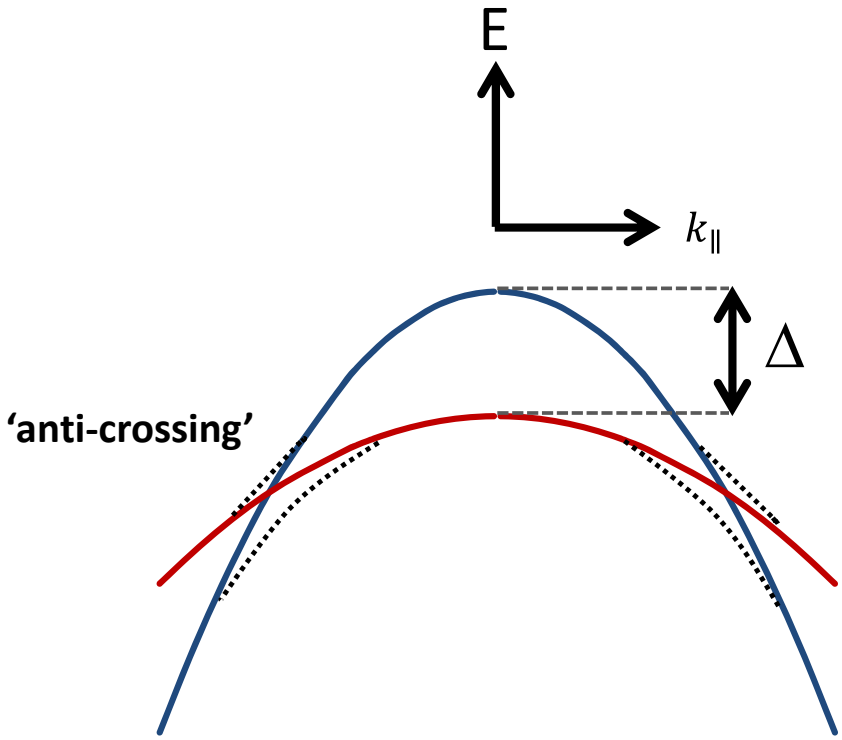

Figure 4.1: Schematic diagram of the relevant hole sub-bands for a III-V QW. The hole energy is plotted versus the hole wave vector for in-plane motion. The upper (HH) and lower (LH) curves describe holes that are light and heavy, respectively for in-plane motion. Expected anti-crossings are shown in dash lines.

The quantum confinement induced by the narrow channel width will lift the degeneracy as shown schematically in Figure 4.1. Because the higher-energy band (HH) has a lighter hole mass in the plane of the QW while the lower-energy band (LH) has a heavy hole mass in the plane of the QW, the hole mobility can be significantly

enhanced by confinement if only the higher energy band is occupied in a QW channel since the in-plane mass of the higher band is lighter.

Biaxial strain breaks the cubic symmetry of III-V semiconductors and alters the band structure. Biaxial compressive strain splits HH and LH bands such that the effective mass of the higher energy band (HH) in Figure 4.1 is lighter in the in-plane direction and heavier in the growth direction similar to effect of the confinement. Therefore in order to maximize the hole mobility, both biaxial compressive strain and confinement should be maximized to induce a large energy separation between the maxima for the two bands Δ [Figure 4.1]. However, the "anti-crossings" of the two bands can add significantly to their non-parabolicity, resulting in mixing of the heavy and light characters when close to the anti-crossing points as shown in Figure 4.1. Therefore, anti-crossings of the bands significantly affects the hole mobility as the Fermi level gets close to the anti-crossing points.

4.2 Effect of Strain, confinement and density on effective mass of Holes in InSb QWs

Because the energy separation of the maxima for the two bands Δ (Figure 4.1) increases with increasing biaxial compressive strain and decreasing well width as described in section 4.1, one can conclude that the effective mass at the Fermi level will depend on strain, well width, and hole density. The effective mass of holes in strained InSb QW structures was studied and the results are discussed in this section.

4.2.1 Layer structures

The five QW structures in this study were grown on semi-insulating 2° off, GaAs (001) substrates by molecular beam epitaxy [4]. The layer sequences are shown in Figure 4.2. For the sequences shown in Figure 4.2 (a) and 4.2 (b), the Be δ-doped layer near the surface provides holes to surface states, while the other δ-doped layer supplies holes to the nearby InSb QW. For the sequence shown in Figure 4.2 (c), a single δ-doped layer supplies holes to both the surface states and the QW. A two-dimensional hole system is confined within the InSb QW (7, 9, or 15 nm thick) by $Al_{0.20}In_{0.80}Sb$ barrier layers. The InSb QW is compressively strained to the lattice constant of the relaxed 2 μm-thick $Al_xIn_{1-x}Sb$ (x=0.15 or 0.20) buffer layer. Three QW structures (Structures A, B, and C) followed the layer sequence shown in Figure 4.2 (a). These structures had different hole densities in the well due to different doping densities and/or different values for d, the separation between the well and dopant layers. The QWs in these three structures were 15nm thick and compressively strained by 0.8% to the lattice constant of $Al_{0.15}In_{0.85}Sb$. The layer sequence for Structure D is shown in Figure 4.2 (b). The hole density is similar to that in Structure B, but the QW is thinner (9 nm thick) and under more compressive strain (1.05% strain) due to the $Al_{0.20}In_{0.20}Sb$ buffer layer. The layer sequence for Structure E is shown in Figure 4.2 (c). The hole density is similar to that of Structure C, but the QW is thinner (7 nm thick) and under more compressive strain (1.05% strain). The separation between the two hole bands, Δ in Figure 4.1, is due to strain and confinement. Strain alone would make Δ equal to 70 meV and 93 meV for Structures A-C and D-E, respectively [5].

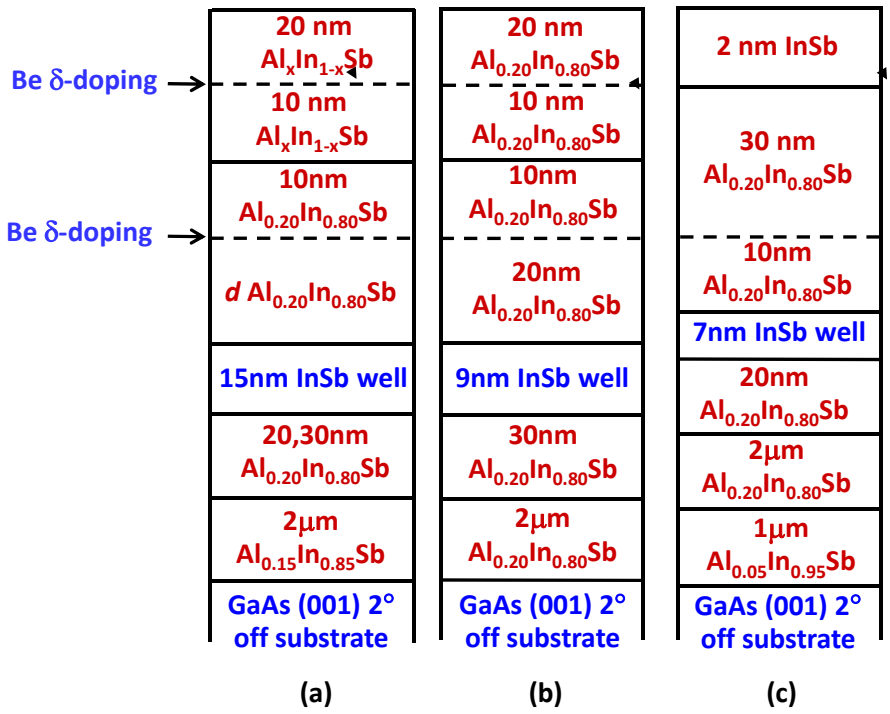

Figure 4.2: The layer sequences for the *p*-type InSb QWs in this study. The dashed lines indicate Be δ-doped layers. Structures A and B are described by (a) with d=20 nm; Structure C is described by (a) with d=10 nm. Structures D and E are described by (b) and (c), respectively.

4.2.2 Measurements

The hole density and the hole mobility for all five structures were deduced from van der Pauw and Hall effect measurements [sec. 2.2]. The measurements were made in a closed-cycle refrigerator at temperatures from 300K to 20K, and the magnetic field was swept between 0 and 0.12T. Electrical contact was made at the corners of square samples (8 mm × 8 mm) by annealing indium-zinc contacts at 230°C for 7 minutes in a 20% H_2:80% N_2 atmosphere. The density and mobility values at 20K and 300K are

listed in Table 4.1, along with the values for QW width and strain. The hole densities in all five structures are low enough that one can expect only the higher energy band of Figure 4.1 to be occupied at low temperature.

Structure	W (nm)	Strain (%)	p (10^{11}cm^{-2}) 20K [300K]	μ_h (cm^2/Vs) 20K [300K]	m* (m_e)
A (t196)	15	0.80	2.1 [12.7]	24,500 [260]	0.046
B (t194)	15	0.80	3.1 [11.1]	26,300 [460]	0.055
C (t198)	15	0.80	5.1 [9.8]	21,500 [570]	0.083
D (t212)	9	1.05	3.5 [7.1]	20,000 [660]	0.062
E (t241)	7	1.05	4.7 [...]	55,600 [...]	0.017

Table 4.1: Structural and electronic parameters of *p*-type InSb QWs at 20K and 300K. *W* is the width of the quantum well. At 300K, Structure E had an electron density of 2.9×10^{11} cm^{-2} and an electron mobility of 11,200 cm^2/Vs.

The effective mass of the holes was deduced from magneto-optical measurements in the Faraday geometry using a Fourier transform infrared spectrometer, with an applied magnetic field up to 3T, and at a temperature of 4.2K. The magnetic field and the propagation direction of the incident photons were perpendicular to the QW plane. A bolometer was placed below the QW structure to measure the intensity of the transmitted infrared light. At low magnetic fields, holes undergo cyclotron orbits with a cyclotron frequency of ω_c=eB/m^*, where m^* is the hole effective mass. A minimum in the transmitted intensity is expected when the frequency of the incident

photons is in resonance with the cyclotron frequency, or equivalently when the photon wavenumber is $K=(e/c)(B/m^*)$ where c is the speed of light. Therefore a value for m^* can be deduced from a measurement of the transmission minimum as a function of B.

4.2.3 Results and Discussion

Figure 4.3 shows cyclotron resonance data for Structures A and E. The transmission spectrum at a constant magnetic field $T(B)$ is normalized by dividing by the zero-field transmission spectrum $T(0)$, and plotted as a function of the photon wavenumber. We observed a well-defined single cyclotron feature in a normalized transmission curve with $1.0\text{T} \leq B \leq 3.5\text{T}$. The low-$B$ limit for observing cyclotron resonance is determined by the requirement that a complete cyclotron orbit is made before a hole is scattered, which requires that $\mu B \geq 1$, or by the spectrometer's beam splitter, which absorbs light with K below ~30 cm^{-1}. Since quantum mechanical effects are stronger at high B (the discrete spin-split Landau levels are well resolved), our semi-classical interpretation would be less valid.

Despite the limited B and K ranges for observing semi-classical cyclotron resonance, enough data were collected to deduce the hole effective mass in all five QW structures. Figure 4.4 shows a plot of the observed cyclotron resonance positions for the five QW structures, as functions of B and K. For each set of points, an effective mass can be deduced from a linear fit that is forced to intersect the origin. The deduced effective mass for each structure is listed in Table 4.1. We will now compare the experimentally deduced values with theoretical expectations.

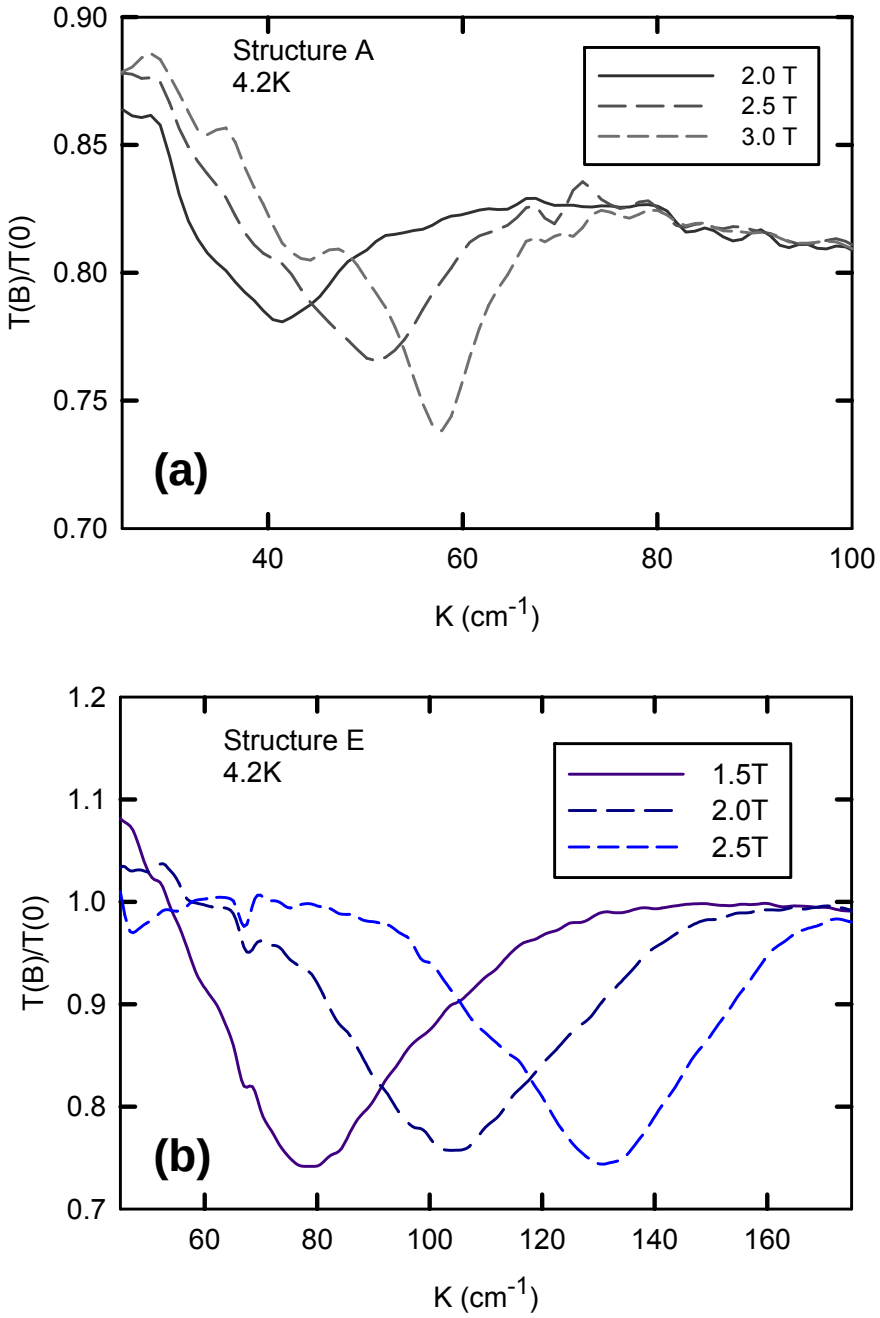

Figure 4.3: Normalized transmission through a *p*-type InSb QW, versus incident photon wavenumber for (a) Structure A and (b) Structure E with an applied magnetic field as indicated.

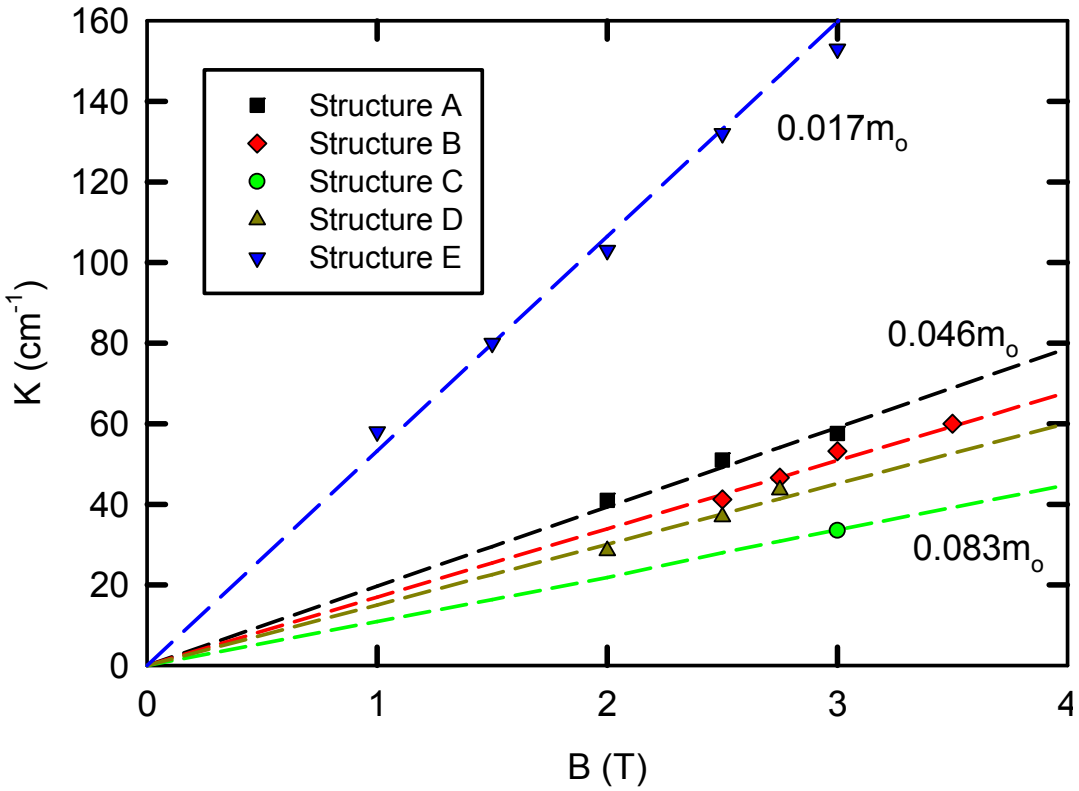

Figure 4.4: Cyclotron resonance wavenumber as a function of applied magnetic field for five QW structures. The effective mass for the holes is between $0.017m_e$ and $0.083m_e$ and depends on the strain and confinement.

The effective mass for the three structures (A, B, and C) with the same well thickness and compressive strain, increased with increasing hole density. This qualitative dependence is expected from Figure 4.1, where the anti-crossings should increase the effective mass of the higher band as the Fermi level approaches the anti-crossing points. Figure 4.5 (a) and (b) show a schematic of the energy band structures for a *p*-type QW with the Fermi level for low and high hole densities, respectively. The

Fermi level is closer to the lower energy band which has higher effective mass for in-plane motion.

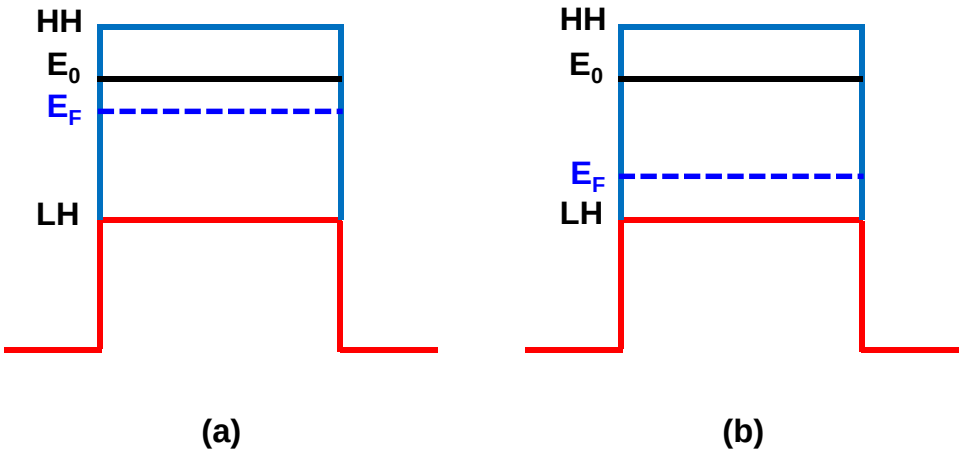

Figure 4.5: Schematic of energy band diagram of a *p*-type InSb QW with (a) low and (b) high hole densities. For low hole densities the Fermi level is closer to the upper energy band (a) which has a light in-plane hole mass, whereas for high hole densities the Fermi level is closer to the lower energy band which has a heavy effective mass for the in-plane motion.

The hole density in Structure D (p=3.5×10^{11}cm^{-2}) is similar to that in Structure B (p=3.1×10^{11}cm^{-2}), but the QW is thinner and under more compressive strain. The measured effective mass in Structure D (0.062m$_e$ where m$_e$ is the mass of an electron in free space) is slightly heavier than in Structure B (0.055m$_e$). This behavior is expected for low hole densities where the dominant effect of increased strain and confinement would be to increase the effective band gap, the energy difference between the ground-state subbands for electrons and holes. One should expect an increase in the band edge

masses for analogous reasons to the increase in carrier masses in III-V materials with increasing band gap. The hole density in Structure E (p=4.7×10^{11}cm^{-2}) is similar to that in Structure C (p=5.1×10^{11}cm^{-2}), but the QW is thinner and under more compressive strain. The measured effective mass in Structure E (0.017m_e) is much lighter than in Structure C (0.083m_e). This behavior is expected for high hole densities where the dominant effect of increased strain and confinement would be to increase the energy where the anti-crossings occur. Moving the anti-crossings further from the Fermi energy reduces their effect on the curvature of the band at Fermi level. This would result in a lighter effective mass.

The Luttinger model is one of the few analytical models that predicts the in-plane hole masses [3, 6]. It does not explicitly account for well width, strain, or the anti-crossings between the two valence bands. According to that model, the masses for the two bands in Figure 4.1 would be $m_e/(\gamma_1+\gamma_2)$=0.019m_e and $m_e/(\gamma_1-\gamma_2)$=0.050m_e where γ_1=36.13 and γ_2=16.24 are empirical parameters determined from bulk InSb measurements [7]. The expected anti-crossings between the two bands should result in a mass for the upper band (Figure 4.1) that varies from 0.019m_e near the bottom of the upper band to 0.050m_e as the bottom of the lower band is approached. Our measured values span a wider mass range (0.017m_e for Structure E to 0.083m_e for Structure C) than predicted by the Luttinger model.

In Reference 8, the effective mass for holes in $In_{0.20}Ga_{0.80}As$ QWs under biaxial compressive strain was measured using cyclotron resonance. An observed m^{*2}~p dependence was explained by a two-band model. The intercept of a plot of m^{*2} versus p yielded a value for the effective mass at the band edge. The m^* values measured in our

cyclotron resonance experiments do not show the *p* dependence predicted by the two-band model.

Radosaljevic *et at*. [9] report the results of an 8-band *k·p* model that explicitly incorporates strain in an InSb QW. The upper limit for the effective mass of the upper band was chosen to be the bulk value for the heavy hole mass ($0.26m_e$) rather than the value from the Luttinger model ($0.050m_e$). It is difficult to make a quantitative comparison between our measured effective masses with the calculation because the well width for the calculation was not disclosed and the number of calculated data points in our density range is small. However, the calculation does correctly predict our observed strain dependence at low density (Structures B and D) and high density (Structures C and E). A rough interpolation of their calculated data points yields a value of ~3-5×$10^{11}$$cm^{-2}$ (~20 meV and ~0.04 m_e) for the crossover between low and high density behavior, in agreement with our observations.

One would expect that a structure with a lower effective mass would have a higher mobility if the mean scattering time is similar for all the structures grown. Indeed, Structure E has both the highest mobility and lowest effective mass at low temperature. However, the effects of scattering, primarily by defects [10] and ionized dopants at low temperatures may not be the same in all the grown layers. This would explain why higher low-temperature mobility does not perfectly correlate with a lower effective mass.

The hole mobility at 300K is much lower than implied by the ratio of the measured effective mass for holes to the electron effective mass (~0.02 m_e). This may be due to the occupation of higher-energy hole subbands (within both the heavy and

light bands), which are expected to have a heavier effective mass than measured at the Fermi level. The average effective mass of the holes in the different subbands at 300K may have a different dependence on strain, confinement, and hole density than does the Fermi-level mass measured at 4.2K. This would explain why Structure D has a higher mobility than Structures A-C at 300K, but not at 20K. More experiments are required to determine why Structure E, which contains less doping than Structures A-D, is *n*-type at 300K.

In summary, our measurements of the effective mass of holes in InSb QWs (0.017 m_e to 0.083 m_e) indicate a strong dependence on hole density, strain, and confinement. A promising candidate to explain our data is an 8-band $k \cdot p$ or Luttinger model that incorporates strain and confinement [9, 11]. The measured effective masses are lighter than previously reported for other III-V QWs at comparable hole density, including GaAs (>0.5m_e [12]), $In_{0.20}Ga_{0.80}As$ (>0.19m_e [8]), and $In_xGa_{1-x}Sb$ (0.1m_e [13]) QWs.

4.3 Hole mobility in compressively strained InSb QWs

InSb is an attractive channel material for *n*-type electronic devices because of the high electron mobility. We have achieved room-temperature electron mobility of 44,700cm^2/Vs for a QW made of InSb as discussed in Chapter 3. A room temperature hole mobility of 700cm^2/Vs was reported by our group for an InSb QW with 1.05% strain and remote doping with Be [4]. The fabrication and performance of *p*-type InSb QW FETs was reported at about the same time by researchers at Intel and QinetiQ [9]. They achieved room temperature hole mobility of 1,230cm^2/Vs for an InSb QW with

1.9% strain. These mobilities are higher than the reported hole mobilities for $In_yGa_{1-y}As$ (260cm^2/Vs [14], 265cm^2/Vs [15], 380, 390, and 400cm^2/Vs [16] with x=0.2, 0.65, 0.73, 0.77, 0.82 respectively). However, these mobilities are still lower than the hole mobilities observed in $In_{0.40}Ga_{0.60}Sb$ QW (1500cm^2/Vs) [13] or in Ge QW (3100cm^2/Vs) [17]. The key concepts behind enhancing the hole mobility in Ge, InSb, or $In_{0.40}Ga_{0.60}Sb$ are the remote doping, quantum confinement and strain engineered QW structure.

The energy splitting Δ between the two bands as shown in Figure 4.1 can be further increased by decreasing the QW thickness (10-5nm) and by increasing the compressive strain in the QW. Simulation studies on strain dependent band structure show that the hole mobility can be further improved up to ~1600cm^2/Vs in InSb QWs by increasing the biaxial compressive strain up to ~2% compared to QWs made of GaAs or GaSb [18]. Theoretical calculations have shown that biaxially compressively strained InSb can provide the highest hole mobility at room temperature with a SiO_2 gate insulator compared to Ge, GaSb or $In_{0.70}Ga_{0.30}As$ with same hole density, but $In_{0.70}Ga_{0.30}As$ also exhibits a promising mobility enhancement [19].

4.4 Improved 2D hole systems in InSb QWs

Structure E, which contains a single doping layer and a metamorphic $Al_{0.20}In_{10.80}Sb$ buffer layer with an $Al_{0.05}In_{0.90}Sb$ initial layer, had the smallest effective mass and the highest hole mobility at low temperature. Compared to Structures A-D with double delta doped layers, having a single doping layer in structure E may be advantageous in

avoiding parallel conducting paths. However, Structure E showed *n*-type conductance at room temperature. A series of compressively strained InSb QWs with a single Be delta doping layer, and $Al_xIn_{1-x}Sb$ buffer layers (x= 0.2-0.25) were investigated with an initial buffer layer with different Al compositions and thicknesses, to investigate the cause. All the *p*-type InSb QWs grown on GaAs(001) substrates are listed in Appendix B. A study of the effect of interlayers and the Al composition of the interlayers on defect reduction in *n*-type InSb QWs, have previously been done by our group [20]. It has been observed that the interlayers with 15% difference in the Al composition had 59% lower TD density compared to the non-interlayer structure and hence improve the low temperature electron mobility [20]. The effect of the initial buffer layer composition, and the thickness on hole mobility and density in *p*-type InSb QWs was also studied and are described in this section.

4.4.1 Layer structures of strained *p*-type InSb QWs

The layer structures were grown on semi insulating GaAs(001) 2° off substrates by MBE. The layer sequences are shown in Figure 4.6. For all the structures, a single Be δ-doped layer provides holes to both the surface states and the QW. A two dimensional (2D) hole system is confined within the InSb QW (6 or 7nm thick) by $Al_{0.20}In_{0.80}Sb$ (in structure F) or $Al_{0.25}In_{0.75}Sb$ (in structures G-M) barrier layers. The InSb QW is compressively strained to the lattice constant of the relaxed 1.5-1.8μm thick $Al_yIn_{1-y}Sb$ (y=0.20 or 0.25) buffer layer. An initial buffer layer of $Al_xIn_{1-x}Sb$ (x=0.07,

0.09, 0.10 or 0.15) was grown prior to the thick relaxed buffer layer and the QW structure. The thickness of the initial buffer layer is varied between 0 and 0.88μm.

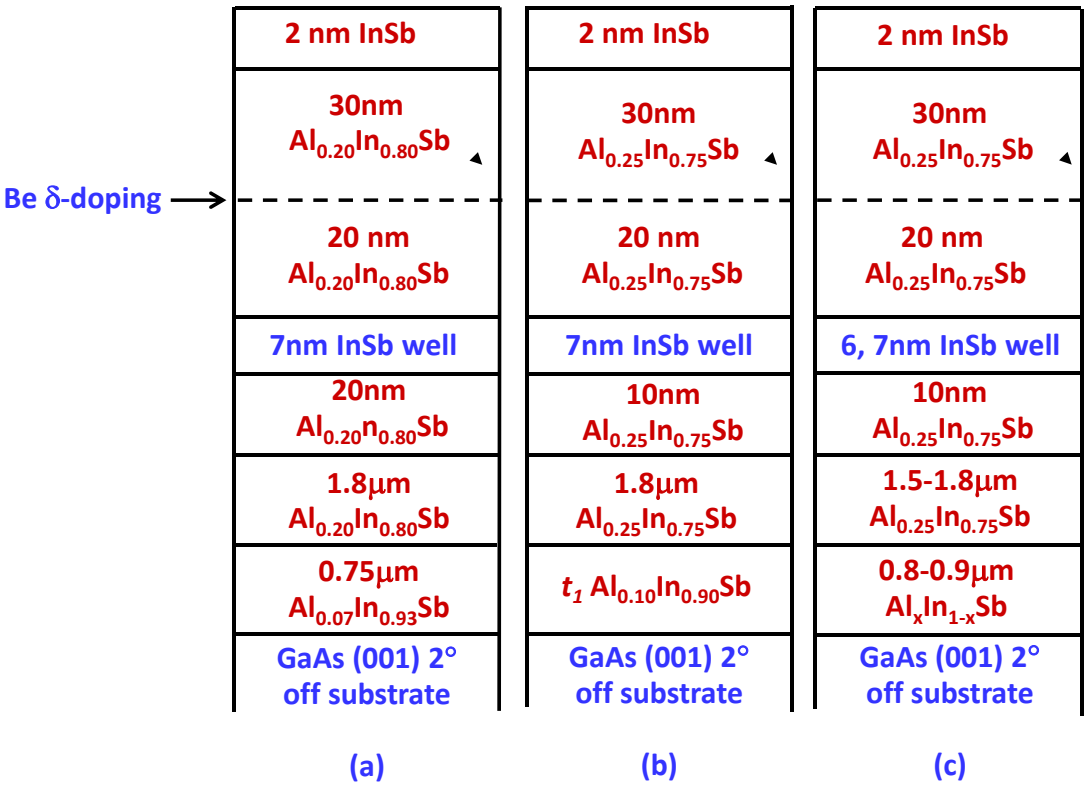

Figure 4.6: The layer structures for the *p*-type InSb QWs. Structure F is described by (a). Structures G, H, I, and J are described by (b) with t_1=0μm, 0.3μm, 0.5μm, 0.88μm respectively. Structures K, L and M are described by (c) with x=0.07, x=0.09 and x=0.15 respectively.

Structure F followed the layer sequence shown in Figure 4.6 (a). The QW thickness in this structure was 7nm thick and compressively strained by 1.05% to the lattice constant of $Al_{0.20}In_{0.80}Sb$, similar to Structure E. The initial buffer layer thickness

was 0.75μm and the Al composition was 7%. This structure had a lower hole density due to the lower doping density. All the other structures, G-M had same doping density. The QW structures G-J followed the layer sequence shown in Figure 4.6 (b). In these structures a 7nm thick QW was compressively strained by 1.32% to the lattice constant of a 1.8μm thick relaxed $Al_{0.25}In_{0.75}Sb$ buffer layer. Structure G had no initial layer and Structures H, I, and J had an $Al_{0.10}In_{0.90}Sb$ initial layer with a thickness of 0.3, 0.5 and 0.88μm, respectively. Structures K-M followed the layer sequence shown in Figure 4.6 (c). The QW was compressively strained by 1.32% to the lattice constant of $Al_{0.25}In_{0.75}Sb$, similar to Structures G-J but the Al composition in the initial layer was varied between 7% and 15%. Structure K had a 0.8μm thick $Al_{0.07}In_{0.93}Sb$ initial layer and a 1.5μm thick $Al_{0.25}In_{0.75}Sb$ buffer layer. Structure L had a 0.9μm $Al_{0.09}In_{0.91}Sb$ initial layer and a 1.7μm thick $Al_{0.25}In_{0.75}Sb$ buffer layer. Structure M had a 0.8μm thick $Al_{0.15}In_{0.85}Sb$ initial layer and a 1.8μm thick $Al_{0.25}In_{0.75}Sb$ buffer layer.

4.4.2 Results and Discussion

The mobility and density of the *p*-type InSb QW structures F-M at 20K and 300K along with the structural parameters are listed in Table 3.2. We observed that the difference between the Al compositions of the initial and the thick relaxed buffer layer had a significant effect on the hole mobility both at room temperature and low temperature.

Structure	W (nm)	Strain (%)	$Al_xIn_{1-x}Sb$ Initial layer composition (x)	Initial layer thickness (μm)	$Al_{0.25}In_{0.75}Sb$ buffer layer thickness (μm)	Density ($10^{11}cm^{-2}$) 20K [300K]	Mobility (cm^2/Vs) 20K [300K]
F (T386)	7	1.06	0.07	0.75	1.80	+2.6 [-1.8]	+70,000[-7380]
G (T453)	7	1.32	0.00	0.00	1.80	+4.0 [+5.7]	+11,900 [+900]
H (T403)	7	1.32	0.10	0.30	1.80	+4.9 [+8.2]	+24,700 [+770]
I (T400)	7	1.32	0.10	0.50	1.80	+4.8[+19.0]	+32,900 [+350]
J (T396)	7	1.32	0.10	0.88	1.80	+4.7 [-6.0]	+50,600[-1400]
K (T388)	6	1.32	0.07	0.80	1.50	+3.6 [-2.2]	+49,600 [-8080]
L (T393)	7	1.32	0.09	0.90	1.70	+4.4 [-2.5]	+52,200 [-4200]
M (T447)	7	1.32	0.15	0.80	1.80	+3.9 [+5.8]	+23,900 [+1050]

Table 4.2: Structural and electronic parameters of the *p*-type InSb QW structures F-M at 20K and 300K. W is the width of the QW. The (+) indicates holes and (-) indicates the electrons.

All the structures without an initial layer were *p*-type at all temperatures, but showed lower hole mobility at low temperatures and high hole mobility at room temperature. The structures E, F and J-L with an initial layer (thickness between 0.75-1.0 μm) were *n*-type at 300K but had higher hole mobility at low-temperatures compared to the structures with no initial layer. The percentage difference between the Al compositions of the initial and the thick relaxed buffer layer of the structures E, F, J, K and L were 15%, 13%, 15%, 18% and 16% respectively. Figure 4.7 shows hole mobility and density at 20K as a function of the difference between the Al compositions

of the initial and thick relaxed buffer layers. Both high hole mobility (μ_h=52,200cm^2/Vs) and high hole density (p=4.4×10^{11}cm^{-2}) were observed in the structure with 16% difference between the Al compositions at the interface of the initial and thick relaxed buffer layers with similar thicknesses at 20K. This structure showed a factor of 4.4 higher hole mobility compared to the structure with no initial layer for the given strain and confinement at 20K. The observed high hole mobility at low temperature in the structures with 15-16% Al percentage difference at the interface could be due to the reduced TD defect density in the well.

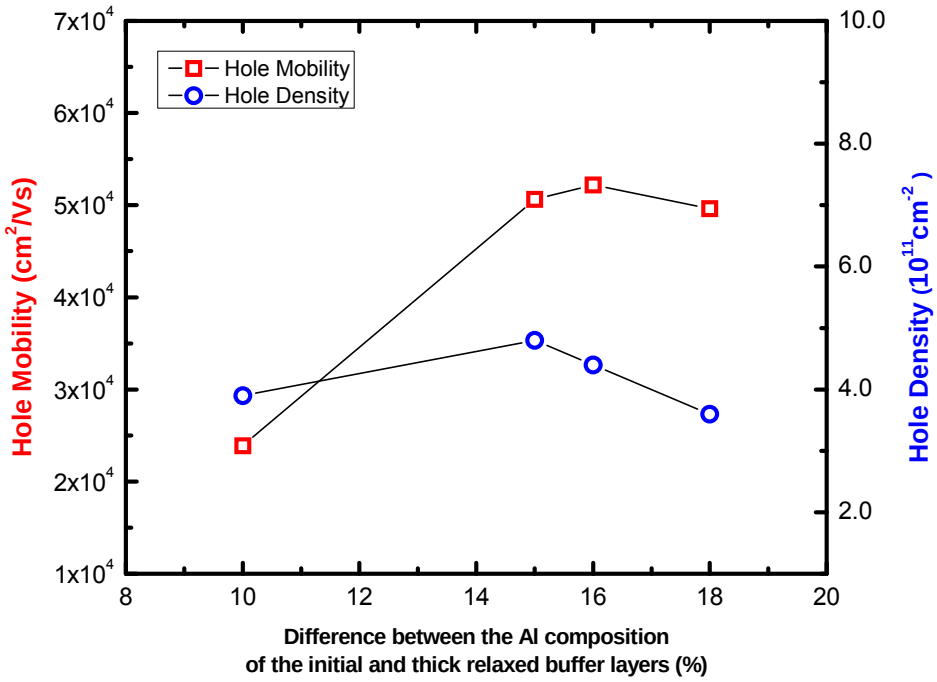

Figure 4.7: The effect of the Al percentage difference at the interface of the initial and thick relaxed buffer layers on hole mobility at 20K.

The thickness of the initial buffer layer also had a significant effect on the hole mobility. In Figure 4.8, the hole mobility and the density (a) at 20K and (b) at 300K are plotted as a function of the initial layer thickness for the structures G (with no initial layer) and H, I and J which had a 15% Al percentage difference at the interface between initial and thick relaxed buffer layers. A high hole density and mobility was observed in the structures with an initial buffer layer compared to the structures with no initial buffer layer at 20K. The hole density at 20K was relatively thickness independent, whereas hole mobility at 20K increased with increasing thickness of the initial layer. High hole mobility (μ_h=50,600 cm^2/Vs) and density (p=4.7×$10^{11}cm^{-2}$) were observed in the structure with 0.88μm thick initial buffer layer. At 20K this structure had a factor of 4.2 (1.5) higher hole mobility compared to the structure with no (structure with 0.5μm) initial buffer layer.

On the other hand the room temperature hole mobility showed a different dependence on the thickness of the initial layer in these structures. As the thickness of the initial buffer layer decreases from 0.88μm (Structure J) to 0.5μm (Structure I) the *n*-type behavior at room temperature changes to *p*-type and the room temperature hole mobility increases as the thickness is further decreased [Fig.4.8 (b)]. The *n*-type conductance at room temperature could be due to the thermally excited intrinsic carriers in the initial layer. In the structures with low Al compositions, the intrinsic carrier density decreases as the thickness of the initial layer decreases.

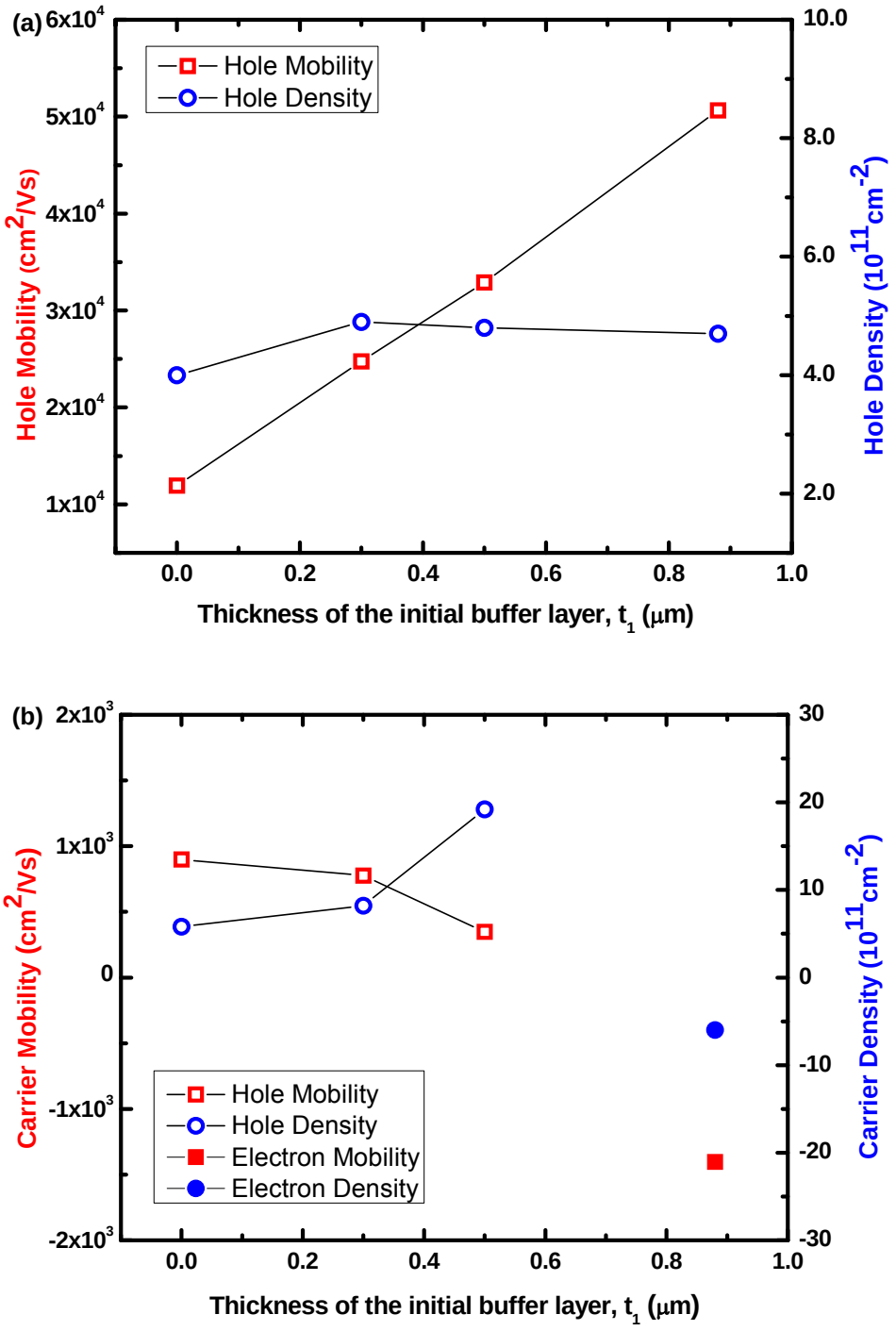

Figure 4.8: The effect of the initial buffer layer thickness on hole mobility (a) at 20K and (b) at 300K. The Al percentage difference at the interface was 15% for the structures with an initial buffer layer.

Figure 4.9 shows a plot of hole mobility and density as a function of the Al percentage difference at the interface of the initial and thick relaxed buffer layer at room temperature. Structure M with a 0.8μm thick $Al_{0.15}In_{0.85}Sb$ initial layer was *p*-type at all temperatures and had the highest hole mobility (μ_h=1,050cm^2/Vs) at 300K. Structure G (μ_h=900cm^2/Vs), with no initial buffer layer, had the next highest mobility at 300K. The percentage difference between the Al composition of the initial and thick relaxed buffer layer of Structure M was 10% and it was lower than that in structures which were *n*-type at 300K. 16% room-temperature hole mobility improvement was observed in the structure with an initial layer compared to the non-initial layer structure.

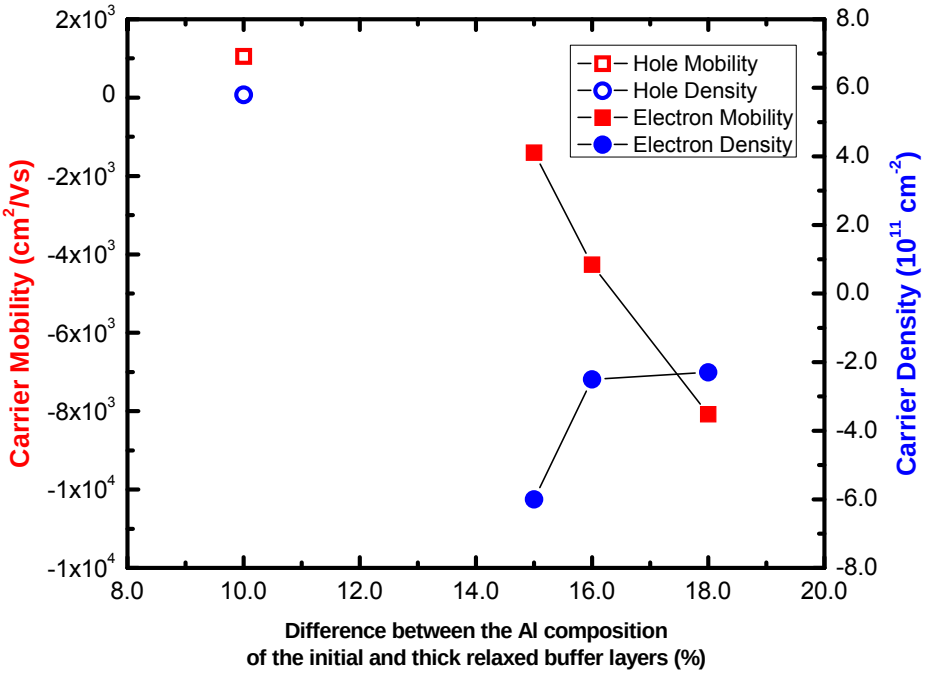

Figure 4.9: The effect of the Al percentage difference at the interface of the initial and thick relaxed buffer layers on hole mobility at 300K.

In summary, both hole mobility and density were further enhanced in the structures with an initial buffer layer, with a dependence on the percentage difference between the Al compositions and the thickness of the initial and thick relaxed buffer layer for a given strain and confinement. This may be due to the different defect densities and/or their propagation through the initial layer in to the QW, which may not be the same in the structures with different Al compositions and the thicknesses. The hole mobility and density at 20K in InSb QWs was enhanced by adding an initial buffer layer with the thickness > 0.8μm and 15-16% difference in the Al compositions. The hole mobility at 300K was enhanced by adding an initial buffer layer with the difference in the Al compositions ≤ 10%. A high hole mobility of 1,050cm^2/Vs was achieved in the improved *p*-type InSb QW with 1.32% compressive strain and a 0.8μm thick initial buffer layer with a 10% difference in the Al compositions.

4.5 2D Hole systems in $In_yGa_{1-y}As$ QWs

Strained *p*-type $In_yGa_{1-y}As$ QWs with remotely Be-doped InP barriers on InP substrates [16], and GaAs barriers on GaAs substrates [8] have previously been reported. Lattice matched (y=0.53) and strained (y=0.65) *p*-type $In_yGa_{1-y}As$ QWs with $Al_{0.52}In_{0.48}As$ barriers have also been reported. 2D hole systems were also realized by direct doping the $In_yGa_{1-y}As$ QW with Be [15]. A doped QW design may increase the ionized dopant scattering as these ionized dopants remain in the well and degrade the carrier mobility. To the best of our knowledge, no transport data were reported for *p*-type $In_yGa_{1-y}As$ QWs with remotely Be-doped $Al_xIn_{1-x}As$ barriers. We have

investigated the doped barrier approach for *p*-type $In_yGa_{1-y}As$ QWs and the hole mobility and density measurements are reported in this section.

4.5.1 Layer structures of *p*-type $In_yGa_{1-y}As/In_xAl_{1-x}As$ QWs.

A series of strain engineered *p*-type $In_yGa_{1-y}As$ with remotely Be-doped $In_yAl_{1-x}As$ barriers were grown on on-axis, semi-insulating InP (001) substrates by MBE. The layer sequences of the QW structures are shown in Figure 4.10. The well and the barrier layers were grown pseudomorphically on a 100nm thick $In_{0.52}Al_{0.48}As$ buffer layer. Biaxial compressive strain was introduced into the $In_yGa_{1-y}As$ layer by slightly varying the In composition in the well or the $In_xAl_{1-x}As$ barrier layers ($x \leq 0.52$), which are lattice matched to InP when y=0.53 and x=0.52. The 2D hole systems were confined within a 10nm thick well. The In composition, y in the $In_yGa_{1-y}As$ QW and that of x in the 20nm thick $In_xAl_{1-x}As$ barrier layers were 0.64 and 0.52 respectively, for the strained well structure. The Indium composition (y) in the well was further increased to 0.64 and 0.75 with the $In_{0.45}Al_{0.55}As$ barriers in order to further improve the hole mobility. The Be δ-doping layer which provides the holes to the well was placed at a spacer thickness of 10nm above the well in the upper barrier. Another Be δ-doped layer which provides the holes to the surface states was placed in the middle of the upper $In_{0.52}Al_{0.48}As$ layer, followed by a 10nm thick $In_{0.53}Ga_{0.47}As$ capping layer. A selective *p*-type $In_yGa_{1-y}As$ QWs grown on InP(001) substrates are listed in Appendix B.

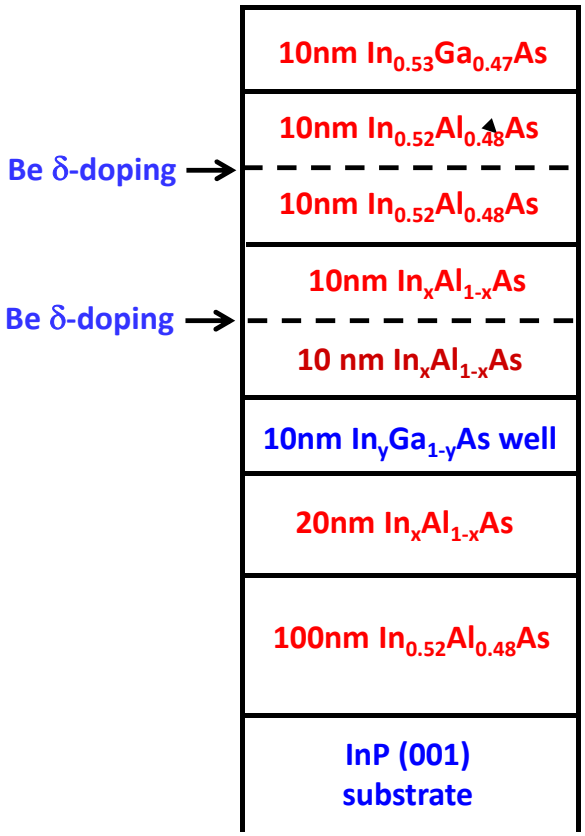

Figure 4.10: The layer structure of a p-type $In_yGa_{1-y}As/In_xAl_{1-x}As$ QW with y=0.64, 0.75 and x=0.52, 0.45.

4.5.2 Results and Discussion

The hole mobility and density were determined by van der Pauw and Hall effect measurements [sec. 2.2] made in a closed cycle refrigerator at temperatures from 300K to 20K. The electrical contacts were made at the corners of a $8\times8mm^2$ square pieces by annealing indium contacts at 400°C for 7min in a 20% H_2:80% N_2 atmosphere. The mobility and density values at 20K and 300K are listed in Table 4.3 along with the In compositions of the well and the barriers. The dependence of the hole mobility on the

QW composition was observed. The temperature dependence of the mobility and the density for a p-type QW with y=0.64 and x=0.52 is shown in Figure 4.11.

structure	y	x	p (10^{11}cm^{-2}) 25K [300K]	μ_h (cm^2/Vs) 25K [300K]
P179	0.64	0.52	9.1 [20.0]	5,340 [140]
P178	0.64	0.45	9.0 [19.0]	4,160 [130]
P185	0.75	0.45	12.3 [11.8]	4,500 [230]

Table 4.3: Structural and electronic parameters of the *p*-type $In_yGa_{1-y}As$ QWs with Be-doped $In_xAl_{1-x}As$ barriers.

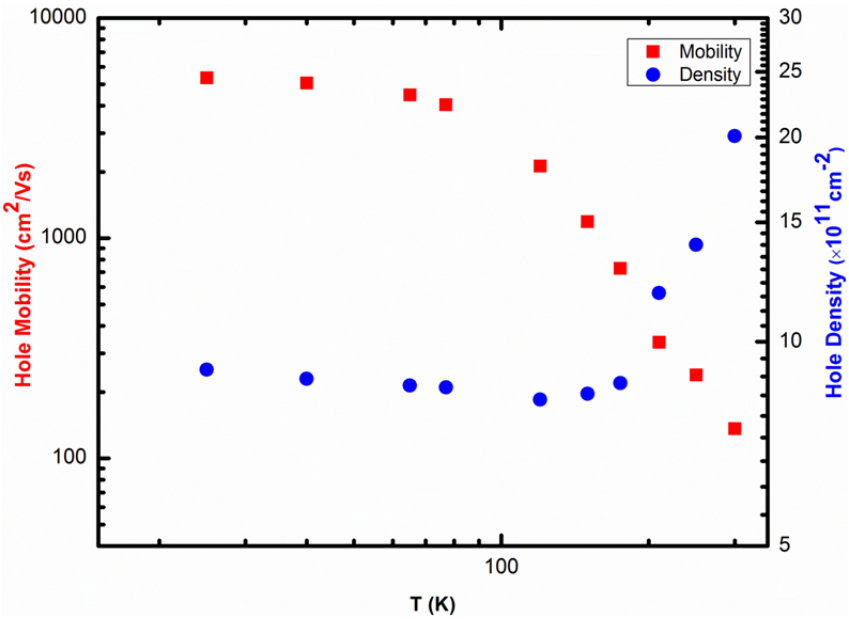

Figure 4.11: The hole mobility and density versus temperature for a strained *p*-type $In_{0.64}Ga_{0.36}As$ QW with Be-doped $In_{0.52}Al_{0.48}As$ barriers.

The mobility in the *p*-type QW with y=0.64 and x=0.52 was ~9 (~70) times smaller at 25K (300K) than in an *n*-type QW with the same layer structure. Improved mobility and density were observed with increased strain. A hole mobility of 230 cm^2/Vs (4,500 cm^2/Vs) was observed for the structure with y=0.75 and x=0.45 with a hole density of 11.8×10^{11} cm^{-2} ($12.3\times10^{11}cm^{-2}$) at 300K (25K). The mobility in this structure was ~4 (~47) times smaller at 25K (300K) than in *n*-type QW with same layer structure. The low-temperature hole mobility for p-type $In_yGa_{1-y}As$ QW was as expected from the ratio of the hole masses (m_h/m_e), however the room-temperature mobility was much lower than expected from the ratio of the m_h/m_e. Population of higher subbands with larger m_h* at 300K may be the reason for the observed low mobilities at 300K. The observed hole mobility in the *p*-type $In_{0.75}Ga_{0.75}As$ QW ($230cm^2/Vs$) was comparable to the reported hole mobility for $In_yGa_{1-y}As$ QW ($260cm^2/Vs$) with y=0.2 [14] and (265 cm^2/Vs) with y=0.65 [15] at 300K. This hole mobility, however, was lower than that of 380, 390, 400 cm^2/Vs for y=0.73, 0.77, 0.82 respectively [16] at 300K. Further optimization of the growth conditions and layer thickness in order to fully utilize the strain, would be needed to obtain higher hole mobility in our $In_yGa_{1-y}As$ QWs.

Chapter 5

Epitaxial Growth of Elemental Sb Quantum Wells

5.0 Introduction

Since the 1980s, there have been several reports on the formation of antimony (Sb) thin films. An Sb film was evaporated on GaAs (110) [1, 2], InP (110) [2, 3] and InP (100) [4] for use as a capping layer or as a Schottky barrier. Efforts on the epitaxial growth of Sb on InSb (111) [5] and GaSb (111) [6-8] were also reported. InSb and GaSb are direct gap semiconductors whereas Sb is a semimetal with an indirect negative band gap. The motivation in Reference 6-8 was to develop the Sb/GaSb system as an indirect narrow gap/direct gap superlattice, presuming that sufficient quantum confinement would open up an indirect gap in the Sb layers. Since the Sb films in the initial research were restricted to a thickness greater than ~16 nm, the indirect gap in Sb was not observed. Some subsequent research was reported on ultra-thin films of Sb on Si (111) [9, 10].

Elemental Sb has gained more attention recently because calculations indicate that the inherently large spin-orbit coupling enables topological insulator (TI) behavior [11]. The large atomic number of Sb results in a large spin-orbit coupling for electrons in crystalline Sb and in compounds and alloys that contain Sb. TIs are a new class of materials that are electrical insulators in their bulk interior, but electrical conductors at their surfaces. Their conducting surface states are topologically protected from elastic backscattering [11], unlike those found in ordinary two-dimensional (2D) electron

systems. Although elemental bulk Bi and Sb are semimetals, particular alloy compositions of BiSb are semiconducting and these alloys were the first materials identified as three-dimensional (3D) TIs. While the semimetallic states in bulk Sb preclude TI behavior, recently topoelectronic phase transitions in Sb films as a function of film thickness have been predicted [12]. A semimetal-to-3D TI transition induced by quantum confinement is expected at a critical thickness of ~7.8 nm, a 3D TI-to-2D quantum spin Hall state transition at a critical thickness of ~2.7 nm, and a trivial semiconductor state for films thinner than ~1 nm [12]. The search for these topological phases has motivated our recent studies of atomically flat, ultra-thin Sb films.

Sb crystallizes in a rhombohedral structure with the atoms forming in bilayers (BLs). Angle-resolved photoemission spectroscopy (ARPES) experiments have been performed on a 20-BL (~7.2 nm) Sb film prepared on a Bi-terminated Si (111) substrate [10]. The ARPES measurement revealed surface states that crossed in a Dirac cone at the zone center; however no transport measurements were reported. The 2D TI properties of a different thin film TI (1-BL Bi thin films grown on Bi_2Te_3 substrates) have been experimentally observed using scanning tunneling microscopy (STM), scanning tunneling spectroscopy (STS) [13] and ARPES [14]. Our effort focuses on a comparable suppression of the semimetallic behavior by means of quantum confinement in order to enable electrical transport experiments that probe the topological surface states. A quantum-confined 2D TI was first discovered in a HgTe QW with $Hg_{0.3}Cd_{0.7}Te$ barriers and was observed through transport measurements [15].

Zincblende GaSb can serve as a barrier material for rhombohedral Sb. Its bandgap (0.8 eV at low temperature) is larger than predicted for Sb layers thicker than 3

bilayers [12] and both GaSb (111) and Sb have a hexagonal arrangement of surface atoms with nearly identical nearest-neighbor distances [6]; therefore epitaxial growth of Sb is feasible on the (111) surface of GaSb. To study transport in any TI material, it is essential to minimize non-topological bulk and surface states originating from defects or unintentional dopants, as they can dominate the conductivity if their density is sufficiently high. The elemental composition of Sb may result in fewer crystalline defects compared to compounds (Bi_2Te_3, Bi_2Se_3) or alloys (Bi_xSb_{1-x}) which are also being studied as potential topological materials.

We have developed a molecular beam epitaxy (MBE) procedure to realize ultra-thin films of Sb with good crystalline quality. In the procedure used by earlier researchers [5-8], Sb was epitaxially grown by cooling the substrate while exposing it to a flux of Sb. However, the growth of Sb at intermediate temperatures increases the uncertainty in film thickness. Depositions of Sb thin films with controlled thicknesses have been discussed in the literature [2-4, 9], but the films were not grown by MBE and the thickness was not considered a critical variable for potential as a TI. In our revised procedure, Sb is epitaxially grown by opening the Sb shutter only after the substrate has reached a fixed low temperature. In this chapter, epitaxial Sb ultra-thin films grown using the revised procedure, including characterization of the structural and electrical properties will be described.

The chapter is organized as follows. First, a brief review of topological insulators is given. Next, epitaxial Sb QWs grown using the revised procedure on GaAs(111)A substrates, and their structural and electrical properties are described. Resistivity measurements indicated that Sb wells with a thickness above ~2 nm were

metallic (relatively temperature-independent resistivity) whereas thinner wells showed insulating or semiconducting behavior (resistivity increased with decreasing temperature) [16]. In order to minimize the defects, the Sb QWs were grown on GaSb (111)A substrates. Then, the structural and electrical properties of the films grown on GaSb(111)A substrate are described.

In order to measure the semiconducting band gap of quantum confined Sb using transport experiments, existing bulk conduction through GaSb epilayers need to be reduced. As a potential solution, AlSb which exhibits high resistivity was substituted as the barrier material for Sb. Preliminary results of our initial experimental investigations on epitaxial growth of Sb with AlSb barrier layers on a GaAs (111) substrate are reported at the end of the chapter.

5.1 Brief review of Topological Insulators

Interest in topological insulators has exploded because of their exotic properties which can be used for future spintronics and quantum computing applications. These are a new class of materials that are insulating in the bulk due to an energy gap separating the valence and conduction bands, but conducting at the surface due to gapless states on the boundary. TIs can be 3D or 2D. The 3D TIs are bulk insulators with 2D metallic surface states, whereas the 2D TIs, which are also known as 2D quantum spin hall (QSH) state, have one-dimensional (1D) edge states. These surface/edge states are generated by the spin orbit interactions and are distinct from all other known states of matter, including quantum Hall (QH) state. The surface/edge states in a TI are protected from elastic backscattering by time reversal (TR) symmetry

[11]. These metallic states are “helical”, that is the spin of the carriers are locked in a right angle with its momentum. A pair of edge states at a given edge counter propagate with opposite spins [11]. The up spins propagate in one direction while down spins propagate in the other direction (Fig. 5.1). These helical edge states can be transmitted through even strong disorder by flipping the spin and changing the path by π - (- π) = 2π full rotation in the disordered region [17].

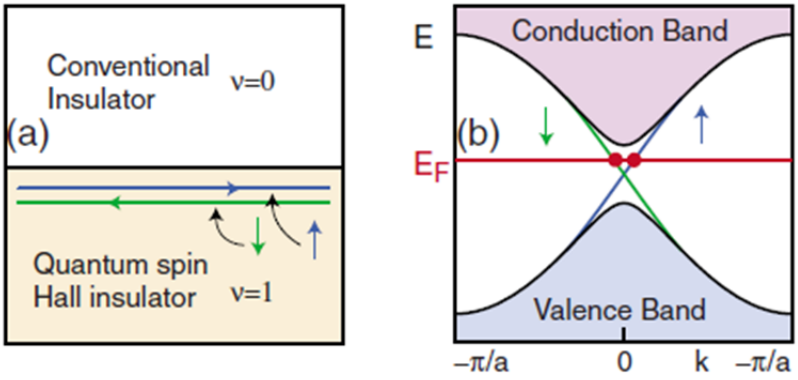

Figure 5.1: Pair of Edge states in the QSH insulator. (a) The interface between a QSH state and an ordinary insulator (ex. vacuum). Up and down spins propagate in opposite directions. (b) The edge states have Dirac like dispersion in the gap. Figure is adapted from ref. 11.

Ordinary insulators and TIs mathematically distinguished by distinct topological invariants Z_2 (ν_0=0, 1) depending on the role of TR symmetry for spin ½ particles [11, 18]. For 3D case, strong and weak TIs can be found. ν_0 = 0 identifies the weak TI whereas ν_0= 1 identifies a strong TI. The surface Brillouin zone has four TR invariant points $\Gamma_{1,2,3,4}$ [Fig. 5.2(a) and (b)]. In a TIthese points are degenerate (Kramers theorem)

with up and down spins [Fig. 5.2(a) and (b)] and form 2D Dirac points [Fig. 5.2(c)] [11]. Whether an odd or even number of spin degenerate Dirac points are enclosed by the Fermi surface determines the strong or weak nature of the TI state. If the Fermi furface encloses an odd number of Dirac points, the surface become a strong TI [Fig. 5.2(b)]. When the Fermi surface encloses an even number of Dirac points, the state is referred to as a weak TI [Fig 5.2(a)]. The surface states in a weak TI are not protected against strong disorder by the TR symmetry.

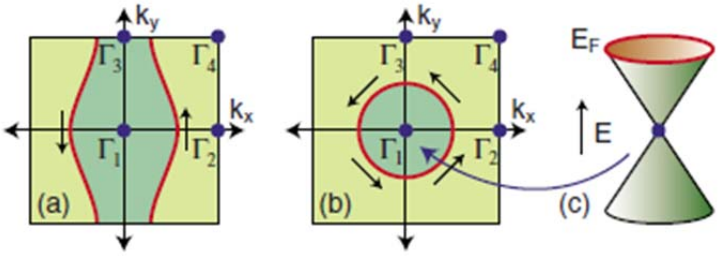

Figure 5.2: Fermi circles in the surface Brillouin zone for (a) a weak TI and (b) a strong TI. The spin of the metallic surface states go around the Fermi circle required by the TR symmetry such that states at momenta **k** and **–k** have opposite spins (helical). (c) In the strong TI the Fermi circle encloses a single (simplest case) Dirac point. Figure is adapted from ref. 11.

In a QH state back scattering by an impurity is suppressed, but TR symmetry is broken in the presence of a magnetic field. The edge states give rise to quantized conductance, which take integer values in units of e^2/h (1/25,813Ω) at low temperature and high magnetic field. In a TI state spin-polarized spatially separated edge states

which form a single Dirac cone on the boundary will give rise to conductance (non-quantized) even without a magnetic field [17]. In strong topological insulators, under an applied magnetic field the surface Hall conductivity will be quantized in half integers, $\sigma_{xy} = (n+1/2)\ e^2/h$ [19]. Half integer quantization of the Hall conductivity in strong topological insulators can be explained by the surface Dirac fermions whose sign of the effective mass plays an important role [17, 19, and 20]. The Hall conductance for massless Dirac fermions is $(n + 1/2)\ e^2/h$ [20]. This can be applied to the strong TI. Due to the spin texture the Dirac fermions in TI acquire a mass (Zeeman term) which opens a gap by breaking the TR symmetry on the surface (but not in the bulk) under an applied magnetic field [17, 19]. In a slab geometry the strong TI with a single Dirac point on the surface can be considered as an interface between two phases, the vacuum (conventional insulator) and TI. These two phases are shared by the 3D (2+1) Dirac fermions whose mass is equal but (+) on top and (-) on the bottom and leads to massless (gapless) Dirac fermions in between (on the surface) at zero energy. Therefore when the two surfaces share a single Dirac point and the Fermi level crossing the zero mode Landau level the surface Hall conductivity is half integer quantized. However, in the standard transport experiments, both surfaces will be measured in parallel doubling the half.

Search for topological insulators is growing rapidly, since it was first discovered experimentally in HgTe quantum wells. Material compounds composed of heavy elements such as Bi, Sb, Te or Hg exhibit strong spin-orbit coupling which enables the topological insulator behavior. In HgTe QW with CdTe barriers, the bulk band inversion lead to the Dirac like dispersion of the surface bands revealing a 2D QSH

state, for the well thickness, d > 6.3nm [15]. A conductance plateau of $2e^2/h$ was measured independent of the sample width indicating that the transport was at the edge. Bi_xSb_{1-x} was predicted to be a strong 3D TI for a certain range of composition, x ($0.09 < x < 0.18$) [19] and was the first experimentally discovered TI for the 3D class [21]. Topologically nontrivial surface states were mapped in an angle-resolved photoemission spectroscopy (ARPES). Later, it has been observed in the newer generation 3D materials such as Bi_2Se_3 [22], Bi_2Te_3 [23], and elemental Sb [10]. In all these cases the surface states with a single Dirac cone were mapped in ARPES or in STM. Because of the non-topological surface states due to the anti-site defects and intrinsic doping, the transport experiments in TI are challenging. Successful transport experiments have been performed on thin HgTe QWs [15] and 70nm thick, strained HgTe layer [24] by revealing 2D and 3D TI, respectively. Low carrier density in these materials lead to the bulk insulating regime at low temperature and observation of the QH effect from the TI states. Majority of these high quality TI materials are grown by the MBE. Our studies on searching for new TI in elemental Sb focus on suppression of the bulk semimetallic behavior of Sb by means of quantum confinement. Once the materials are available with sufficient purity in supporting the bulk insulating behavior, topological insulators will offer a platform to explore many new topoeltronic devices.

5.2 Experimental Procedures

5.2.1 Substrate preparation

The 2 inch diameter semi-insulating GaAs (111) substrates used in this study were double side polished with one side A and the other side B. Surface A (B) of the

GaAs(111) substrate is Ga (As) terminated with a single dangling bond per atom. The wafer was cleaved into four pieces by scribing on the back side or B side. Because these wafers were thinner (thickness ~300μm) than usual 2 inch InP(001) or 2 inch GaAs(001) wafers (typical thickness> 325μm) they did not fit very well within the spring plates which are made to hold 600μm thick wafers. Therefore, a quarter of a 2 inch GaAs (111)A wafer was loaded with another quarter of the same wafer in a stack to avoid the fluctuations of substrate temperature during rotation. Each GaAs (111)A substrate was degased at 300°C for ~12 hours at the heated station in the buffer chamber before loading into the growth chamber. The native oxide layer was desorbed (680°C-720°C) with an Sb_2 over pressure. The substrate was annealed for 3-5min at a temperature of ~10°C higher than the oxide desorption temperature.

The 2 inch GaSb (111) wafers used in this study were ~1mm thick, *n*-type doped, only polished on the A side. The wafer was cleaved into ~1×1cm^2 pieces by scribing on the back side and placing between two glass slides covered with particle free clean paper. Each GaSb (111)A substrate was degased at 250°C for ~12 hours at the heated station prior to transferring in to the growth chamber. The native oxide layer was desorbed at ~450-460 °C under an Sb flux. The substrate was then annealed for ~10 and 5min at a temperature of ~10 and 20°C higher than the oxide desorption temperature, respectively.

5.2.2 Epitaxial growth and post growth characterization

All growths were performed in an Intevac Gen II MBE chamber equipped with an Sb cracker cell. The growth was monitored *in situ* by using reflection high energy electron diffraction (RHEED).

Sb QW structures were structurally characterized through scanning electron microscopy (SEM), field-emission SEM (FE-SEM) and field-emission transmission electron microscopy (FE-TEM). Due to the absence of RHEED intensity oscillations during the deposition of Sb, the growth rate was determined from cross-sectional SEM measurements of thick Sb films with deposition times of 9 to 60 min. The thickness and structural parameters of one ultra-thin Sb layer was determined by cross-sectional TEM measurements. Some of the thicker Sb films were characterized through high resolution X-ray diffraction measurements (HR-XRD).

The electrical resistivity of the Sb films was measured in the van der Pauw geometry using four-wire measurements in a closed-cycle refrigerator at temperatures from 300 to 20K. The electrical contact was made by pressing pure indium on the corners of square pieces with ~5 or ~8 mm long edges. The indium contacts were not annealed in order to avoid parallel conduction through the substrate. Ohmic contact was checked using two-wire measurements and confirmed through observation of linear current -voltage characteristics at 300, 77 and 20K.

5.3 Epitaxial growth of Sb: revised procedure on GaAs (111)A

A series of Sb quantum well (QW) structures were grown on semi-insulating GaAs (111)A substrates with GaSb buffer layers. The simple layer sequence for the Sb QW structures is shown in Fig. 5.3. The GaSb buffer layer and the GaSb cap layer are expected to act as barriers for carriers in the Sb layer.

Prior to the growth of the Sb layer, a 0.5μm thick GaSb (111) buffer layer was grown on the GaAs (111)A substrate at a temperature of ~100°C below the oxide desorption temperature (580°C), at a rate of 0.45 monolayers (ML) per second, and under an Sb_2 rich condition with an Sb_2:Ga beam flux ratio of ~4.1. The surface reconstruction gave rise to a 2×6 RHEED pattern that was maintained during the growth of the GaSb buffer layer as shown in Figs. 5.4(a) and 5.5(a).

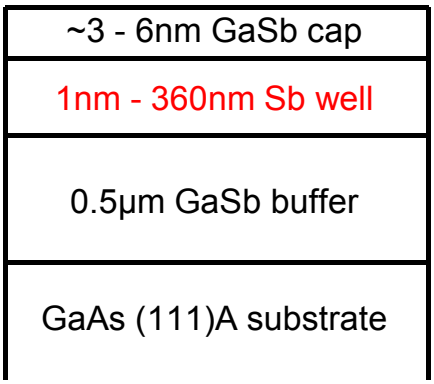

Figure 5.3: Layer sequence for the Sb QW structures grown on GaAs(111)A substrate.

Following the original growth procedure, the substrate temperature was lowered to ~220°C under an Sb flux after closing the Ga shutter. The RHEED pattern changed to 5×1 as the temperature was lowered [Fig. 5.4(b)] and gradually weakened as Sb began

to nucleate on the cooling surface [Fig. 5.4(c)]. It eventually changed to 1×2 when a sufficiently thick Sb layer formed on the surface [Fig. 5.4(d)]. We found that this method was impractical for realizing ultra-thin films of Sb because it provided only limited thickness control.

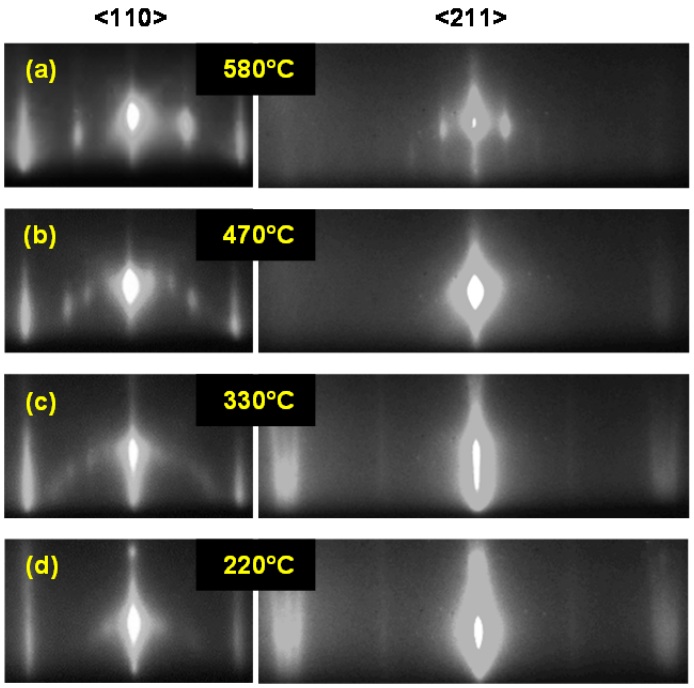

Figure 5.4: RHEED patterns along the <110> and <211> directions for a GaSb (111)A surface under an Sb flux at (a) ~580°C after growth of the GaSb buffer layer, (b) ~470°C with negligible Sb on the surface, (c) ~330°C with some Sb at the surface, and (d) ~220°C with complete Sb coverage of the surface.

In the revised procedure, the Sb layer is epitaxially grown at a fixed substrate temperature. After closing the Ga shutter [Fig. 5.5(a)], the substrate temperature was

lowered under an Sb flux with the RHEED pattern changing from 2×6 to 5×1. The Sb shutter was closed at a substrate temperature of ~65°C below this transition temperature. The substrate temperature was further lowered about ~200°C without an Sb flux. The RHEED pattern remained 5×1 after the Sb shutter was closed [Fig. 5.5(b)] and during the additional temperature reduction. The Sb shutter was reopened at a substrate temperature of ~300°C or ~280°C (~265°C below the transition temperature) to grow an epitaxial thin Sb layer at this fixed temperature with a constant flux. A streaky 1×1 RHEED pattern observed after growth of the Sb layer indicated a smooth surface [Fig. 5.5(c)]. After deposition of the Sb layer, migration enhanced epitaxy [25] (MEE) was used to grow a GaSb cap layer [Fig. 5.5(d)]. For this capping layer the shutters were cycled multiple times through a two-step sequence (only Ga shutter open for ~1ML, followed by only Sb shutter open for ~1ML) or a three-step sequence (both shutters closed for ~1sec between steps 1 and 2). Uncapped structures were also grown in order to investigate the surface morphology of the Sb layer.

5.3.1 Structural Properties and surface morphology

Figures 5.6(a) and 5.6(b) show cross-sectional SEM images of two thick films of Sb deposited using the revised growth procedure at 300°C. The Sb layer deposited for 30 min (~174 nm) was almost exactly half as thick as the Sb layer deposited for 60 min (~360 nm), indicating that the growth rate of Sb is well controlled using the revised growth procedure. From these data, the growth rate of Sb was found to be 0.1 nm/sec for a substrate temperature of 300°C. A similar growth rate was found for a substrate temperature of 280°C.

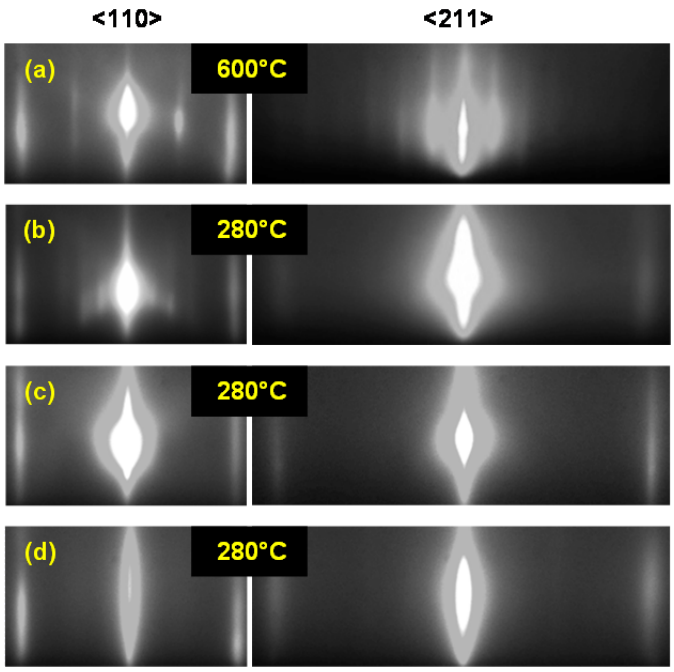

Figure 5.5: RHEED patterns along the <110> and <211> directions for a GaSb(111)A surface (a) at ~600°C, after the growth of a GaSb buffer layer under an Sb flux, and a GaSb (111)A surface at ~ 280°C without a Sb flux, (b) just before the Sb QW growth, (c) after the Sb QW growth, and (d) after the GaSb cap layer growth. The RHEED patterns in (d) were captured during a different growth than the patterns in (a), (b), and (c).

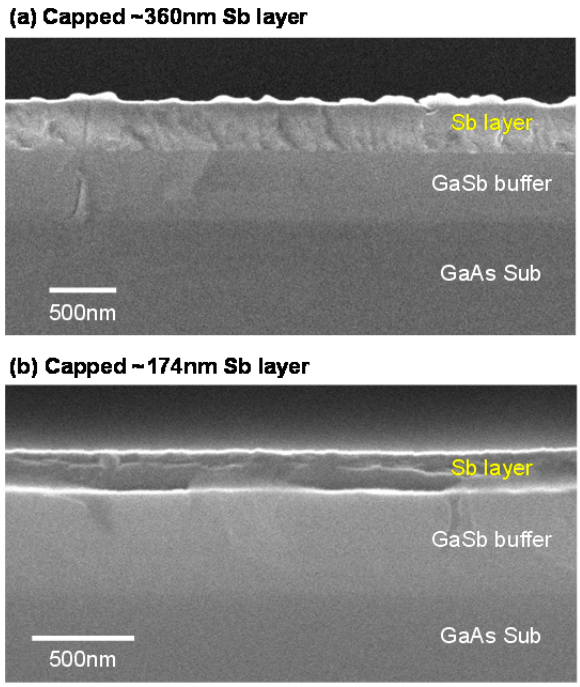

Figure 5.6: Cross-sectional SEM images of thick Sb films grown at 300°C for deposition times of (a) 60 min and (b) 30 min. The images show thicknesses (~360nm and ~174nm) that scale well with deposition times. Roughness due to cleaving can be seen in the images.

Figures 5.7(a) and 5.7(b) show cross-sectional TEM images of an ultra-thin Sb layer grown at 300°C. As expected, 41 seconds of Sb growth resulted in a thickness of 4.1 to 4.5 nm [Fig. 5.7(b)], indicating good control over the growth rate even for ultra-thin layers. The image with higher resolution [Fig. 5.7(b)] shows well-ordered crystalline layers of GaSb and Sb and sharp interfaces. Within the experimental resolution, both GaSb and Sb have the expected crystal structures and the expected interatomic distances (3.52 Å for GaSb and 3.76 Å for Sb) along the growth direction. As evident in Figure 5.7(a) and 5.7(b), the TEM images also reveal trench features that

indicate that the GaSb cap layer does not completely cover the surface of the Sb film. An accurate measure of the surface coverage cannot be obtained from these images because of the limited size of the images and the thinness of the TEM specimen.

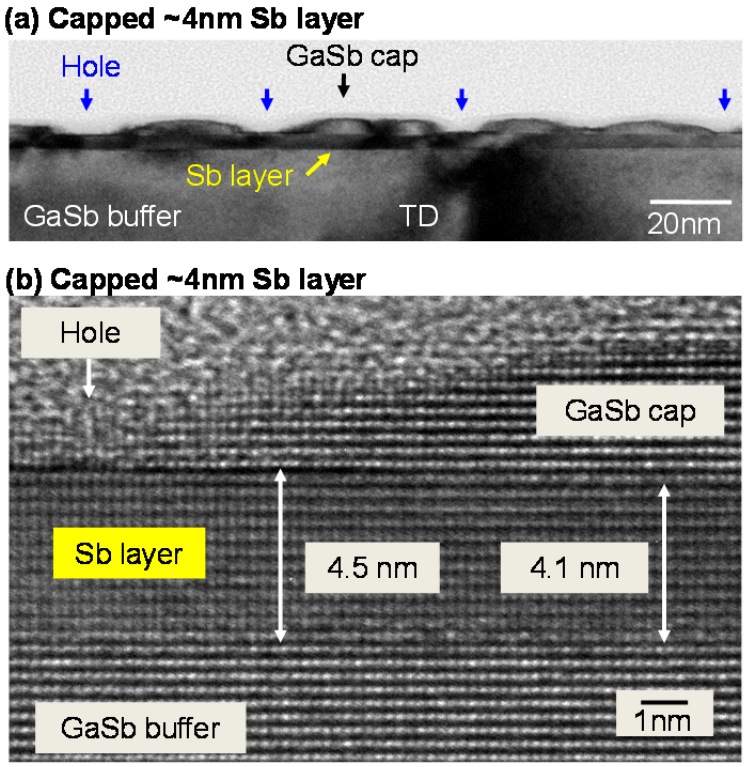

Figure 5.7: Cross-sectional TEM images of an ultra-thin Sb structure showing (a) a larger area of the well-ordered ultra-thin Sb layer, and (b) sharp interfaces between the Sb and GaSb layers under high resolution. The images were captured from the <211> direction. A non-uniform coverage of the GaSb cap layer is seen in both images. In (a), the image contrast due to a threading dislocation (TD) can be seen.

Three plan-view FE-SEM images are shown in Figure 5.8. These images were obtained with an annular backscatter detector and with the electron beam at near normal incidence. The contrast in this mode is particularly sensitive to crystalline defects and strain, in addition to compositional differences. The shape of the triangular features appearing in all three FE-SEM images is due to the three-fold symmetry of the hexagonal arrangement of atoms on the surface. The positions of dark point-like features correspond to the emerging edges of threading dislocations on the surface, which arise from the 7.8% lattice mismatch between the GaAs substrate and the GaSb and Sb epilayers.

Figure 5.8(a) is a plan-view FE-SEM image of a larger area of the same structure analyzed in Figure 5.7. The light gray/white areas are the GaSb cap layer, while the black areas are voids in the cap layer or defects in the Sb and/or cap layer. In this image, the dark gray areas are also voids in the cap layer. The voids in the FE-SEM image of Figure 5.8(a) correspond to the holes seen in the TEM images of Figure 5.7. Quantitative analysis of Figure 5.8(a) yields a value of 85% for the surface coverage of the GaSb cap layer, which is higher than one might have expected from the TEM images. For this structure, the GaSb cap layer (~3 nm) was grown by the two-step MEE procedure at 300 °C. In the series of structures grown at 280 °C, a thicker GaSb cap layer (~6 nm) was deposited and the three-step MEE procedure was used. The FE-SEM image of such a structure, with an Sb thickness of ~1.5 nm, is shown in Figure 5.8(b) and was obtained under different conditions than used in Figure 5.8(a). As in Figure 5.8(a), the light gray/white areas are the GaSb cap layer while the black areas are voids

in the cap layer or defects in the Sb and/or cap layer. Quantitative analysis of Figure 5.8(b) shows an improved coverage of 96% for the GaSb cap layer.

In order to study the morphology of a thin Sb layer (nominally ~1.5 nm), an uncapped structure was grown at 280 °C. The FE-SEM image of the uncapped structure is shown in Figure 5.8(c). Unlike in Figures 5.8(a) and 5.8(b), the bright areas correspond to the Sb layer while the dark areas are voids in the Sb layer or defects in the Sb or GaSb buffer layer. As expected, the number of threading dislocations (dark point-like features) in Figure 5.8(c) is similar to the numbers seen in Figures 5.8(a) and 5.8(b). The closed-loop dark line contrasts, which were not seen in Figures 5.8(a) and 5.8(b), are reminiscent of step edges. In a similar uncapped Sb structure, we made a careful FE-SEM and atomic force microscopy (AFM) study of the same area. Line contrasts were observed in FE-SEM images using backscattered electrons while step edges were seen in AFM and low-energy (1 keV) FE-SEM images using secondary electrons. The line contrasts did not correlate with the step edges. We instead attribute the line contrasts to undulations in the strain of the thin Sb epilayer. Because bulk Sb is nearly lattice-matched to bulk GaSb, the appearance of the strain features is surprising. The interpretation may be additionally complicated by the presence of an oxide layer that forms during exposure of the Sb surface to air. This oxide layer could induce the strain lines seen in the FE-SEM image of the Sb layer. Image analysis of Figure 5.8(c) yields a value of 93% for the surface coverage of the thin Sb layer.

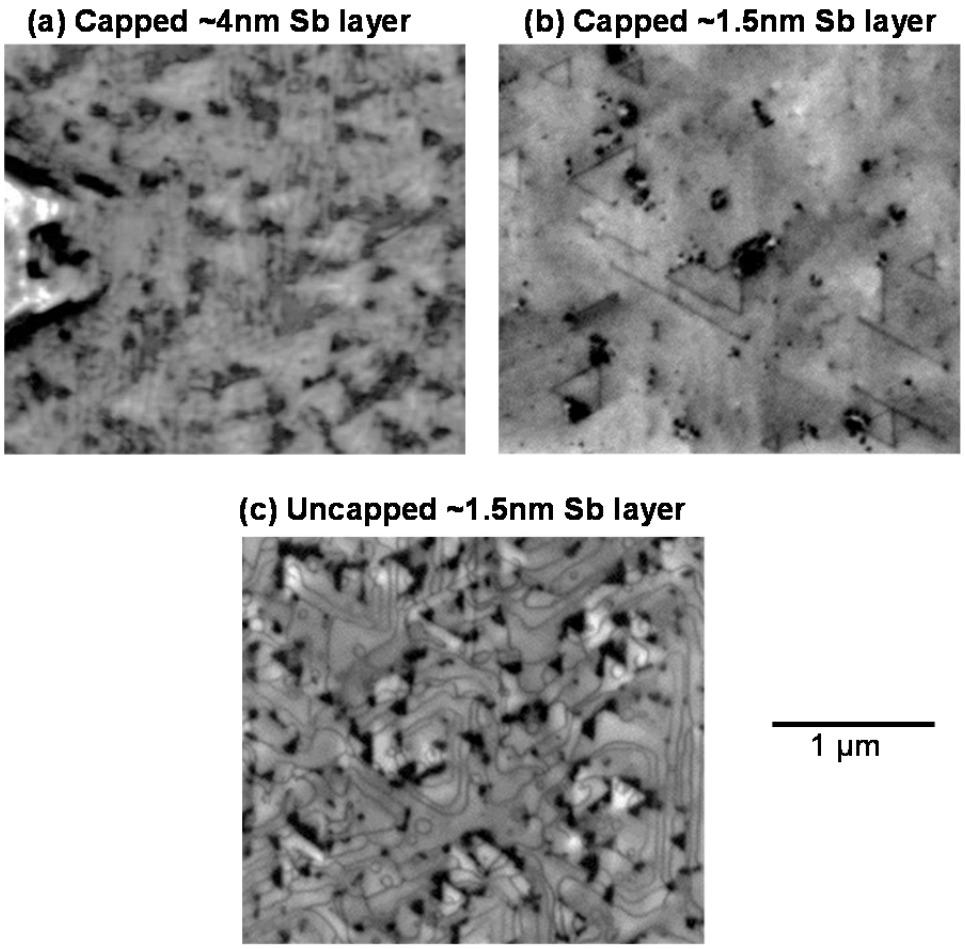

Figure 5.8: Plan view FE-SEM images of the surface of an ultra-thin Sb structure (a) grown at 300 °C with a ~3 nm GaSb cap layer, (b) grown at 280 °C with a ~6 nm GaSb cap layer and (c) grown at 280 °C without a GaSb cap layer. The thickness of the Sb layer is noted in each image. The surface morphology of both the cap layer and the Sb layer grown at 280 °C is more uniform than for the capped structure grown at 300 °C. The scale bar is 1 μm long.

5.3.2 Electrical Properties

Figure 5.9 shows the temperature dependence of the 2D electrical resistivity of a series of capped Sb layers grown at 280 °C, with a nominal Sb thickness ranging from 1 to 4 nm. The actual Sb thickness may be slightly larger (~0.6 nm) due to leakage around a closed Sb shutter or other systematic uncertainties.

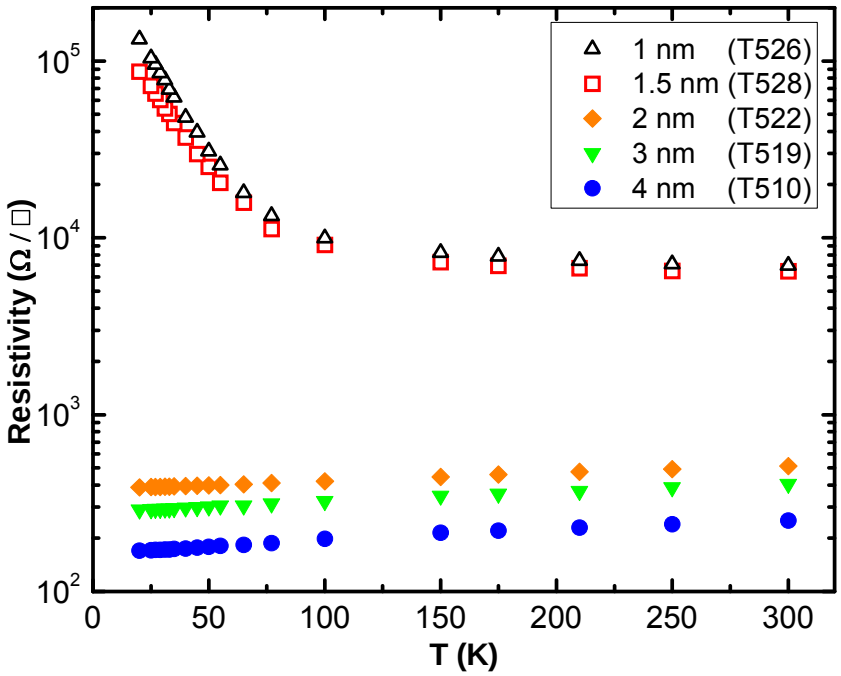

Figure 5.9: Two-dimensional electrical resistivity versus temperature for ultra-thin Sb layers with different thicknesses grown on GaAs (111)A substrates at 280°C.

In principle, the GaSb cap layer can affect the resistivity measurement by providing an alternate conduction path and/or by modifying the Fermi energy in the Sb layer. We have ruled out the former effect by measuring the resistivity of a 500 nm-thick GaSb epilayer on a semi-insulating GaAs (111)A substrate. Because the

measured resistivity was 8×10^3 Ω/□ at 20 K (4×10^3 Ω/□ at 300 K), we expect that a 6 nm thick GaSb cap layer would have a resistivity of 6.7×10^5 Ω/□ at 20 K (3.3×10^5 Ω/□ at 300 K). This is a factor of 5 to 3300 larger at 20 K (33 to 1700 larger at 300 K) than the measured resistivity of the five structures represented in Figure 5.9, which indicates that conduction through the GaSb cap layer is negligible.

Insight into the latter effect, Fermi energy modification, can be gained by noting that two of the five structures have a resistivity that is a factor of ~100 larger than the underlying 500 nm-thick GaSb layer. This implies that a potential energy barrier (a Schottky barrier in the case of semi-metallic Sb) prevents carriers from going into the underlying GaSb layer. It is reasonable to assume that the GaSb cap layer also gives rise to a potential barrier that confines carriers to the Sb layer. Hence the resistivity experiment predominantly measures conduction through the Sb layer rather than through the GaSb barriers.

Because the electrical properties of a quantum well can depend on the composition of the barrier layers, the GaSb cap layer should fully cover the Sb layer for straightforward interpretation of the resistivity data. According to FE-SEM analyses, the GaSb coverage is similarly high for all the structures listed in Figure 5.9. Because the coverages of the Sb layer [(Figure 5.8(c)] and GaSb cap layer [Figure 5.8(b)] are both high and the uncovered areas are not clustered together, we assume that the electrical properties are similar to the behavior of a complete Sb layer with a complete GaSb cap.

At a fixed temperature, the resistivity increases with decreasing film thickness for all five structures. At low temperature the resistivity is approximately inversely proportional to thickness for the films of thickness 2, 3, and 4 nm, as one would expect

for conduction dominated by a semimetal. The relative temperature independence of the resistivity for these three Sb structures is also consistent with semimetallic behavior.

For Sb films with thicknesses of 1 and 1.5 nm, the resistivity increases with decreasing temperature and is significantly larger at any temperature than expected from extrapolating the thickness dependence of the 2, 3, and 4 nm-thick Sb layers. These behaviors imply that the 1 nm and 1.5 nm layers are insulating, or semiconducting. Recent first-principles calculations [12] have predicted insulating behavior for ~1 nm-thick layers of Sb and conducting behavior through topological surface states for a thickness of ~1 to 2.7 nm. These predictions are consistent with our observations, but our resistivity measurements cannot discriminate between surface and interior conduction. A qualitatively similar semimetal to semiconductor transition between ~30 and 20 nm was observed for Bi films grown on Si (111) and attributed to quantum confinement [26]. For our experiments on ultra-thin Sb films, Figure 5.8(c) implies that the high resistivity in the thinnest layers is not due to incomplete Sb coverage. Nevertheless, we have not ruled out the possibility that the observed insulating behavior is due to structural properties rather than quantum confinement. A firmer conclusion would be reached if theoretical modeling was performed to include the effects of GaSb barrier layers and explicitly calculate the expected electrical conductivity.

5.4 Epitaxial growth of Sb: revised procedure on GaSb(111)A substrate

In order to obtain Sb thin films with better crystalline quality, growth of Sb QWs was switched to GaSb(111)A substrates. We observed that the initial conditions for the epitaxial growth of Sb on GaSb (111) are on GaSb (111)A substrate is different compared to that of on GaAs (111)A substrate.

A series of uncapped Sb ultra-thin films were grown on *n*-doped GaSb (111)A substrates with a GaSb homo-epitaxial buffer layer. The vacuum and the GaSb buffer layer are expected to act as the upper and the lower barriers respectively, for carriers in the Sb layer. The simple layer sequence for the Sb QW structures is shown in Fig. 5.10.

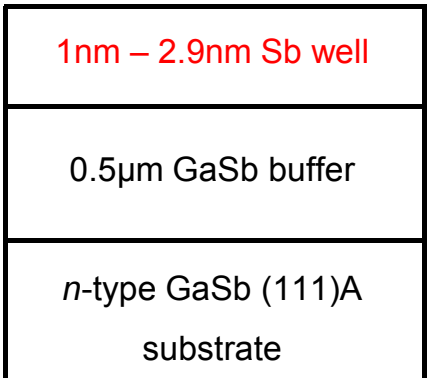

Figure 5.10: Layer sequence for the Sb QW structures grown on *n*-GaSb(111)A substrate.

Following the revised growth procedure on a GaAs (111)A substrate, first, a 0.5μm thick GaSb homo epitaxial layer was grown at a temperature of ~90-100°C below the oxide desorption temperature, at a rate of 0.45 monolayers (ML) per second, and under an Sb_2 rich condition with an Sb_2:Ga beam flux ratio of ~4.1. The surface

reconstruction gave rise to a 2×6 RHEED pattern that was maintained during the growth of the GaSb buffer layer as shown in Figure 5.11(a). After growth of the GaSb buffer layer the wafer was annealed for ~5min at a temperature of 5-10°C higher than the growth temperature under an Sb flux. The substrate temperature was then lowered under an Sb flux with the RHEED pattern changing from 2×6 to 5×1. The Sb shutter was closed at a substrate temperature of ~350°C (~100°C below this transition). The wafer was annealed without an Sb flux at this temperature until the RHEED pattern changes from 5×1 back to 2×6. A slower out-diffusion of Sb on the surface is necessary in order to obtain a smooth surface. The substrate temperature was further lowered ~165°C without an Sb flux. The RHEED pattern remained 2×6 during the additional temperature reduction and just before the QW growth [Fig. 5.11 (b)]. The Sb shutter was reopened at a substrate temperature of ~185°C (~265°C below the transition temperature) to grow an epitaxial thin Sb layer at this fixed temperature with a constant flux. A well-defined streaky 1×1 RHEED pattern observed after growth of the Sb layer indicated a smooth surface [Fig. 5.11 (c)]. Unlike on GaAs (111)A substrates, in order to obtain a smooth 2D crystal growth of Sb on a GaSb(111)A substrate the surface reconstruction of the GaSb surface needed to remain 2×6 prior to the Sb QW growth. The Sb growth attempted on a 5×1 reconstructed surface on a GaSb(111)A substrates (at T_{sub}=185°C) gave rise to 1D Sb wires [27] instead of a 2D epitaxial layer, as indicated by the spotty RHEED pattern.

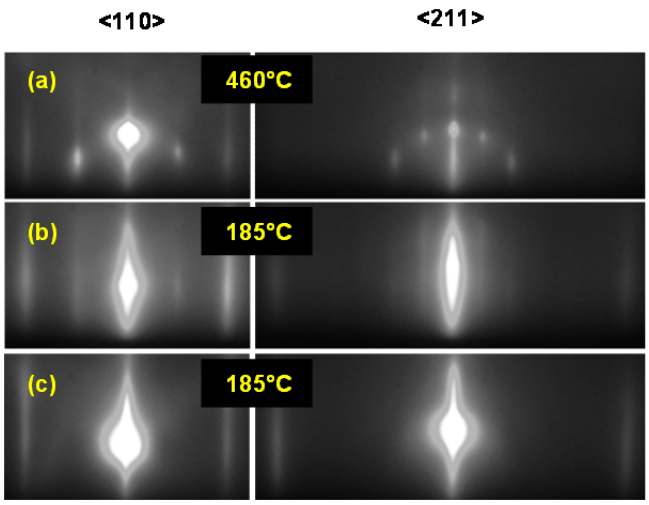

Figure 5.11: RHEED patterns along the <110> and <211> directions for a GaSb(111)A surface (a) at ~460°C, after the growth of a homo-epitaxial GaSb buffer layer under an Sb flux, a GaSb (111)A surface at ~ 185°C without a Sb flux, (b) just before the Sb QW growth and (c) after the Sb QW growth.

5.4.1 Structural properties

Figure 5.12 shows a FE-SEM image of an uncapped ~1.5nm thick (15sec of Sb growth) ultra-thin film of Sb grown at 185°C on an *n*-type GaSb(111)A substrate. The bright areas correspond to the Sb layer while the dark line contrasts are due to the strain, possible induced by the Sb oxide layer on the surface. Unlike in Figure 5.8 (c), threading dislocations indicated by dark point-like features are not seen in these images. The wide spatial distribution and the continuity of the strain lines and absence of voids on the surface indicate that the ultra-thin Sb layer is uniform and completely covers the surface. Threading dislocations, voids or defects on the Sb film are almost completely

removed by the growth on a lattice match GaSb(111)A substrate and further lowering the growth temperature to 185°C.

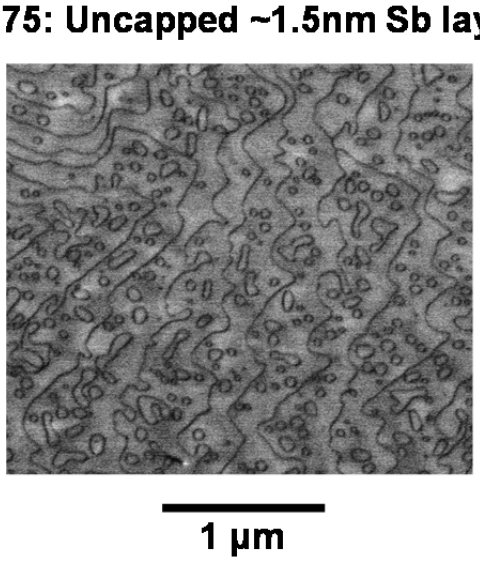

Figure 5.12: Plan view FE-SEM image of the surface of an ultra-thin Sb structure grown at 185°C without a GaSb cap layer on an *n*-type GaSb (111)A substrate. The surface morphology of the Sb layer shows uniform complete coverage.

5.4.2 Electrical properties

Figure 5.13 shows the temperature dependence of the 2D electrical resistivity of a series of uncapped Sb QWs thickness ranging from 1.5nm to 3.2 nm, grown at 185°C on GaSb(111)A substrates. All four structures had lower resistivities at temperatures above 200K than below 200K, in contrast to the films grown on GaAs(111)A, probably due to the lower defect density in the Sb films grown on GaSb substrates. As shown in Figure 5.13 the resistivity increases with decreasing film thickness for all four structures

indicating that the dominant contribution for the resistivity is from the Sb layer. At low temperature the resistivity is approximately inversely proportional to thickness for the films of thickness 2, 2.9 and 3.2 nm indicating that these films behave as semimetals. The relative temperature independence of the resistivity at low temperature for these three Sb films is also consistent with semimetallic behavior.

The resistivity of the 1.5nm thick Sb film is larger than expected from extrapolating the thickness dependence of the 2, 2.9 and 3.2 nm thick Sb layers; however the resistivity is still relatively temperature independent at low temperatures. This behavior may indicate that the 1.5nm film grown on a GaSb(111)A substrate is also conducting, but through topological states as predicted by the calculations [12]. It is possible that the 1.5nm thick Sb film grown on a GaAs(111)A substrate goes insulating faster than the films grown on GaSb(111)A (assuming that the actual thickness is the same for both films). When grown on GaAs, the effective band gap would be increased by both confinement and the residual strain presence in the GaSb and Sb layers. These results do not contradict any of the claims made for Sb layers grown on GaAs substrate since the Sb film deposited for 10sec (~1nm) and 7sec (~0.7nm) show insulating properties (the resistivity data are not shown since the four wire resistance read negative values below 100K due to the high resistivity of these films).

Figure 5.14 shows the 2D resistivity along with the four wire resistance along <211> ($R_{12,43}$) and <110> ($R_{23,14}$) directions for these uncapped Sb films. The anisotropy in the four wire resistance may be due to the defects in preferential directions and/or the irregular shape of the sample. However the four wire resistance along a

<110> direction slightly decreases with decreasing temperatures while that of along <211> is temperature independent for the 1.5nm thick film. This behavior may be associated with some structural phase change in the film but is currently under investigation. Figure 5.15 shows the carrier density at 20K for the Sb ultra-thin films grown on two different substrates as a function of the film thickness. The Sb thin films grown on GaSb(111)A had lower carrier density compared to the films grown on GaAs(111)A substrate. The high hole density which could be due to strong defect doping, and the lower mobility may be the obscure observation of TI states via transport measurement in these films. Further optimization of growth parameters and even thinner films will lead to lower bulk carrier density and increase the mobility in our Sb films.

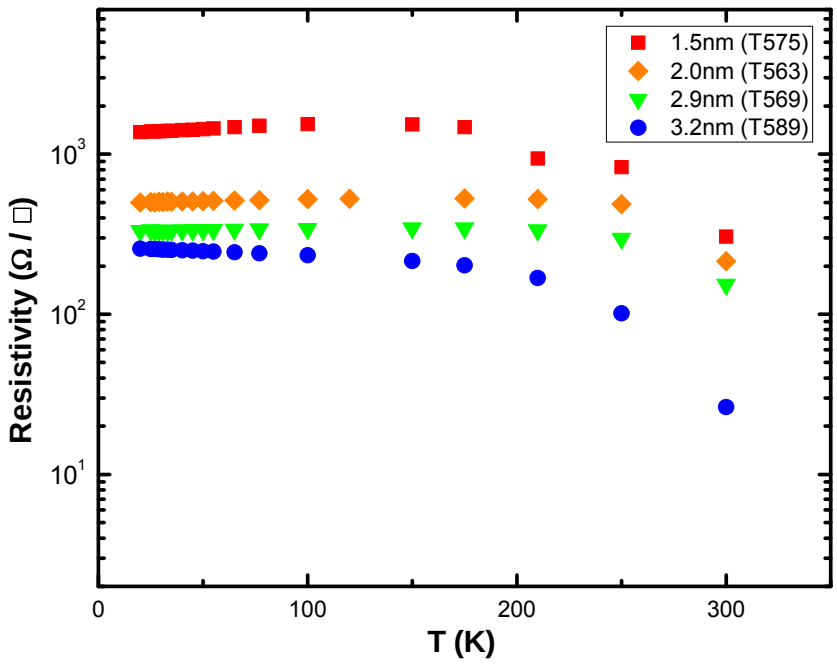

Figure 5.13: Two-dimensional electrical resistivity versus temperature for uncapped ultra-thin Sb layers with different thicknesses grown at 185°C on GaSb (111)A substrate.

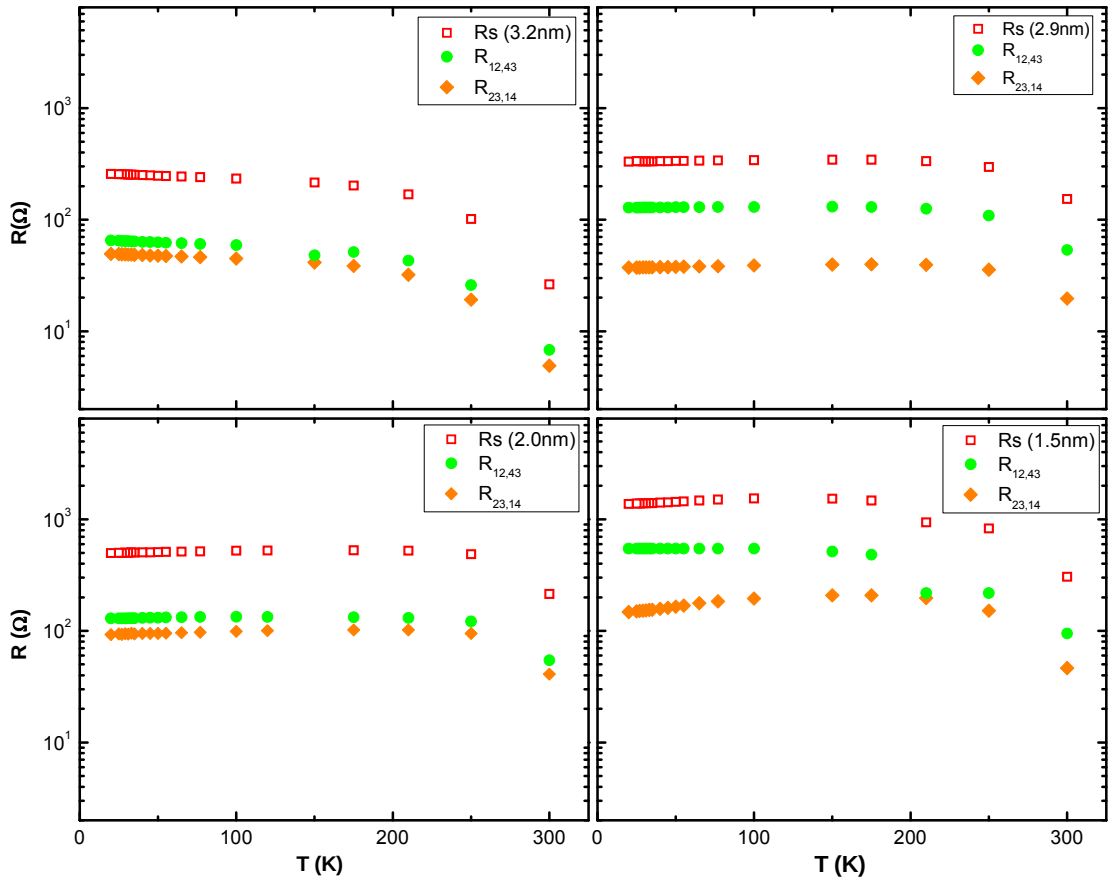

Figure 5.14: Four wire resistance along <211> ($R_{12,43}$) and <110> ($R_{23,14}$) directions and 2D resistivity versus temperature for Sb QWs with different thicknesses grown on GaSb (111)A substrate at 185°C.

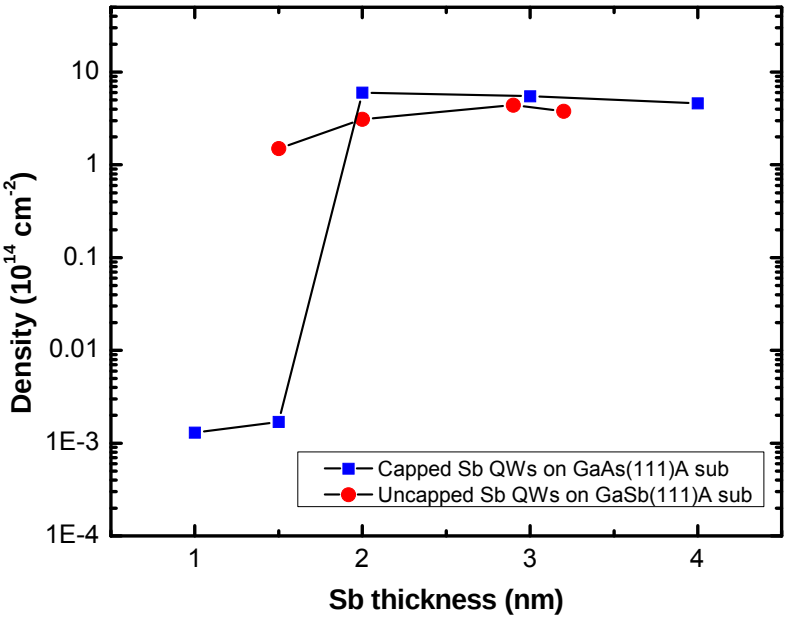

Figure 5.15: A comparison of the carrier density at 20K with the layer thickness for the Sb films grown on GaAs(111)A and GaSb(111)A substrates. The Sb layers grown on GaSb(111)A substrate had no cap in contrast to the layers grown on GaAs(111)A substrates.

5.5 Preliminary study of epitaxial growth of Sb on AlSb (111)A surfaces

AlSb was substituted for GaSb, as the barrier layers for the carriers in Sb. The effect of strain induced by the 0.65% lattice mismatch in Sb/AlSb system, along with the confinement is expected to open up the bulk gap in Sb and thus reveal a 3D TI. The tensile strain induced by the 0.3% lattice mismatch between HgTe and CdTe had been the key parameter in opening up the gap in 70nm thick HgTe layer and hence reveal a 3D TI [24].

5.5.1 Epitaxial growth

A 0.14μm thick AlSb buffer layer was grown on GaAs (111)A substrate at a substrate temperature of ~100°C below the oxide desorption temperature (580°C), at a rate of 0.45 monolayers (ML) per second, and under an Sb_2 rich condition with an Sb_2:Ga beam flux ratio of ~4.1. The surface reconstruction gave rise to a 2×1 RHEED pattern that was maintained during the growth of the AlSb buffer layer. Similar RHEED patterns have been observed for AlSb growth on GaSb (111)A substrates and reported in Reference 28. After closing the Al shutter the substrate temperature was lowered to 300°C under an Sb flux with the RHEED pattern changing from 2×1 to 2×6. The surface established a 1×1 pattern after 13min of deposition at this fixed substrate temperature, forming an epitaxial Sb layer. Further deposition of Sb resulted in poly-crystalline growth as indicated by rings in the RHEED pattern. However, the 1×1 RHEED pattern was recovered a few seconds after closing the Sb shutter. A GaSb cap layer was grown by the two-step MEE procedure at 300°C.

Sb growth was also attempted by pre-cooling the substrate without an Sb flux on a AlSb (111)A surface at a fixed substrate temperature of 270°C. The RHEED pattern remained 2×1 after closing the Sb shutter at 480°C and during the further temperature reduction to 270°C. Poly-crystalline growth resulted after 18s of Sb deposition at this temperature as indicated by the rings in the RHEED pattern. This may be because of the roughness on AlSb surface due to the out diffusion of Sb at higher substrate temperatures during the pre-cooling or due to the lattice mismatch between the AlSb and GaAs (111)A substrates.

5.5.2 Results

Unlike GaSb, an AlSb epilayer grown on GaAs (111)A substrate showed a resistivity of ~1MΩ at 100K. Our initial growth experience showed that the initial nucleation of Sb on the AlSb (111)A surface is critical (maybe due to strain) compared to the nucleation of Sb on the GaSb (111)A surface and establishing the epitaxial growth of Sb on AlSb (111) surface therefore is challenging. It was noticed that the sticking coefficient or the growth rate of Sb (at similar substrate temperature and for a similar Sb flux) on AlSb (111)A is much lower than that of on GaSb (111). An Sb layer deposited for 15min at 300°C (Structure T429) displayed very high resistivity, ~0.1MΩ/□ at 250K, which is more than 100 times higher than the resistivity of ~1.5nm insulating Sb film on GaSb (111)A surface grown on a GaAs(111)A substrate at 250K.

Further optimizations are required to establish the growth conditions to reliably grow epitaxial Sb on a AlSb (111)A surface.

5.6 HR-XRD Results

X-ray diffraction scans were performed along the <111> direction of the reciprocal lattice in the cubic coordinate system, which is parallel to <001> in the hexagonal coordinate system. XRD analysis of Sb films grown by the original method has previously been reported [6]. Figure 5.16 shows the HR-XRD measurement of three films of Sb deposited using the revised growth procedure at 300°C on GaAs (111)A substrate in this study.

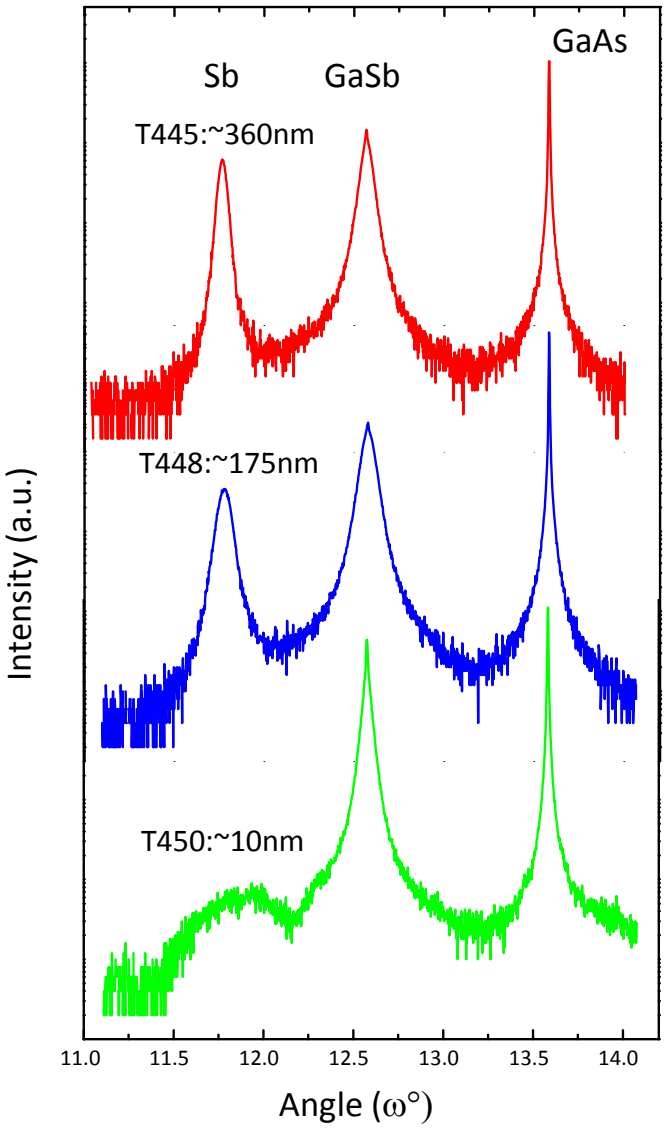

Figure 5.16: High-resolution X-ray ω-2θ scans from the (111) reciprocal plane of Sb films grown using the revised growth procedure on GaAs(111)A substrate.

Diffraction peaks from the Sb (003) plane and GaSb and GaAs (111) planes were observed, confirming the smooth epitaxial growth of Sb. Sb film thicknesses calculated from the X-ray data were comparable with the thickness determined from SEM measurements. A shift in the angular position of the Sb peak towards the GaAs

peak was also observed for a thin film. This indicates that the Sb film become strained as the film thickness is reduced. Calculated strain along a <111> direction and the film thickness from the X-ray data are given in the Table 5.1. Out of plane strain ($\varepsilon_{\perp}$) is calculated with respect to the bulk C_0 (11.273Å) for Sb. The thickness of each film was calculated using the formula given in Equation 2.20 in Chapter 2.

Sample	Sb film thickness (nm)	θ_{bragg}	C (Å) (C_0=11.273)	$\varepsilon_{\perp}$ $(C-C_0)/C_0$	Sb film thickness (nm) (by XRD)
T445	~360	11.8335	11.2710	0.00017	~364.8
T448	~175	11.8443	11.2609	0.00107	~118.0
T450	~10	12.0039	11.1133	0.01417	~16.8

Table 5.1: Structural parameters of epitaxial Sb films grown on GaAs(111) substrates, determined by HR-XRD measurements.

5.8 Summary

In summary, a molecular beam epitaxy technique was developed to reliably grow ultra-thin layers of Sb with good control over the thickness down to a few nanometers. TEM and FE-SEM images indicate good crystalline quality. Resistivity experiments reveal a metal to insulator transition that may be due to quantum confinement. A lower defect density and more uniform Sb ultra-thin films were obtained by the growth on GaSb(111)A substrates. Ongoing transport experiments at low temperature and high magnetic field on these ultra-thin Sb layers are being carried out by Dr. Murphy's group at OU to investigate possible TI states.

Chapter 6

Conclusions and Suggestions for Future Work

The research performed during this dissertation work mainly focused on optimization of growth and structural parameters to improve the electron and hole mobility in narrow gap InSb and InGaAs QWs and realization of elemental Sb QWs with GaSb barriers in order to explore their potential as topological insulators.

Both high electron mobility and hole mobility are required for electronic device applications. High electron mobility of 44,700 cm^2/Vs (251,000 cm^2/Vs) and 11,700 cm^2/Vs (53,800 cm^2/Vs) at room temperature (low temperature) have been achieved in our strained balanced *n*-type InSb and $In_yGa_{1-y}As$ QWs, respectively by optimizing the growth, structural and doping parameters. Further optimizations of well thickness and the doping parameters will lead to even higher mobility in strained balanced $In_yGa_{1-y}As$ QWs. Lower density yet high mobility are required in order to develop gated InSb QWs for experiments in the quantum Hall regime. A low temperature mobility of 139,200 cm^2/Vs with the electron density as low as 1.6×10^{11} cm^{-2} has been achieved for gated InSb device applications.

Hole mobility is equally as important as the electron mobility for CMOS applications. The *p*-type $In_yGa_{1-y}As$ QWs were realized by δ-doping the $In_xAl_{1-x}Sb$ barrier layers with Be. This approach improves the hole mobility by reducing the ionized dopants scattering and allows further optimization of the structural parameters.

The room temperature hole mobilities in our *p*-type $In_{0.75}Ga_{0.25}As$ QWs are lower than the reported hole mobility of similar structures probably due to the strain relaxation. Further optimization of the well width along with the Al composition of the barrier layers will improve the hole mobility in these QWs. From the research conducted on *p*-type InSb QWs, we observed that the hole mobility can be further improved by optimizing the buffer layer structure and further increasing the strain.

A room temperature hole mobility of 1,050cm^2/Vs was achieved in our *p*-type InSb QW with only 1.32% strain, along with an improved buffer layer structure which consists of an $Al_{0.15}In_{0.85}Sb$ initial layer and an $Al_{0.25}In_{0.75}Sb$ metamorphic thick buffer layer. This hole mobility is lower than the reported hole mobility for an InSb QW with 1.9% strain (1230cm^2/Vs) and the hole mobility for an $In_xGa_{1-x}Sb$ QW. Calculations have predicted that the compressive strain in the InSb QW can be increased up to a high of 2% and hence further improve the room temperature hole mobility up to 1600cm^2/Vs [4.18]. The high room-temperature hole mobility observed in our InSb QW with only 1.32% strain is encouraging and also suggest that even higher mobility can be obtained by further optimizing the structural parameters. Our studies of the effect of the buffer layer on hole mobility in InSb showed that the Al percentage difference in the thick relaxed buffer layer and the initial layer and the thickness of the initial layer have significant effects on the hole mobility. The percentage difference between the Al compositions of the thick relaxed buffer layer and the initial layer has to be lower than 10% in order to improve the room-temperature hole mobility. Further studies on thickness dependence of the hole mobility at 300K with the $Al_{0.15}In_{0.85}Sb$ initial layer will be needed for further optimizations of the buffer layer structures.

We were able to develop a molecular beam epitaxy procedure to reliably grow ultra-thin Sb QWs with good crystalline quality and good control over the thickness on the order of few nanometers. The structural and electrical properties of these ultra-thin films were studied. Resistivity experiments reveal a metal to insulator transition that may be due to quantum confinement and suggest that an energy gap exists in our thinner Sb QWs. However calculations including the resistivity of the barrier layers will be needed to explicitly calculate the resistivity of the Sb QWs due to the confinement and to determine the existing energy gap. These ultra-thin Sb QWs provide a good test bed for topological insulators. Weak anti-localization studies at low temperature and high magnetic field are ongoing to investigate possible topological states in our ultra-thin Sb layers grown on GaSb (111)A substrates. Our future research will focus on processing devices with dimensions smaller than the phase breaking length of the carriers to investigate 2D TI states at zero magnetic field.

On the other hand Sb/GaSb superlattice structures with different Sb thicknesses can be used to experimentally determine the band gap versus thickness via magneto-optical experiments. For this purpose further optimization is needed to establish the growth conditions of the Sb/GaSb superlattice structures.

References for Chapter 1:

1. http://department.fzu.cz/surfaces/mbe/soubory/mbe/mbe_method.htm#Kom.
2. J. R. Arthur, "Molecular beam epitaxy", *Surface Science* **500** (2002).
3. G. P. Srivastava, "Theory of semiconductor surface reconstruction", *Rep. Prog. Phys*. **60** (1997).
4. W.K. Liu and M. B. Santos, "surface reconstruction of InSb (001) during molecular beam epitaxy", Surface Science **319**, 172 (1994).
5. http://britneyspears.ac/physics/fabrication/fabrication.htm.

References for Chapter 2:

1. *Characterization of Semiconductor Heterostructures and Nanostructures,* Carlo Lamberti, Elsevier B.V., 2008.
2. XRD data analysis of InSb/AlInSb heterostructures by Prof. Bob Hauenstein from OSU, Oklahoma.
3. PC-MRD User's Guide, first edition, 1993, published by Philips for use with version 1.0 of the PC-MRD software.
4. *X'pert Epitaxy Software, user's guide*, 3rd Edition.
5. V. Drits, J. Srodon and D. D. Eberl, "XRD measurement of mean crystal thickness of Illite and Illite/Smectite: reappraisal of the Kubler index and the Scheerrer equation," Clays and Clay Minerals **45**, 3 (1997).
6. *Solid State Physics*, N. W. Ashcroft and D. N. Mermin, College Edition (1976).

7. L. J. Van der Pauw, "A method of measuring specific resistivity and Hall Effect of discs of arbitrary shape," *Philips Res. Repts*. **13**, 1 (1958).
8. *Introduction to Solid State Physics,* C. Kittel, John Wiley & Sons, Inc., 7th Edition.

References for Chapter 3:

1. R. Chau, "III-V on Silicon for future high speed and ultra-low power digital applications: challenges and opportunities," *CS MANTECH conference*, (2008).
2. E. Sijercic, K. Mueller, and B. Pejcinovic, "Simulation of InSb devices using drift-diffusion equations", *Solid-State Electronics* **49**, 1414 (2005).
3. T. Ashley, A. R. Barns, L. Buckle, S. Datta, A. B. Dean, M. T. Emeny, M. Fearn, D. G. Hayes, K. P. Hilton, R. Jefferies, T. Martin, K. J. Nash, T. J. Philips, W. H. A. Tang, P. J. Wilding and R. Chau, "Novel InSb-based Quantum Well Transistors for Ultra-High Speed, Low Power Logic Applications", *7th International Conference on Solid State and Integrated Circuits Technology*, (2004).
4. N. Goel, J. Graham, J. C. Keay, K. Suzuki, S. Miyashita, M. B. Santos, and Y. Hirayama, "Ballistic transport in InSb mesoscopic structures," *Physica E* **26,** 455 (2005).
5. A. M. Gilbertson, M. Fearn, A. Kormanyos, D. E. Read, M. T. Emeny, T. Ashley, S. A. Solin, and L. F. Cohen, "Ballistic transport and boundary

scattering in InSb/$In_{1-x}Al_xSb$ mesoscopic devices," *Physical Review B* **83,** 075304 (2011).

6. S. Datta, T. Ashley, J. Brask, L. Buckle, M. Doczy, M. Emeny, D.Hayes, K. Hilton, R. Jefferies, T. Martin, T. J. Philips, D. Wallis, P. Wilding and R. Chau, "85nm Gate Lengthh Enhancement and Depletion mode InSb Quantum Well Transitors for Ultra High Speed and Very Low Power Digital Logic Applications", *Technical Digest, IEDM*, (2005).
7. A. R. Dedigama, D. Deen, S. Q. Murphy, N. Goel, J. C. Keay, M. B. Santos, K. Suzuki, S. Miyashita, and Y. Hirayama, " Current Focusing in InSb heterostructures," *Physica E* **34**, 647 (2006).
8. M. B. Santos, K. J. Goldammer, W. K. Liu and R. E. Doezema, "Electrical properties of Si-doped InSb/$Al_xIn_{1-x}Sb$ quantum wells grown by molecular beam epitaxy," *Proceedings of the 8th International Conference on Narrow Gap Semiconductors* (1997).
9. N. Dai, G. A. Khodaparast, F. Brown, R. E. Doezema, S. J. Chung, and M. B. Santos, "Band offset determination in the strained-layer InSb/$Al_xIn_{1-x}Sb$ system," *Appl. Phys. Lett*. **76**, 3905 (2000).
10. T. D. Mishima, M. Edirisooriya, and M. B. Santos, "Low-Defect-Density Crystalline Structure and Method for Making Same," Patent No. US 7,923,098 B2, Date of Patent: April 12, 2011.
11. M. M. Uddin, H. W. Liu, K. F. Yang, K. Nagase, T. D. Mishima, M. B. Santos and Y. Hirayama, "Characterization of InSb quantum wells with atomic layer deposited gate dielectrics," *Appl. Phys. Lett.* **101**, 233503 (2012).

12. T. D. Mishima, and M. B. Santos, "Effect of buffer layer on InSb quantum wells grown on GaAs(001) substrates," *J. Vac. Sci. Technol*. *B* **22**, 1472 (2004).

13. T. D. Mishima, M. Edirisooriya, and M. B. Santos, "Dislocation filtering by $Al_xIn_{1-x}Sb/Al_yIn_{1-y}Sb$ interfaces for InSb-based devices grown on GaAs(001) substrates," *Appl. Phys. Lett*. **88**, 191908 (2006).

14. T.D. Mishima, M. Edirisooriya, and M. B. Santos, "Reduction of micro-twin defects for high-electron-mobility InSb quantum wells", *Appl. Phys. Lett*. **91**, 062106 (2007).

15. T. D. Mishima, M. Edirisooriya, and M. B. Santos, "Dislocation filtering at the interfaces between $Al_xIn_{1-x}Sb$ and $Al_yIn_{1-y}Sb$ layers," *Physica B* **376-377**, 591 (2006).

16. W. K. Liu, K. J. Goldammer, and M. B. Santos, "Effect of substrate temperature on Si compensation in δ-doped InSb and $Al_xIn_{1-x}Sb$ grown by molecular beam epitaxy," *J. Appl. Phys.* **84**, 1367(1998).

17. T. Matsuoka, E. Kobayashi, K. Taniguchi, C. Hamaguchi and S. Sasa, "Temperature dependence of electrical mobility in InGaAs/InAlAs heterostructures," *Jpn. J. of Appl. Phys.*, **29**, 2017 (1990).

18. J. M. S. Orr, A. M. Gilbertson, M. Fearn, O. W. Croad, C. J. Storey, L. Buckle, M. T. Emeny, P. D. Buckle, and T. Ashley, " Electronic transport in modulation-doped InSb quantum well heterostructures," *Physical Review B* **77**, 165334 (2008).

19. O. J. Pooley, A. M. Gilbertson, P. D. Buckle, R. S. Hall, M. T. Emeny, M. Fearn, M. P. Halsall, L. F. Cohen and T. Ashley, "Quantum well mobility and

the effect of gate dielectrics in remotely doped InSb/$Al_xIn_{1-x}Sb$ heterostructures," *Semicond. Sci. Technol*., **25**, 125005 (2010).

20. P. A. R. D. Jayathilaka, S. Cairns, J. Keay, S. Q. Murphy, C. K. Gaspe, T. D. Mishima, and M. B. Santos, "Probing spin-relaxation anisotropy in 1D InSb wires by weak anti-localization," *AIP Conference Proceedings* **1416**, 95 (2011).
21. K. Higuchi, H. Matsumoto, T. Mishima and T. Nakamura, "Optimum design and fabrication of InAlAs/InGaAs HEMT's on GaAs with both high breakdown voltage and high maximum frequency of oscillation," *IEEE Transactions on Electron Devices,* vol, **46**, No 7, 1312 (1999).
22. W. Ha, K. Shinohara, and B. Brar, "Enhancement-mode metamorphic HEMTon GaAs substrate with 2S/mm g_m and 490GHz f_T," *IEEE Electronic Device Lett.,* Vol. **29**, No.5 (2008).
23. S. Solodky, M. Leibovitch, N. Ashkenasy, I. Hallakoun, Y. Rosenwaks and Y. Shapira, " Characterization methodology for pseudomorphic high electron mobility transistors using surface photovoltage spectroscopy," *J. Appl. Phys*., **88**, 6775 (2000).
24. E. Hwang, S. Mookerjea, M. K. Hudait and S. Datta, "Invistigation of scalability of $In_{0.7}Ga_{0.3}As$ quantum well field effect transistor (QWFET) architecture for logic applications," *Solid State Electronics*, in press (2011).
25. D-H. Kim, and J. A. del Alamo, "Lateral and vertical scaling of In0.7Ga0.3As HEMTs for post-Si-CMOS logic applications," *IEEE Transactions on Electron Devices* **55**, 2546 (2008).

26. N. Waldron, D-H. Kim, and J. A. del Alamo, “A self-Aligned InGaAs HEMT architecture for logic applications,” *IEEE Transactions on Electron Devices* **57**, 297 (2010).

27. P. Nam, R. Tsai, M. Lange, W. Deal, J. Lee, C. Namba, P. Liu, R. Grundbacher, J. Wang, M. Barsky, A. Gutierrez-Aitken, and S. Olson, “ Shallow mesa isolation of AlSb/InAs HEMT with AlGaSb buffer Layer using inductively coupled plasma etching,” *GaAs Mantech,* (2005).

28. Y. Xuan, Y. Q. Wu, T. Shen, T. Yang, and P. D. Ye, “High performance submicron inversion-type enhancement-mode InGaAs MOSFETs with ALD Al203, HfO2 and HfAlO as gate dielectrics,” *IEDM Tech. Dig*., **637-640**, Dec. (2007).

29. L. Czornomaz, M. El Kazzi, D. Caimi, P. Mächler, C. Rossel, M. Bjoerk, C. Marchiori and J. Fompeyrine, “Self-aligned S/D regions for InGaAs MOSFETs,” ESSDERC, 219 (2011).

30. S. Oktyabrsky and P. D. Ye, *Fundamentals of III-V semiconducotor MOSFETs*, Springer edition.

31. M. Passlack, N. Medendorp, R. Gregory, and D. Braddock, “Role of Ga_2O_3 template thickness and gadolinium mole fraction in $Gd_xGa_{0.4-x}O_{0.6}/Ga_2O_3$ gate dielectric stacks on GaAs,” *Appl. Phys. Lett*.**83**, 5262 (2003).

32. P. D. Ye, G. D. Wilk, B. Yang, J. Kwo, H.-J. L. Gossmann, M. Hong, K. K. Ng, and J. Bude, “Depletion-mode InGaAs metal-oxide-semiconductor field-effect transistor with oxide gate dielectric grown by atomic-layer deposition,” *Appl. Phys. Lett*. **84**, 434 (2004).

33. I. Ok, H.-S. Kim, M. Zhang, C.-Y. Kang, S. J. Rhee, C. Choi, S. A. Krishnan, T. Lee, F. Zhu, G. Thareja, and J. C. Lee, "Metal Gate–HfO_2 MOS Structures on GaAs Substrate With and Without Si Interlayer, *IEEE Electron Device Lett*. **27**, 45 (2006).

34. H. -S. Kim, I. Ok, M. Zhang, F. Zhu, S. Park, J. Yum, H. Zhao, and J. C. Lee, "Gate oxide scaling down in HfO_2–GaAs metal-oxide-semiconductor capacitor using germanium interfacial passivation layer," *Appl. Phys. Lett*. **91**, 042904 (2007).

35. N. Goel, W. Tsai, C. M. Garner, Y. Sun, P. Pianetta, M. Warusawithana, D.G. Schlom, H. Wen, C. Gaspe, J.C. Keay, M.B. Santos, L.V. Goncharova, E. Garfunkel, T. Gustafsson, "Band offsets between amorphous $LaAlO_3$ film on $In_{0.53}Ga_{0.47}As$,", *Appl. Phys. Lett*. **91**, 113515 (2007).

36. S. P. Kowalczyk, D. L. Miller, J. R. Waldrop, P. G. Newman, and R. W. Grant, "Protection of molecular beam epitaxy grown AlxGa1−xAs epilayers during ambient transfer," *J. Vac. Sci. Technol*. **19**, 255 (1981).

37. InJo Ok, H. Kim, M. Zhang, F. Zhu, S. Park, J. Yum, H. Zhao, Domingo Garcia, Prashant Majhi, N. Goel and W. Tsai, C.K. Gaspe, M.B. Santos, and Jack C. Lee, "Metal gate: HfO2 metal-oxide-semiconductor structures on high-indium-content InGaAs substrate using physical vapor deposition," *Appl. Phys. Letters* **92**, 112904 (2008).

38. InJo Ok, H. Kim, M. Zhang, F. Zhu, S. Park, J. Yum, H. Zhao, Domingo Garcia, Prashant Majhi, N. Goel and W. Tsai, C. Gaspe, M.B. Santos, and Jack C. Lee, "Self-aligned n-channel metal-oxide-semiconductor field effect transistor on

high-indium-content $In_{0.53}Ga_{0.47}As$ and InP using physical vapor deposition HfO_2 and silicon interface passivation layer," *Appl. Phys. Lett*. **92**, 202903 (2008).

39. Feng Zhu, Han Zhao, I. Ok, H. S. Kim, J. Yum, Jack C. Lee, Niti Goel, W. Tsai, C.K. Gaspe, and M.B. Santos, "Effects of Anneal and Silicon Interface Passivation Layer Thickness on Device Characteristics of $In_{0.53}Ga_{0.47}As$ Metal-Oxide-Semiconductor Field-Effect Transistors," *Electrochemical and Solid-State Letters* **12**, H131 (2009).
40. Feng Zhu, Han Zhao, I. Ok, H. S. Kim, J. Yum, Jack C. Lee, Niti Goel, W. Tsai, C.K. Gaspe, and M.B. Santos, "A high performance $In_{0.53}Ga_{0.47}As$ metal-oxide-semiconductor field effect transistor with silicon interface passivation layer," *Appl. Phys. Lett*. **94**, 013511 (2009).
41. Hyoung-Sub Kim, I. Ok, M. Zhang, F. Zhu, S. Park, J. Yum, H. Zhao, Jack C. Lee, Prashant Majhi, N. Goel, W. Tsai, C.K. Gaspe, and M. B. Santos, "A study of metal-oxide-semiconductor capacitors on GaAs, $In_{0.53}Ga_{0.47}As$, InAs, and InSb substrates using a germanium interfacial passivation layer," *Appl. Phys. Lett.* **93**, 062111 (2008).
42. Feng Zhu, Han Zhao, I. Ok, H. S. Kim, J. Yum, Jack C. Lee, Niti Goel, W. Tsai, C. K. Gaspe, and M. B. Santos, "High mobility HfO_2-based $In_{0.53}Ga_{0.47}As$ n-channel metal-oxide-semiconductor field effect transistors using a germanium interfacial passivation layer," *Appl. Phys. Lett*. **93**, 132902 (2008).

References for Chapter 4:

1. B. R. Bennett, M. G. Ancona, and J. B. Boos, "Compound semiconductors for low-power *p*-channel field effect transistors," *MRS Bulletin*, vol. **34,** (2009).
2. C. K. Gaspe, M. Edirisooriya, T. D. Mishima, P. A. R. Dilhani Jayathilaka, R. E. Doezma, S. Q. Murphy, and M. B. Santos, "Effect of strain and confinement on the effective mass of holes in InSb quantum wells," *J. Vac. Sci. Technol. **B*** 29, 03C110 (2011).
3. *The Physics of Low-Dimensional Semiconductors, An Introduction*, John H. Davies, Cambridge University Press, Cambridge, (1998).
4. M. Edirisooriya, T.D. Mishima, C.K. Gaspe, K. Bottoms, R.J. Hauenstein and M.B. Santos, "InSb quantum-well structures for electronic device applications," *J. Cryst. Growth* **311**, 1972 (2009).
5. T. Kasturiarachchi, F.Brown, N. Dai, G. A. Khodaparast, R. E. Doezema, S. J. Chung, and M. B. Santos, "Determination of deformation potentials in strained InSb quantum wells," *Appl. Phys. Lett*. **88**, 171901 (2006).
6. J. Luttinger and W. Kohn, "Motion of Electrons and Holes in Perturbed Periodic Fields," *Phys. Rev.* **97**, 869 (1955).
7. Landölt-Bornstein, *Numerical Data and Functional Relationships in Science and Technology*, edited by O. Madelung, Group III, 22 (Springer, Berlin, 1987).
8. Shawn-Yu Lin, H.P. Wei, D.C. Tsui, and J.F. Klem, "Cyclotron mass of two-dimensional holes in strained-layer GaAs/$In_{0.20}Ga_{0.80}As$/GaAs quantum well structures," *Appl. Phys. Lett.* **67**, 2170 (1995).
9. M. Radosaljevic, T. Ashley, A. Andreev, S.D. Coomber, G. Dewey, M. T. Emeny, M. Fearn, D. G. Hayes, K.P. Hilton, M.K. Hudait, R. Jefferies, T.

Martin, R. Pillarisetty, W. Rachmady, T. Rakshit, S. J. Smith, M. J. Uren, D. J. Wallis, P. J. Wilding, and Robert Chau, "High-Performance 40nm Gate Length InSb *p*-Channel Compressively Strained Quantum Well Field Effect Transistors for Low-Power (VCC=0.5V) Logic Applications," *Proceedings of the IEEE International Electron Devices Meeting*, (2008).

10. T. D. Mishima, and M. B. Santos, "Impact of structural defects upon electron mobility in InSb quantum wells," *J. Appl. Phys*. **109**, 073707 (2011).
11. Z. Soban, J. Voves, and K. Kalna, *J. Physics: Conference Series* **193**, 012128 (2009).
12. W. Pan, K. Lai, S.P. Bayrakci, N.P. Ong, D.C. Tsui, L.N. Pfeiffer, and K.W. West, "Cyclotron resonance at microwave frequencies in two-dimensional hole system in AlGaAs/GaAs quantum wells," *Appl. Phys. Lett*. **83**, 3519 (2003).
13. B. R. Bennett, M.G. Ancona, J.B. Boos, and B.V. Shanabrook, "Mobility enhancement in strained p-InGaSb quantum wells," *Appl. Phys. Lett*. **91**, 042104 (2007).
14. R. T. Hsu, W. C. Hsu, M. J. Kao, and J. S. Wang, "Characteristics of a δ□-doped GaAs/InGaAs p-channel heterostructure field-effect transistor," *Appl. Phys. Lett*. **66**, 2864 (1995).
15. Y-J. Chan and D. Pavlidis, "Single and dual p-doped Channel channel $In_{0.52}Al_{0.48}As/In_xGa_{1-x}As$ (x = 0.53, 0.65) FET's and the role of doping," *IEEE Trans. Elec. Dev*. **39**, 466 (1992).
16. A. M. Kusters, A. Kohl, K. Heime, Th. Schäpers, D. Uhlisch, B. Lengeler and H. Lüth, "Low- and high-field transport properties of pseudomorphic

$In_xGa_{1-x}As/InP$ ($0.73 \leq x \leq 0.82$) *p*-type modulation-doped single-quantum well structures," *J. Appl. Phys.* **75**, 3507 (1994).

17. M. Myronov, K. Sawano, and Y. Shiraki, "Observation of two-dimensional hole gas with mobility and carrier density exceeding those of two-dimensional electron gas at room temperature in the SiGe heterostructures," *Appl. Phys. Lett.* **91**, 082108, 2007.
18. A. Nainani, B. R. Bennett, J. Brad Boos, M. G. Ancona, and K.C. Saraswat, "*Enhancing hole mobility in III-V semiconductors*," *J. Appl. Phys.* **111**, 103706 (2012).
19. Y. Zhang, M. V. Fischetti, B. Sorée, and T. O'Regan, " *Theory of hole mobility in strained Ge and III-V p-channel inversion layers with high-κ insulators*," *J. Appl. Phys.* **108**, 123713 (2010).
20. M. Edirisooriya, T. D. Mishima and M. B. Santos, "Effect of Al composition on filtering of threading dislocations by $Al_xIn_{1-x}Sb/Al_yIn_{1-y}Sb$ heterostructures grown on GaAs(001) ," *J. Vac. Sci. Technol. B* **25**, 3 (2007).

References for Chapter 5:

1. D. E. Savage and M. G. Lagally, "Direct observation by reflection high energy electron diffraction of amorphous to crystalline transition in the growth of Sb on GaAs(110)," *Appl. Phys. Lett*. **50**, 1719 (1987).
2. U. Resch, N. Esser and W. Richter, "Growth mode of Bi and Sb layers on GaAs (110) and InP(110)," *Surf. Sci.* **251/252**, 621 (1991).

3. M. Yamada, A. K. Wahi, P. L. Meissner, A. H-Gomez, T. Kendelewicz, and W. E. Spicer, "Effect of annealing Sb/InP(110) interfaces and Schottky barrier formation of Ag on annealed Sb/InP(110) surfaces," *Appl. Phys. Lett*. **58**, 2243 (1991).

4. S. Morikita and H. Ikoma, "Antimony and bismuth passivations of InP and characterizations of InP metal-insulator-semiconductor structures fabricated by plasma oxidation of Sb- and Bi-passivated InP," *J. Vac. Sci. Technol*. A **21**, 226 (2003).

5. A. J. Noreika, M. H. Francombe, and C. E. C. Wood, "Growth of Sb and InSb by molecular beam epitaxy," *J. Appl. Phys*. **52**, 7416 (1981).

6. J. A. Dura, A. Vigliante, T. D. Golding and S. C. Moss, "Epitaxial growth of Sb/GaSb structures: An example of V/III-V heteroepitaxy," *J. Appl. Phys*. **77**, 21 (1995).

7. T. D. Golding, J. A. Dura, W. C. Wang, J. T. Zborowski, A. Vigliante, H. C. Chen, J. H. Miller Jr and J. R. Meyer, "Investigation of Sb/GaSb multilayer structures for potential application as an indirect narrow-bandgap material," *Semicond. Sci. Technol*. **8**, S117 (1993).

8. W. C. Wang, J. A. Dura, J. T. Zborowski, A. Vigliante, H. C. Chen, T. D. Golding, and J. R. Meyer, , "Preparaion of Sb/GaSb {111}-oriented multilayer structures using molecular-beam epitaxy and migration enhanced epitaxy, " *J. Vac. Sci. Technol. A* **11**, 1001 (1993).

9. V. K. Paliwal1, A. G. Vedeshwar, and S. M. Shivaprasad, "Formation of interfacial phases in the epitaxial growth of Sb on Si(111)-7 × 7 reconstructed surface *Pure Appl. Chem*. **74**, 9 (2002).
10. G. Bian, X. Wang, Y. Liu, T. Miller, and T.-C. Chiang, "Interfacial protection of topological surface states in ultrathin Sb films," *Phys. Rev. Lett*. **108**, 176401 (2012).
11. M. Z. Hasan and C.L. Kane, "Colloquium: Topological Insulators," *Rev. Mod. Phys*. **82**, 3045 (2010).
12. P. Zhang, Z. Liu, W. Duan, F. Liu, and J. Wu, "Topological and electronic transition in a Sb(111) nanofilm: The interplay between quantum confinement and surface effect," *Phys. Rev*. B **85**, 201410 (2012).
13. F. Yang, L. Miao, Z. F. Wang, M.-Y. Yao, F. Zhu, Y. R. Song, M.-X. Wang, J.-P. Xu, A. V. Fedorov, Z. Sun, G. B. Zhang, C. Liu, F. Liu, D. Qian, C. L. Gao, and J.-F. Jia, "Spatial and Energy Distribution of Topological Edge States in Single Bi(111) Bilayer," *Phys. Rev. Lett.* **109**, 016801 (2012).
14. T. Hirahara, N. Fukui, T. Shirasawa, M. Yamada, M. Aitani, H. Miyazaki, M. Matsunami, S. Kimura, T. Takahashi, S. Hasegawa, and K. Kobayashi, "Atomic and Electronic Structure of Ultrathin Bi(111) Films Grown on Bi_2Te_3(111) Substrates: Evidence for a Strain-Induced Topological Phase Transition," *Phys. Rev. Lett.* **109**, 227401 (2012).
15. M. König, S. Wiedmann, C. Brüne, A. Roth, H. Buhmann, L. W. Molenkamp, X.-L. Qi and S.-C. Zhang, "Quantum Spin Hall Insulator State in HgTe Quantum Wells," *Science* **318**, 766 (2007).

16. C. K. Gaspe, S. Cairns, L. Lei, K. S. Wickramasinghe, T. D. Mishima, J. C. Keay, S. Q. Murphy, and M. B. Santos, "Epitaxial Growth of Elemental Sb Quantum Wells," *J. Vac. Sci. Technol. B* **31**, 03C129 (2013).

17. X-Liang Qi and S-Cheng Zhang, "Topological insulators and superconductors," *Rev. Mod. Phys*. **83**, 1057 (2011).

18. L. Fu, C. L. Kane and E. J. Mele, "Topological Insulators in Three Dimensions," *Phys. Rev. Lett*. **98**, 106803 (2007).

19. L. Fu and C. L. Kane, "Topological insulators with inversion symmetry," *Phy. Rev. B* **76**, 045302 (2007).

20. S-Qing Shen, "Quantum hall effect of the surface states in topological insulator," arXiv:0909.4125 [cond-mat.mes-hall] (2009).

21. Y. Xia, D.Qian, D. Hsieh, L.Wray, A. Pal, H. Lin, A. Bansil, D. Grauer, Y.S. Hor, R.J. Cava, and M.Z. Hasan, "Observation of a large-gap topological-insulator class with a single Dirac cone on the surface," *Nat. Phys*. **5**, 398 (2009).

22. D. Hsieh, D. Qian, L. Wray, Y. Xia, Y. S. Hor, R. J. Cava, and M. Z. Hasan, "A topological Dirac insulator in a quantum spin Hall phase," *Nature* **452**, 970 (2008).

23. Y.L. Chen J. G. Analytis, J. H. Chu, Z. K. Liu, S. K. Mo, X. L. Qi, H. J. Zhang, D. H. Lu, X. Dai, Z. Fang, S. C. Zhang, I. R. Fisher, Z. Hussain, and Z. X. Shen, "Experimental realization of a three-dimensional topological insulator, Bi_2Te_3," *Science* **325** 178 (2009).

24. C. Brüne, C. X. Liu, E.G. Novik, E. M. Hankiewicz, H. Buhmann, Y. L. Chen, X. L. Qi, Z. X. Shen, S. C. Zhang and L. W. Molenkamp, "Quantum Hall Effect from the Topological Surface States of Strained Bulk HgTe," *Phys. Rev. Lett*. **106**, 126803 (2011).

25. Y. Horikoshi, M. Kawashima, and H. Yamaguchi, "Migration-Enhanced Epitaxy of GaAs and AlGaAs," *Jpn. J. Appl. Phys*. **27**, 169 (1988).

26. P. Fei, L. Xue-Jin, L. Zhao-Liang, Y. Shu-Li and C. Dong-Min, "Origin of the metallic to insulating transition of an epitaxial Bi(111) film grown on Si(111)," *Chin. Phys. B* **19**, 087201 (2010).

27. A. Proessdorf, F, Grosse, K. Perumal, W. Braun and H. Riechert, "Anisotropic interface induced formation of Sb nanowires on GaSb(111)A substrates," Nanotechnol. **23**, 235301 (2012).

28. A. Proessdorf, F. Grosse, W. Braun, F. Katmis, and H. Riechert, "Analysis of GaSb and AlSb reconstructions on GaSb(111)A-and B-oriented surfaces by azimuthal-scan reflection high-energy electron diffraction," *Physical Review **B*** **83**, 155317 (2011).

Appendix A

Sample	Buffer	Spacer ,Cap thickness (nm)	Si δ-doping surface/ QW ($10^{11}cm^{-2}$) (1170^0C)	InSb QW, Barrier Thickness (nm)	Electron mobility /Density at 300K		Electron mobility/ Density at 20K	
					μ (cm^2/Vs)	n (cm^{-2})	μ (cm^2/Vs)	n (cm^{-2})
T319	Interlayers 10%AlInSb 2.8μm	20%AlInSb 10/10, 10%AlInSb 10/20	30s/30s 3.6/3.6	20, 20	34,440	1.0e12	165,000	4.1e11
T320	Interlayers 10%AlInSb 2.8μm	20%AlInSb 15/5, 10%AlInSb 10/20	30s/30s 3.6/3.6	20, 20	38,890	6.4e11	228,380	2.5e11
T326	Interlayers 10%AlInSb 2.8μm	20%AlInSb 18/2, 10%AlInSb 10/20	30s/30s 3.6/3.6	20, 20	28,980	1.3e12	62,420 (25K)	3.7e11 (25K)
T330	Interlayers 10%AlInSb 2.8μm	20%AlInSb 15/5, 10%AlInSb 10/20 10nm InSb	30s/30s 3.6/3.6	20, 20	32,150	1.4e12	135,380 (50K)	5.3e11 (50K)
T335	Interlayers 10%AlInSb 2.8μm	20%AlInSb 15/5, 10%AlInSb 10/20 10nm InSb	30s/30s 3.6/3.6	20, 20	44,730	5.4e11	251,540 (15K)	3.1e11 (15K)
T338 (Triangular QW)	Interlayers 10%AlInSb 2.8μm	20%AlInSb 15/5, 10%AlInSb 10/20 10nm InSb	30s/30s	20, 20	21,500	5.0e11	51,460	1.9e11
T339	Interlayers 10%AlInSb 2.8μm	20%AlInSb 15/5, 10%AlInSb 10/20 10nm InSb	30s/15s 3.6/1.8	20, 20	39,830	3.6e11	171,500	2.0e11
T341 (3□ whole wafer)	Interlayers 10%AlInSb 2.8μm	20%AlInSb 15/5, 10%AlInSb 10/20 10nm InSb	30s/30s 3.6/3.6	20, 20	43,100	5.0e11	229,500	2.9e11
T350 (doping in the lower barrier)	Interlayers 10%AlInSb 2.8μm	20%AlInSb 15/5, 10%AlInSb 10/20 10nm InSb	25s/30s 3.0/3.6	20, 20	35,620	8.0e11	105,300	5.4e11
T397	Interlayers 10%AlInSb 2.8μm	20%AlInSb 15/5, 10%AlInSb 10/20 10nm InSb	25s/8s 3.0/0.9	20, 20	37,590	3.7e11	139,170	1.6e11

T402	Interlayers 10%AlInSb 2.8μm	20%AlInSb 15/5, 10%AlInSb 10/20 10nm InSb	25s/6s 3.0/0.72	20, 20	35,290	2.6e11	84,550	1.0e11
T409 (3□ whole wafer)	Interlayers 10%AlInSb 2.8μm	20%AlInSb 15/5, 10%AlInSb 10/20 10nm InSb	25s/8s 3.0/0.72	20, 20	35,730	4.5e11	166,280	1.7e11

Table A.1: Summary of asymmetrically doped *n*-type InSb QWs with interlayer buffer grown on GaAs(001) 2°substrates. Interlayers consist of 0.5μm $Al_{0.10}In_{0.90}Sb$, 0.2μm $Al_{0.20}In_{0.80}Sb$, and 0.3μm $Al_{0.10}In_{0.90}Sb$. InSb QW is grown on a 2.8μm thick relaxed $Al_{0.10}In_{0.90}Sb$ buffer layer.

Sample	Buffer Layers	Spacer, Cap thickness (nm)	Si δ-doping near surface/ QW ($10^{11}cm^{-2}$) (1170^0C)	InSb QW, Barrier Thickness (nm)	Mobility/ Density at 300K		Mobility/ Density at 20K	
					μ (cm^2/Vs)	n (cm^{-2})	μ (cm^2/Vs)	n (cm^{-2})
T337	20%AlInSb 1.8 μm 10%AlInSb 0.25 μm	20%AlInSb 15/5, 10%AlInSb 10/20 10nmInSb	30s/15s 3.6/1.8	20, 20	27,260	5.5e11	51,780	3.8e11
T340	20%AlInSb 1.8 μm 10%AlInSb 0.25 μm	20%AlInSb 15/5, 10%AlInSb 10/20 10nm InSb	30s/11s	20, 20	29,000	4.9e11	56,360	3.6e11
T348	20%AlInSb 1.8 μm 10%AlInSb 0.25 μm	20%AlInSb 15/5, 10%AlInSb 20/10 10nmInSb	25s/9s	20, 20	36,730	3.7e11	78,280	3.0e11
T351	20%AlInSb 1.8 μm	20%AlInSb 15/5, 10%AlInSb 10/20 10nmInSb	20s/9s	20, 20	8,970	2.9e11	4,760	1.8e11

Table A.2: Summary of symmetrically doped *n*-type InSb QWs grown on GaAs(001) 2° off substrate.

Appendix B

Sample	Buffer layer Structure	Spacer, and Cap layer Structures (nm)	Be δ-doping near QW, Surface (850^0C)	QW, barrier thickness (nm)	Hole mobility and density at 300K		Hole mobility and density at 20K	
					μ (cm^2/Vs)	n (cm^{-2})	μ (cm^2/Vs)	n (cm^{-2})
T361	0.5μm 10%AlInSb 2.5μm 20%AlInSb	10/10 20%AlInSb 10/20 20%AlInSb 5 nm InSb	12s, 5s	7, 20	-380	-1.9e12	-13,840	-6.8e11
T372	0.5μm 10%AlInSb 2.8μm 20%AlInSb	10/20 20%AlInSb	15s,	7, 20	-500	-1.1e12	-10,970	-3.8e11
T386	0.75μm 7% AlInSb 1.8μm 20%AlInSb	20/30 20%AlInSb 2nm InSb	20s	7, 20	7,380	1.8e11	-70,000	-2.6e11

Table B.1 Summary of 1.05% strained *p*-type InSb QW structures grown on 2° off GaAs(001) substrates.

Sample	Buffer layer Structure	Spacer, and Cap layer Structures	Be δ-doping near QW, Surface (850^0C)	QW, barrier thickness (nm)	Hole mobility and density at 300K		Hole mobility and density at 20K	
					Mobility (cm^2/Vs)	Density (cm^{-2})	Mobility (cm^2/Vs)	Density (cm^{-2})
T369	0.5μm 10%AlInSb 2.5μm 25%AlInSb	10/10nm 25%AlInSb 10/20nm 25%AlInSb	10s, 5s	7, 20	-700	-9.8e11	-12,000	-6.5e11
T370	0.5μm 5% AlInSb 2.5μm 25%AlInSb	10/10nm 25%AlInSb 15/15nm 25%AlInSb	8s, 3s	5, 20	7200	2.3e11	-10,080	-3.8e11
T371*	0.3μm 10%AlInSb 2.5μm 30%AlInSb	15/5nm 30%AlInSb 10/20nm 30%AlInSb 5nmInSb	10s, 8s	7, 20	-650	-1.1e12	-7,150	-7.5e11

T374	0.5µm 10%AlInSb 2.5µm 25%AlInSb	15/5nm 25%AlInSb 10/20nm 25%AlInSb 5nmInSb	10s, 7s	7, 20	-600	-1.1e12	-15,200	-6.4e11
T373	0.5µm 10%AlInSb 2.5µm 25%AlInSb	15/5nm 25%AlInSb 10/20nm 25%AlInSb 5nmInSb	8s, 6s	7, 20	-580	-9.9e11	-16,000	-4.4e11
T375	0.5µm 10%AlInSb 2.57, 20µm 25%AlInSb	10/10nm 25%AlInSb 10/20nm 25%AlInSb 5nmInSb	6s, 5s	7, 20	-350	-1.7e12	-17,670	-5.0e11
T379	3.0µm 25%AlInSb	15/20nm 25%AlInSb 5nmInSb	15s,	6, 20	-500	-8.2e11	-3,880	-3.5e11
T380	2.4µm 25%AlInSb	10/30nm 25%AlInSb 5nmInSb	12s	6 20	-850	-5.8e11	-10,600	-4.3e11
T381	2.4µm 25%AlInSb	10/30nm 25%AlInSb 2nmInSb	15s	6, 20	-750	-7.1e11	-8,750	-5.2e11
T387	0.8µm 9% AlInSb 1.8µm 25%AlInSb	10/10nm 25%AlInSb 10/30nm 25%AlInSb 2nmInSb	10s, 10s	7, 20	2940	3.4e11	-38,860	-5.7e11
T388	0.8µm 7% AlInSb 1.5µm 25%AlInSb	20/30nm 25%AlInSb 2nmInSb	25s	6 20	8080	2.2e11	-49,600	-3.6e11
T393	0.8µm 9% AlInSb 1.7µm 25%AlInSb	20/30nm 25%AlInSb 2nmInSb	25s	7 20	4200	2.5e11	-52,200	-4.4e11
T396	0.88µm 10%AlInSb 1.8µm 25%AlInSb	20/30nm 25%AlInSb 2nmInSb	25s	7, 20	1400	6.0e11	-50,600	-4.8e11
T398	0.88µm 10%AlInSb 1.8µm 25%AlInSb	20/30nm 25%AlInSb 2nmInSb	37s	7, 20	680	1.3e12	-44,550	-5.4e11
T401	0.88µm 10%AlInSb 1.8µm 25%AlInSb	20/30nm 25%AlInSb 2nmInSb	25s	7, 20	1200	6.5e11	-29,300	-5.8e11
T399	0.88µm 10%AlInSb 1.8µm 25%AlInSb	20/20nm 25%AlInSb 2nmInSb	25s	7, 20	-200	-2.6e12	-26,700	-4.3e11
T400	0.5µm 10%AlInSb 1.8µm 25%AlInSb	20/30nm 25%AlInSb 2nmInSb	25s	7, 20	-350	-1.9e12	-32,900	-4.8e11

T401	0.8µm 7% AlInSb 1.5µm 25%AlInSb	20/30nm 25%AlInSb 2nmInSb	25s	7, 20	1200	6.5e11	-29,300	-5.8e11
T403	0.3µm 10%AlInSb 1.8µm 25%AlInSb	20/30nm 25%AlInSb 2nmInSb	25s	7, 20	-770	-8.2e11	-24,700	-4.9e11
T438	0.5µm 10%AlInSb 0.2µm 25%AlInSb 0.3µm 10%AlInSb 1.8µm 25%AlInSb	20/30nm 25%AlInSb 2nmInSb	25s	7, 20	23 (non-linear hall curve)	3.4e13 (non-linear hall curve)	-51,900	-5.0e11
T439	0.5µm 10%AlInSb 0.3µm 30%AlInSb 1.8µm 25%AlInSb	20/30nm 25%AlInSb 2nmInSb	25s	7, 20	-100	-6.2e12	-22,900	-4.5e11
T447	0.8µm 15%AlInSb 1.8µm 25%AlInSb	20/30nm 25%AlInSb 2nmInSb	25s	7, 20	-1,050	-5.8e11	-23,900	-3.9e11
T449	0.5µm 10%AlInSb 0.2µm 25%AlInSb 0.3µm 15%AlInSb 1.8µm 25%AlInSb	20/30nm 25%AlInSb 2nmInSb	25s	7, 20	-10 (non-linear hall curve)	-6.6e13 (non-linear hall curve)	-46,750	-3.8e11
T466	0.5µm 10%AlInSb 0.2µm 25%AlInSb 0.3µm 15%AlInSb 1.8µm 25%AlInSb	20/30nm 25%AlInSb 2nmInSb	25s	7, 20	100	5.8e12	-34,900	-3.8e11

Table B.2 Summary of 1.32% strained *p*-type InSb QW structures grown on 2° off GaAs(001) substrates. *****Structure T371 had a 1.59% strained InSb QW.

Sample	x	y	Spacer thickness (nm)	Be δ-doping near QW, Surface (850^0C)	QW, barrier thickness (nm)	Hole mobility and density at 300K		Hole mobility and density at 25K	
						Mobility (cm^2/Vs)	Density (cm^{-2})	Mobility (cm^2/Vs)	Density (cm^{-2})
P104	64	45	10	1.0E+12, 4.2E+12	10, 20	-80	-3.3E+12	-2,600	-7.6E+11
P107	64	52	10	1.0E+12, 4.2E+12	10, 20	-40	-5.8E+12	-4,500	-7.5E+11
P108	75	45	10	1.0E+12, 4.2E+12	10, 20	-10	-1.6E+13	-200	-7.5E+11
P124	64	45	10	1.0E+12, 4.2E+12	10, 20	-90	-2.2E+12	-3,700	-4.2E+11
P178	64	45	10	1.0E+12, 4.2E+12	10, 20	-130	-1.9E+12	-4,160	-9.0E+11
P179	64	52	10	1.0E+12, 4.2E+12	10, 20	-140	-2.0E+12	-5,300	-9.1E+11
P185	75	45	10	1.0E+12 4.2E+12,	10, 20	-230	-1.2E+12	-4,500	-1.2E+12
P186	64	45	10	1.5E+12 4.2E+12,	10, 20	-110	-2.3E+12	-3,440	-9.1E+12
P187	64	45	5	1.0E+12 4.2E+12,	10, 20	-120	2.0E+12	-2,550	-9.3E+11
P189	75	45	10	1.0E+12 4.2E+12,	15, 20	-220	-1.2E+12	-1,560	-8.7E+11

Table B.3 Summary of *p*-type $In_xGa_{1-x}As/In_yAl_{1-y}As$ QW structures grown on InP(001) substrates.